LIBRA-SP: A Self-Consistent Design of a Commercial Fusion Power Plant Based on Self-Pinched Propagation of Ions

Final Report for Calendar Year 1994

B. Badger, D. Bruggink, P. Cousseau, R.L. Engelstad, Y-M. Lee, H.Y. Khater, G.L. Kulcinski, J.J. MacFarlane, E.A. Mogahed, G.A. Moses, R.R. Peterson, S. Rutledge, M.E. Sawan, I.N. Sviatoslavsky, P. Wang, L.J. Wittenberg, C.L. Olson, R.E. Olson

December 1994

FPA-94-6

FUSION POWER ASSOCIATES

2 Professional Drive, Suite 248
Gaithersburg, Maryland 20879
(301) 258-0545

1500 Engineering Drive
Madison, Wisconsin 53706
(608) 263-2308

LIBRA-SP

A Self-Consistent Design of a Commercial Fusion Power Plant Based on Self-Pinched Propagation of Ions

Final Report for Calendar Year 1994

B. Badger, D. Bruggink, P. Cousseau, R. L. Engelstad, Y-M. Lee,
H. Y. Khater, G. L. Kulcinski, J. J. MacFarlane, E. A. Mogahed,
G. A. Moses, R. R. Peterson, S. Rutledge, M. E. Sawan,
I. N. Sviatoslavsky, P. Wang, L. J. Wittenberg

Fusion Power Associates
402 Gammon Place, Suite 280
Madison, Wisconsin 53719
(608) 833-3388

C. L. Olson and R. E. Olson

Sandia National Laboratory
Albuquerque, NM 87185

December 1994

FPA-94-6

Contents

1. Executive Summary **1-1**

2. Introduction **2-1**

3. Ion Beam Generation and Transport **3-1**

3.1. Two-Stage Ion Diode 3-1

3.2. Self-Pinched Transport 3-3

3.3. Ion Beam Parameters 3-4

4. Target Calculations **4-1**

4.1. Introduction 4-1

4.2. Physics Models 4-5

4.2.1. PHD-IV Target Simulation Code 4-5

4.2.2. EOS and Opacity Models 4-6

4.3. Results 4-11

4.4. Target Neutronics 4-20

4.5. Discussion and Future Work 4-21

5. Design of PERIT Units **5-1**

5.1. Overall Design 5-1

5.2. First Surface Protection 5-7

5.2.1. Motivation and Introduction 5-7

5.2.2. Recent Work and Discussion 5-8

5.2.3. Analysis of Flow in Sheets 5-10

5.3. Mechanical Response 5-15

5.4. Neutronics Analysis 5-19

5.5. Thermal Hydraulic Analysis 5-23

5.5.1. Introduction 5-23

5.5.2. Geometry 5-23

5.5.3. Thermal Hydraulics Calculations 5-26

6. Beam Ports and Diode Damage Assessment **6-1**

6.1. Diode Enclosure Environment 6-1

6.1.1. Double Rotating Discs 6-1

6.1.2. Single Rotating Discs 6-2

6.1.3. Modeling the Problem 6-2

6.1.4. System Conductances 6-3

6.1.5. Required Pumping Speed 6-5

6.2. Neutronics Analysis 6-6

7. Tritium and Safety Analysis **7-1**

7.1. Tritium Issues 7-1

7.1.1. Target Fuel Preparation 7-1

7.1.2. Reactor Building Tritium Inventory 7-1

7.1.3. Tritium Breeding and Recovery from the Liquid $Li_{17}Pb_{83}$ Alloy 7-3

7.2. Environmental and Safety Assessment 7-6

7.2.1. Introduction 7-6

7.2.2. Safety Design Goals 7-7

7.2.3. Off-Site Definitions 7-8

7.2.4. Calculational Procedure 7-9

7.2.5. Activation Analysis 7-10

7.2.6. Maintenance 7-13

7.2.7. Radwaste Classification 7-15

7.2.8. Routine Atmospheric Effluents 7-16

7.2.9. Containment Accident Analysis 7-18

7.2.10. Doses from the Target Factory and Fuel Reprocessing Facilities . . . 7-21

7.2.11. Nuclear Grade Components 7-23

8. LIBRA-SP System Parameters **8-1**

9. Conclusions and Recommendations **9-1**

1. Executive Summary

The third reactor design in the LIBRA (Light Ion Beam ReActor) series is described in this report. The LIBRA-SP (Self-Pinched) concept has many similarities and differences compared to its predecessors, LIBRA and LIBRA-LiTE.

The main similarities include:

- 30 MeV Li ions to drive the light ion fusion DT target.
- The use of Helia pulsed power technology.
- The protection of the first walls with fluids carried in porous tubes which are in turn contained inside the reaction chamber.
- The net electrical power of LIBRA-SP and LIBRA-LiTE is $\approx$ 1000 MWe.

The main differences among the reactor systems include:

- The method of ion beam propagation from the diodes to the target (channel transport in LIBRA, ballistic transport in LIBRA-LiTE, and self-pinch transport in LIBRA-SP).
- The solid material containing the coolant/breeder liquid (woven SiC tubes containing a Pb-Li alloy in LIBRA, woven HT-9 steel tubes containing Li in LIBRA-LiTE, and perforated HT-9 steel tubes containing a Pb-Li alloy in LIBRA-SP).
- The lack of internal magnets in LIBRA-SP to help in the focusing of the ions in the chamber.

The net results of the current design effort are:

1. A much simpler design of the energy conversion chamber.
2. A lower recirculating power fraction (16%-LIBRA-SP vs. 18%-LIBRA-LiTE, and 25%-LIBRA).
3. A lower direct capital cost for the power plant (1640 [$93]/kWe for LIBRA-SP, $1740 for LIBRA-LiTE, and $2570 for LIBRA).

This report also gives the first information on detailed light ion target spectra and debris since the recent declassification in the U.S. Inertial Fusion Program. The techniques and codes developed in this study have continuously improved the understanding of how an attractive light ion power plant might operate and have pointed the way to even greater improvements in safety, reliability, and economics.

2. Introduction

The LIBRA (Light Ion Beam ReActor) concept has been developed over the past decade into the premier commercial power reactor study for light ions. Even though this concept has not been studied continuously over that period, critical issues associated with the idea have been under continuous scrutiny during that time. The evolution of the LIBRA-SP (SP=Self-Pinched) concept was addressed in a paper presented at the Eleventh Topical Meeting on the Technology of Fusion Energy held in New Orleans, LA, June 19-23, 1994. A copy of this paper is included in the Appendix. Additional background for the concept was also given at the Technical Meeting on Drivers for Inertial Fusion Energy sponsored by the IAEA in Paris, November 14-18, 1994 by Dr. G. Kessler and the description of LIBRA-SP will be published by the IAEA.

The specific statement of work (SOW) on LIBRA for the calendar year 1994 is given below.

A. Develop theoretical models for the propagation of protons from the pre-pulse diodes to the target in a self-pinched mode.

B. Develop theoretical models for the propagation of Li ions from the main diodes to the target in a self-pinched mode.

C. Modify the SCATBALL code to compute the beam losses due to scattering in the reactor chamber.

D. Design the entrance ports and shielding for the pre-pulse and main diodes.

E. Integrate the self-pinched propagation mode with the LIBRA-SP reactor cavity designed for the Sandia National Laboratory (SNL) in the US.

In addition to the SOW above, we initiated work on two long-standing problem areas: the modification of the INPORT units used to protect the first wall, and the calculation of target performance. The latter opportunity was not recognized at the start of CY 1994, but due to major declassification in the U.S. Inertial Fusion Program, we were able to add this area to our previous analyses.

Each of the topics in the SOW will be addressed in the subsequent chapters and verification of the calculations performed for this contract will, hopefully, be at least partially verified by experiments at SNL in CY 1995. We will incorporate the results from SNL into our work in CY 1995 to improve the LIBRA concept even further.

3. Ion Beam Generation and Transport

3.1. Two-Stage Ion Diode

As in all earlier versions of LIBRA, a magnetically insulated extraction ion diode is used to accelerate the driver ions. Earlier versions used single stage diodes. Since the conclusion of LIBRA-LiTE, considerable experimental [1,2] and theoretical [3] progress has been made on multi-stage diodes, showing them to couple diode energy to the ions more efficiently and to reduce beam divergence. A multi-stage diode accelerates ions across more than one gap by having more than one virtual cathode; a single stage diode has one cathode and one gap.

A schematic picture of the LIBRA-SP 2-stage diode concept is shown in Fig. 3.1. The picture is only schematic and is not necessarily to scale. Two sets of insulating magnets are shown; the central cone and an outer ring. These define the magnetic fields in the cathode region. There are clearly other magnets in the anode region and elsewhere, which are not shown. The central cone of magnets defines the inner radius of the anode source plasma, R_i. The focal length of the diode, F, is controlled by the shape of the anode, the magnets and the degree of neutralization of the beam ions. The cathode tips are held to potentials V_1 and V_2, relative to the potential of the diode. The gap widths of the two stages are d_1 and d_2.

The outer radius of the anode plasma, R_o, is an important parameter for the self-pinched transport. R_o is determined by the required anode area, A_a and R_i. R_i must be large enough to contain all of the magnetic field coils, power feeds and cooling within the inner cone. The required particle current I_d and the current density J_d determine A_a. J_d is the space-charge limited current density J_{scl} times an enhancement factor K_e, which accounts for the fact that the ions are emitted from a volume of plasma and not from an infinitely thin surface. To avoid a high beam microdivergence θ_μ, K_e should be no more than 5. J_{scl} is a function of d_1 and V_1,

$$J_{scl} = 0.715 \frac{V_1^{3/2} q_1}{A d_1^2} \,. \tag{3.1}$$

$V_1/(V_2 - V_1)$ is thought to affect θ_μ, though in a way that is not yet clear. For the current work, we assume that $V_1 = 0.5 V_2$. It is important that θ_μ be as low as possible because

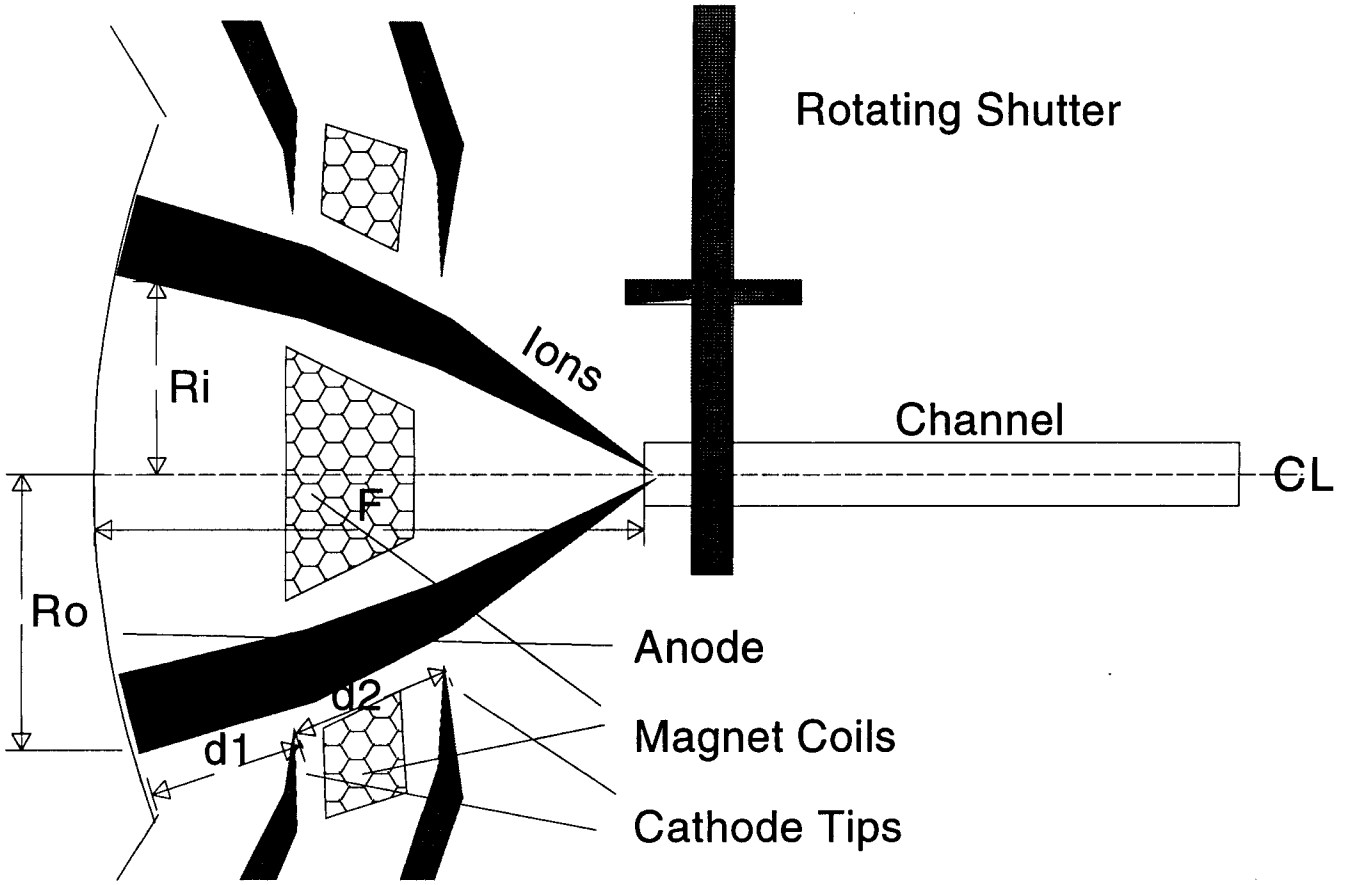

Figure 3.1. Schematic picture of LIBRA-SP two stage diode.

it determines the focal spot size that affects the self-pinched transport. The magnets must supply an applied magnetic field at twice the critical field to avoid the shorting of either gap by the cathode electrons before ions are accelerated, B_{crit},

$$B_{crit} = 0.34\frac{(V^2 + V)^{1/2}}{d} \text{ tesla}\,, \tag{3.2}$$

with V in MV and d in cm. A separate B_{crit} will exist for each gap. These will define the coils.

The focal spot radius r_f is determined by F, θ_μ, and scattering. The effects of scattering and microdivergence add in quadrature,

$$r_f^2 = F(\theta_\mu^2 + \theta_{scat}^2). \tag{3.3}$$

θ_{scat} is the growth in microdivergence caused by scattering. The SCATBALL computer code has been used to calculate r_f with the scattering explicitly calculated and we have found that, for the assumed chamber gas densities, scattering does not have an important impact on the spot size. The focal spot size and R_o/F determine the self-pinched transport parameters.

3.2. Self-Pinched Transport

In the LIBRA-SP concept, the ion beams are transported to the target in the self-pinched mode. The net electrical current of the beams provides the azimuthal magnetic fields that confine the ions to the channels. The required net electrical current is

$$I_{net} = 0.5\left(\frac{R_o}{r_f}\right)^2 \theta_\mu^2 I_A. \tag{3.4}$$

I_A is the Alfvén current,

$$I_A = \beta\gamma\frac{A}{q}\frac{m_p c^3}{e}. \tag{3.5}$$

β and γ are the normal relativistic parameters, A is the beam ion atomic mass, e is the electronic charge, c is the speed of light, and m_p is the mass of a proton. For the beam to have a current of I_{net}, most of the ion current must be neutralized by electrons ionized from the target chamber gas. The electrons move with the beam ions, neutralizing most of the

ion current. The current neutralization fraction is

$$f_m = 1 - \left(\frac{I_{net}}{I_{beam}} \right) . \tag{3.6}$$

The degree of neutralization achieved can only be calculated with a full 2-D electromagnetic particle-in-cell computer simulation.

The guiding of a self-pinched beam to the target is one open question. Lasers could be used to pre-ionize a path to the target. The increased conductivity might lead to propagation along a preferred direction. Another option, the method chosen for LIBRA-SP, uses guide tubes that aim the beams at the target. It is thought that the beams will propagate in a straight line without any pre-ionizing by a laser. The beams must be aimed precisely. The guide tubes confine the beam with image charges and will allow some large radius bends. Neither of these methods has been studied in any detail.

In a self-pinched beam the neutralization is created by the head of the beam. Azimuthal magnetic fields are created in the head of the beams and are frozen in when the conductivity is sufficiently high. The head of the beam is not itself fully confined and is continually eroded, leading to an energy loss per unit transport length. This is not related to any energy loss per ion, but is a loss of ions. From a discussion with Dale Welch of Mission Research Corporation in Albuquerque, NM, a 30 MeV fully stripped 50 kA net current beam would lose 1 ns of beam per 400 cm of transport. We have scaled an energy loss law from this,

$$\epsilon = E_{pulse} \frac{1\,\text{ns}}{\tau} \frac{L_{beam}}{400\,\text{cm}} \frac{I_{net}}{50\,\text{kA}}. \tag{3.7}$$

This is only one component to the efficiency. Each ion may lose energy from axial fields and scattering.

3.3. Ion Beam Parameters

The concepts described in the previous two sections have been used to create consistent designs for the diodes and transport systems. The overall parameters, which serve as the system requirements, are shown in Table 3.1. The target requires 7.2 MJ in a 40 ns pre-pulse and a 20 ns main pulse. The main pulse is time-of-flight bunched by a factor of

Table 3.1. LIBRA-SP General Ion Beam Parameters

Parameter	Unit	Main	Pre-Pulse
Ion species		Lithium	Lithium
Ion energy	MeV	30	30
Energy on target	MJ	6.0	1.2
Total transport efficiency	%	90	90
Energy leaving diodes	MJ	6.67	1.33
Number of beams		12	12
Pulse width at diodes	ns	40	40
Pulse width at target	ns	20	40
Power at diodes	TW	167	33
Power at target	TW	300	30
Particle current at diodes	MA	5.56	1.11
Particle current at target	MA	10	1

2. The ions must be roughly 30 MeV lithium ions. The peak total power must be 330 TW. These parameters have been used in designing the diodes, whose parameters are shown in Table 3.2. Both the main and pre-pulse diodes accelerate the lithium ions to 30 MeV in 2 stages; we assume that the charge state in both stages is 1, and that the stages have equal voltages. The diode parameters determine the self-pinched transport parameters, shown in Table 3.3.

References for Section 3

1. M. G. Mazarakis, et al., "Light Ion Pulsed Power Induction Accelerator for the Laboratory Microfusion Facility," Proceedings of the 15th Biennial Particle Accelerator Conference (1993) IEEE Publ. Serv.

2. S. Miyamoto, et al., "Intense Light Ion Beam Divergence in Single-Stage and 2-Stage Diodes," *IEEE Transactions on Plasma Science*, **21**, 567 (1993).

3. S. A. Slutz and M. P. Desjarlais, "Theory of Multistage Intense Ion-Beam Acceleration," *J. Appl. Phys.*, **67**, 6705 (1990).

Table 3.2. LIBRA-SP Diode Parameters

Parameter	Unit	Main	Pre-Pulse
Current/diode	kA	463	92.6
Voltage Drop 1 V_1	MV	15	15
Voltage Drop 2 V_2	MV	30	30
Physical Gap 1 d_1	cm	2	2
Physical Gap 1 d_2	cm	2	2
Enhancement factor K_e		5	5
Inner anode radius R_i	cm	10	10
Microdivergence θ_μ	mrad	4	4
Focal length F	cm	150	150
J_{scl}	kA/cm^2	0.3	0.3
J_d	kA/cm^2	1.5	1.5
Anode area A_a	cm^2	309	62
Outer anode radius R_o	cm	14.1	10.9
Focal spot radius r_f	cm	0.6	0.6
R/F		0.094	0.073
B_{crit} for Gap 1	T	2.63	2.63
B_{crit} for Gap 2	T	2.63	2.63
B_{appl} for Gap 1	T	5.27	5.27
B_{appl} for Gap 2	T	5.27	5.27

Table 3.3. LIBRA-SP Self-Pinched Transport Parameters

Parameter	Unit	Main	Pre-Pulse
Transport length L	cm	800	800
γ		1.005	1.005
β		0.096	0.096
Charge state		3	3
Alfvén current	kA	6958	6958
I_{net}	kA	30.7	18.5
f_m		0.978	0.933
Energy loss ϵ	kJ	17.1	2.1
Efficiency	%	96.9	98.1

4. Target Calculations

4.1. Introduction

High-gain targets to be used in inertial confinement fusion (ICF) power reactors are expected to release $\sim 10^2 - 10^3$ MJ of energy in the form of x-rays, energetic ions, and neutrons [1-3]. This energy originates in the central, highly compressed core of an ICF target due to fusion of deuterium (D) and tritium (T). The primary fusion products of D-T reactions are α-particles (^{4}He) and 14 MeV neutrons, while secondary products from D-D and D-^{3}He reactions include lower energy neutrons, gamma photons, and charged particles (^{3}He, T, and protons). Because charged particles have relatively short mean free paths, the bulk of this energy is deposited within the target. Energy is transferred from the hot central fuel region to the outer layers of the target by radiation, conduction, and mass motion (kinetic energy) leading to release of x-rays and ion debris. On the other hand, a significant fraction of the neutrons escape the target. It is important to understand the partitioning of energy during the target explosion phase because it provides information critical to the design of ICF target chambers.

Below, we describe calculations of the fusion burn and explosion energetics of the ICF target for the LIBRA-SP light ion fusion reactor design [4]. In this design, the spherical target is irradiated with 24 Li ion beams (12 prepulse and 12 full power) containing a total energy of 7.2 MJ. The peak beam power on target is 330 TW and the pulse width of the full power beams is 20 ns. Internal pulse shaping of the x-ray flux onto the capsule [5] is expected to lead to a gain of about 80, thus producing a total target yield of approximately 550-600 MJ.

The purpose of this investigation is to begin to address quantitatively the *explosion* dynamics of the LIBRA target. It is anticipated that the physics of the *implosion* phase will be addressed in a future study. To study the explosion dynamics, we start with an already-imploded configuration which represents a reasonable representation of the target plasma conditions at the instant of ignition. The evolution of the target breakup is then simulated using the PHD-IV radiation-hydrodynamics code [6]. This code computes the

Table 4.1. LIBRA-SP Target and Ion Beam Parameters

	LIBRA-SP
Total absorbed beam energy	7.2 MJ
Peak beam power (main + prepulse)	330 TW
Hohlraum radius	0.7 cm
Yield	589 MJ
Peak beam intensity	54 TW/cm^2
Target gain	82

time-dependent fusion burn and energy transport within the target. The calculations also utilize new equation of state (EOS) and opacity models developed at Wisconsin [7]. The primary goal of the calculations is to make quantitative predictions for the time-dependent target x-ray flux and ion debris energy. These quantities can then be used to determine the response of the target chamber first wall to the target microexplosion.

The original LIBRA [1] and LIBRA-LiTE [8] designs utilized scaled versions of targets originally designed for heavy ion beam reactors [2] because of classification issues in the U.S. However, recent declassification of light ion targets now allows the use of more realistic target configurations [9]. The LIBRA-SP target design, shown in Fig. 4.1, is based on the target design for the Laboratory Microfusion Facility (LMF) [9]. Several of the LIBRA-SP target parameters are listed in Table 4.1. The two targets are designed with the same strategy. The beam ions penetrate the Hohlraum case and deposit in a low density carbon or plastic foam that is doped with high Z impurity to control the deposition profile. The foam heats to 200-300 eV, creating the drive radiation which is confined by the Hohlraum case. The radiation burns through the pulse-shaping layer around the capsule, shortening the pulse of radiation in the process. The capsule is then driven to implosion by the reshaped radiation pulse. This design has been studied in detail for the LMF target [9]. The predicted gain for the LIBRA-SP design is compared with that of other ICF reactor conceptual design studies in Fig. 4.2.

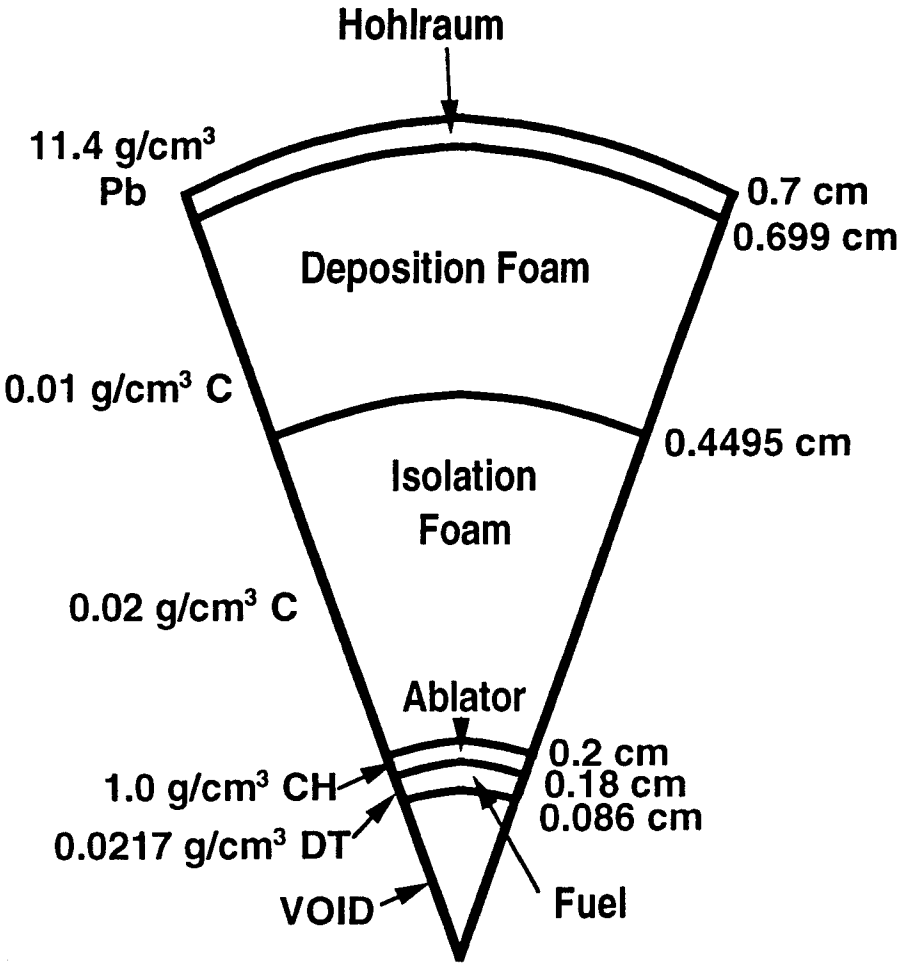

Figure 4.1. Schematic of initial target configuration for LIBRA-SP.

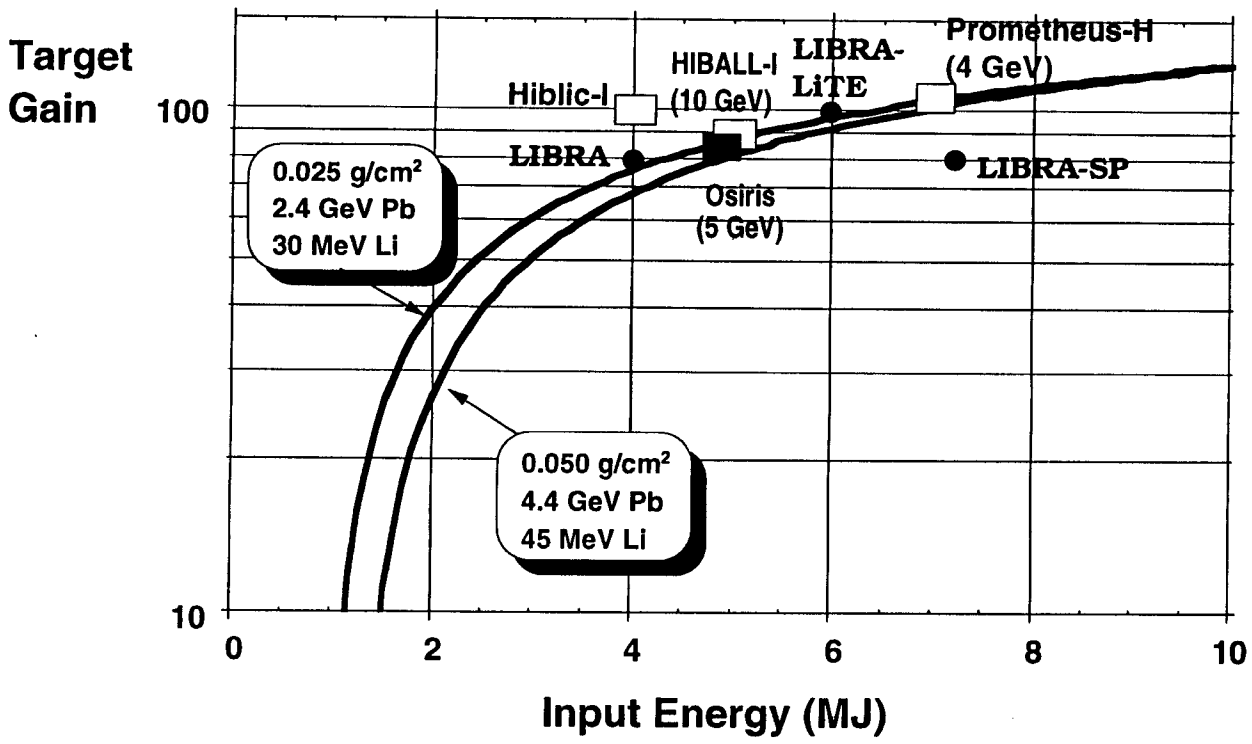

Figure 4.2. Comparison of target gains from several ICF reactor conceptual design studies. The performance of targets that rely on internal pulse shaping is slightly degraded from other ICF target designs.

4.2. Physics Models

4.2.1. PHD-IV Target Simulation Code

PHD-IV [6] is a plasma radiation-hydrodynamics code with models for ion beam energy deposition and fusion burn designed to model ICF target physics processes. It is a 1-D Lagrangian code which solves the single-fluid equation of motion with pressure contributions from electrons, ions, radiation, and fast charged particle reaction products. Energy transfer in the plasma is treated with a 2-temperature model — i.e., separate ion and electron temperatures. Thermal conduction through each species is treated using Spitzer's form of the thermal conductivity. The electron conductivity is flux-limited. Radiation emission and absorption terms couple the electron temperature equation to the radiation transport equations. In addition, the electron and ion temperature equations contain source terms that couple them to the ion beam energy deposition calculation and the energy deposited from the fusion reactions.

The simulations for the LIBRA-SP target utilize a hybrid equation of state model which couples high-density thermodynamic properties calculated using a muffin-tin model to lower density properties which are computed using a detailed configuration accounting model. Multigroup opacities are computed using the EOSOPA code (see below). Radiation is transported using a multigroup flux-limited diffusion model [10]. A total of 200 frequency groups was used in the simulation described below. The time-dependent radiation energy density equations are solved using implicit finite difference techniques.

Fusion reaction equations for DT, DD, and D-^{3}He are solved and the reaction products are transported and slowed using a time-dependent particle tracking algorithm. In addition, PHD-IV includes an ion beam energy deposition package to model the time which includes contributions to the stopping power from both bound and free electrons. However, this latter package was not required for the microexplosion simulation described below.

4.2.2. EOS and Opacity Models

The equation of state covers a wide domain of densities and temperatures. It consists primarily of three contributions: (1) the zero-temperature isotherm, (2) a thermal electronic component, and (3) a thermal ionic part. We have used a hybrid model in the equation of state calculations: a detailed configuration accounting (DCA) model is used for the low-density, high-temperature regime, while a "muffin-tin" model [11] is used for the high-density regime.

In the detailed configuration accounting model, each isolated ion in the plasma is in equilibrium with free electrons. Plasma effects on each atomic system are considered as perturbations. Ion abundances and level occupation numbers are obtained from detailed ionization balance calculations. In our LIBRA-SP calculations, the EOS's are obtained for plasmas with local thermodynamic equilibrium (LTE) populations. Continuum lowering effects are accounted for in the opacity calculations using an occupation probability formalism [12]. The following contributions are included in the equations of state: (1) the translational energy of ions and atoms, (2) the energy of partially degenerate electrons, (3) configuration effects from Coulomb interactions (Debye-Hückel corrections), and (4) atomic internal contributions (excitations and ionizations).

The muffin-tin model is used to accurately compute the equation of state for high-density plasmas. It is applicable to electrons on the zero-temperature isotherm as well as for any finite temperature. It has much of the simplicity of an isolated atom model but captures much of the physics of the band-structure model. In particular, it provides an accurate description of cohesion and the behavior of solids under compression. This model also describes an isolated atom or an ion in equilibrium with an electron gas in low density cases. Hence the muffin-tin model smoothly connects high-density electron degenerate regime and low-density plasma regime. This smooth connection provides thermodynamic consistency of calculated equations of state over a wide domain of temperatures and densities.

Our hybrid model is designed to provide reliable equations of state over a wide range of temperatures and densities. Figure 4.3 shows our results for energy and pressure isotherms of aluminum. In the low-density regime, the nonlinear behavior due to ionization/excitation is clearly seen. The cohesive, degenerate, and pressure ionization effects are observed for the high-density regime. Figure 4.4 shows a comparison of calculated shock Hugoniots with experimental data for Al and Au. It can be seen that the agreement is good.

In order to be able to treat properly the transfer of radiation in LIBRA targets, it is necessary to have values of the opacity for both low-Z and high-Z elements in a wide range of conditions. Radiation is absorbed by atoms and ions via the following types of processes: (1) bound-bound transitions (line absorption); (2) bound-free transitions (photoionization); (3) free-free transitions (Bremsstrahlung); (4) scattering of photons by electrons. In principle, the calculations of opacity for low-Z and high-Z systems are the same. In practice, however, they must be treated differently. We use a detailed term accounting (DTA) method for low-Z systems, and use an unresolved transition array (UTA) model for high-Z systems.

For high-Z atomic systems, especially for the ions in electronic configurations with open d or f shells, each configuration contains a very large number of levels. As a consequence, the number of lines corresponding to the bound-bound transitions between these levels are so numerous that it is impractical to do detailed line accounting calculations. On the other hand, these lines are so closely packed that intrinsic broadening effects suffice to merge them together. Because of this characteristic of high-Z line spectra, an unresolved transition array (UTA) model [13] can be used to compute high-Z opacities. The UTA model uses an average transition between configuration-averaged atomic levels to represent the numerous possible transitions (the transition array) between configurations. The splitting effect of these lines is accounted for by using a line shape for each transition array which is determined from Slater integrals. It is very important to include line broadening due to this UTA effect. Figure 4.5 shows a comparison of gold opacities calculated with and without this broadening effect. The curve on the left was calculated with normal line shapes which include Doppler, natural, and electron impact broadening, while the curve on the right also includes UTA

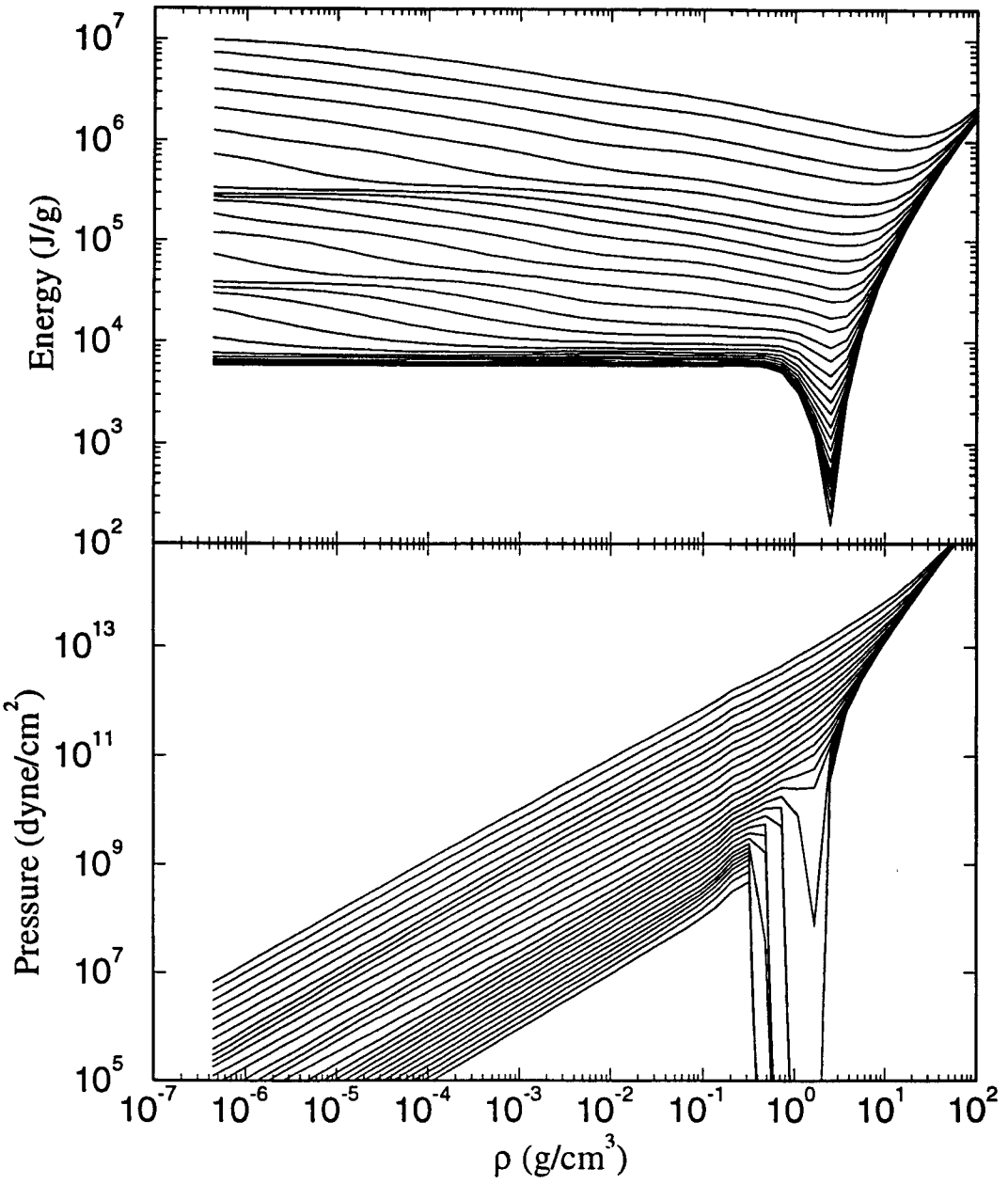

Figure 4.3. Energy and pressure isotherms calculated for Al using hybrid equation of state model.

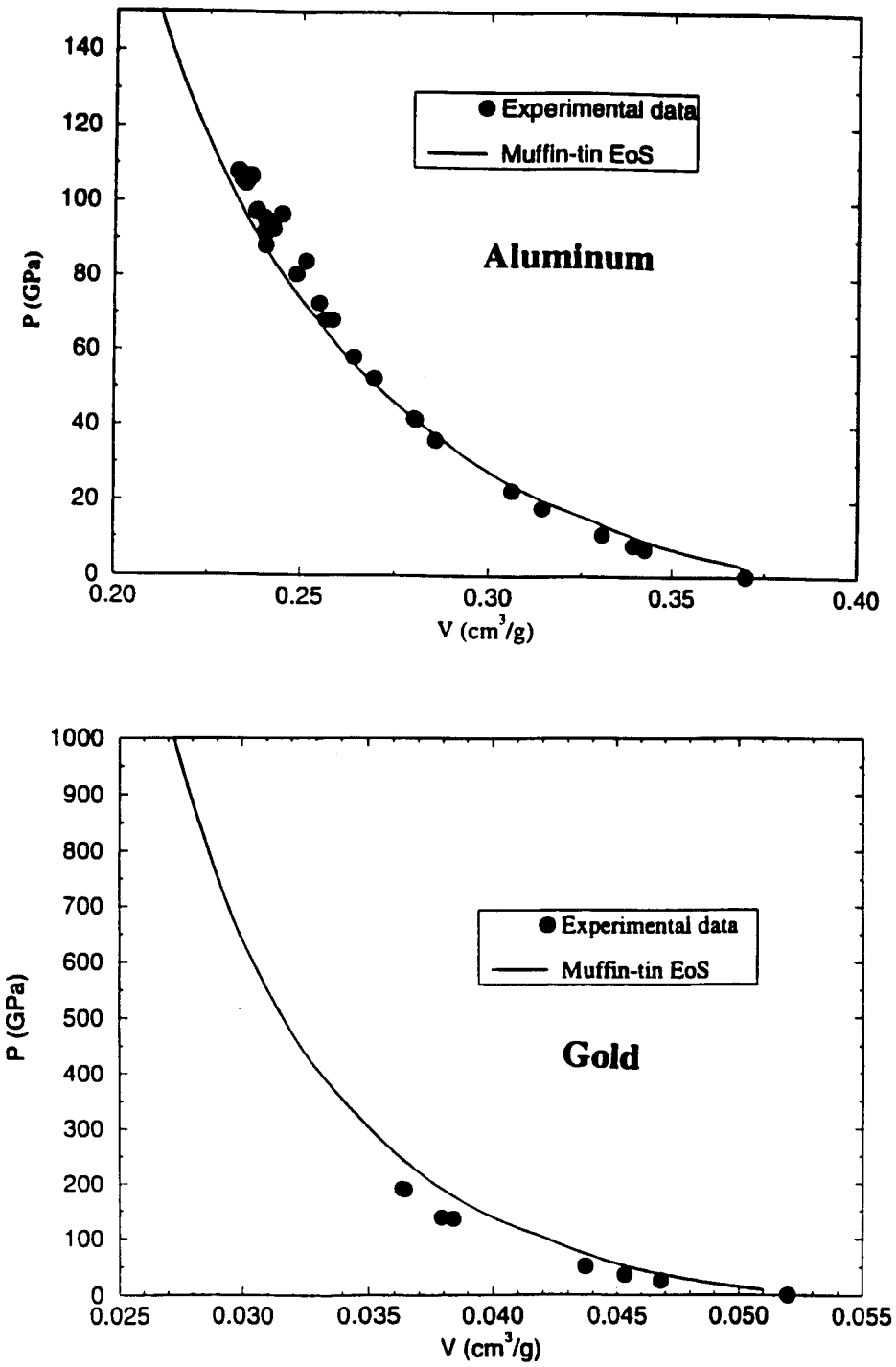

Figure 4.4. Comparison of calculated shock Hugoniots with experimental data for Al and Au.

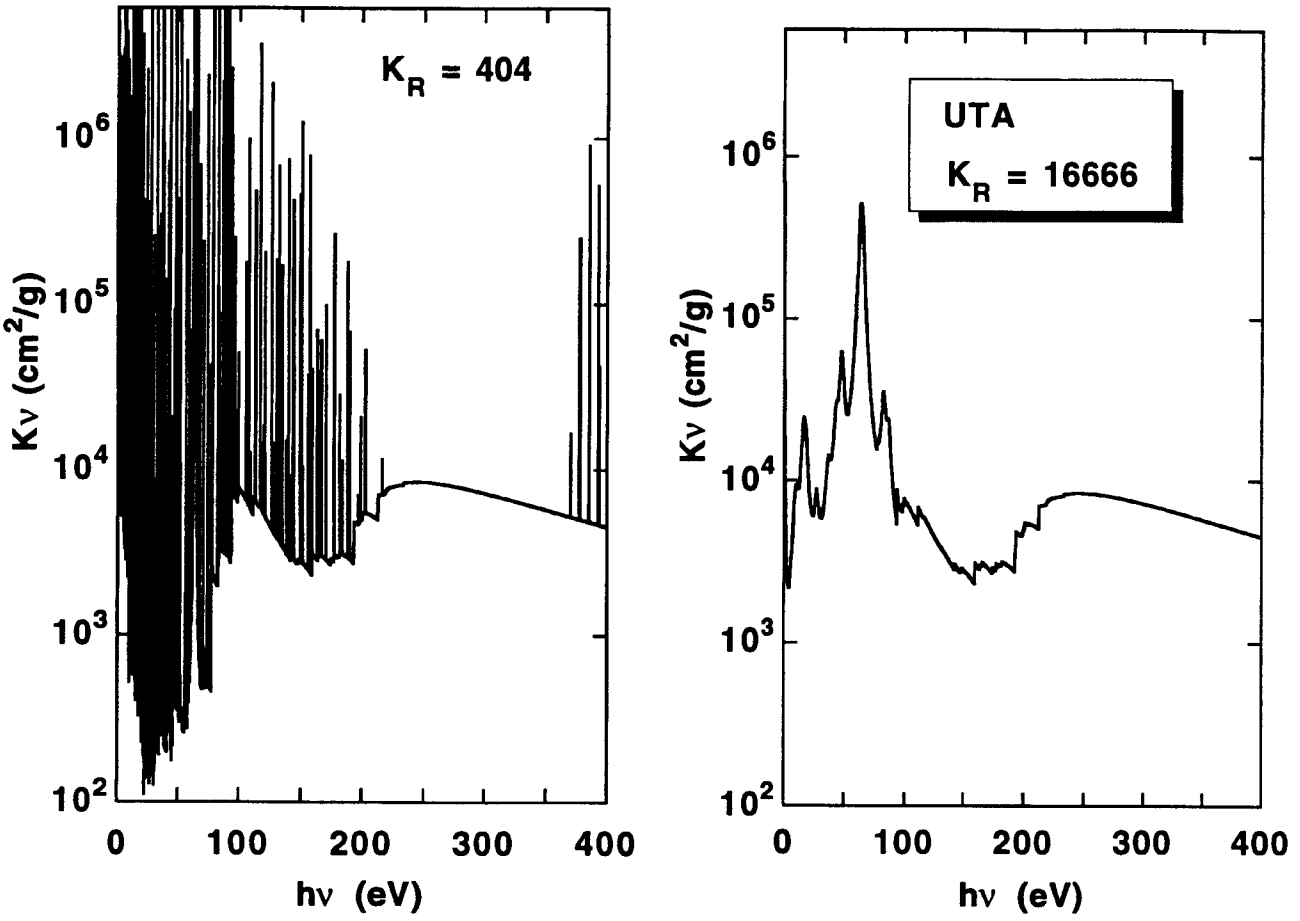

Figure 4.5. Frequency-dependence of Au opacity from calculations neglecting (left) and including (right) broadening due to UTA's.

broadening. It is seen that the non-UTA result leads to a mean Rosseland opacity that is a factor of 40 lower than the UTA result. The UTA model is more accurate and is used in our Pb opacity calculations for the LIBRA target.

To assess the reliability of our opacity calculations, we have compared our results with other theoretical results [14]. In general, we find good agreement with some of the more reputable opacity codes (e.g., OPAL [15] and STA [16]).

4.3. Results

Conditions at the start of ignition assumed for the microexplosion simulation are shown in Fig. 4.6. At present, we simply assume these conditions can be roughly achieved using the beam parameters discussed above in conjunction with an x-ray internal pulse shaping scheme [9]. Clearly, however, a numerical simulation of the implosion is required to provide a more accurate target configuration at ignition.

The LIBRA-SP target is composed of 4 materials: the central DT fuel, a CH ablator, C deposition and isolation foams, and an outer Pb case (Hohlraum). At the start of the PHD-IV simulation, each of the material regions is assumed to have a uniform temperature and density, with the values indicated in Fig. 4.6. The exception to this is the DT fuel, which consists of a central hot spot surrounded by two other DT regions of successively higher density and lower temperature. The outer Pb region is assumed to have expanded by almost three orders of magnitude by the start of ignition. A total of 100 spatial zones was used in the simulation. At the start of the simulation, the areal density of the central hot spot is 0.3 g/cm^2, while that of the entire DT fuel is 3.3 g/cm^2. The fusion burn begins in the hot DT core which is initially at 8 keV. The burn region then propagates outward engulfing the entire DT region. By the end of the simulation a burn fraction of approximately 35% is achieved.

Results from the simulation are shown in Figs. 4.7 through 4.11. Figure 4.7 shows the time-dependent position of the Lagrangian zones, which indicate the material motion in the target. Figures 4.8 and 4.9 describe the energy partitioning and radiation flux histories. Figure 4.10 shows time-integrated spectra for the radiation flux escaping the target at several

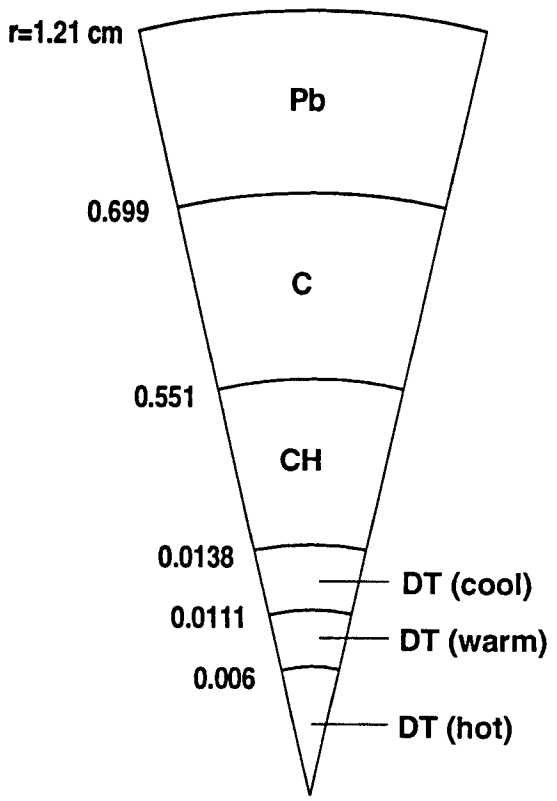

Mass (mg)	Material	T (keV)	ρ (g/cm^3)
120	Pb	0.1	0.020
17.4	C	0.25	0.024
9.1	CH	0.25	0.013
4.2	DT (cool)	0.1	800
0.8	DT (warm)	0.5	166
0.0045	DT (hot)	8	50

Figure 4.6. Conditions at the start of ignition assumed for the PHD-IV LIBRA-SP simulation.

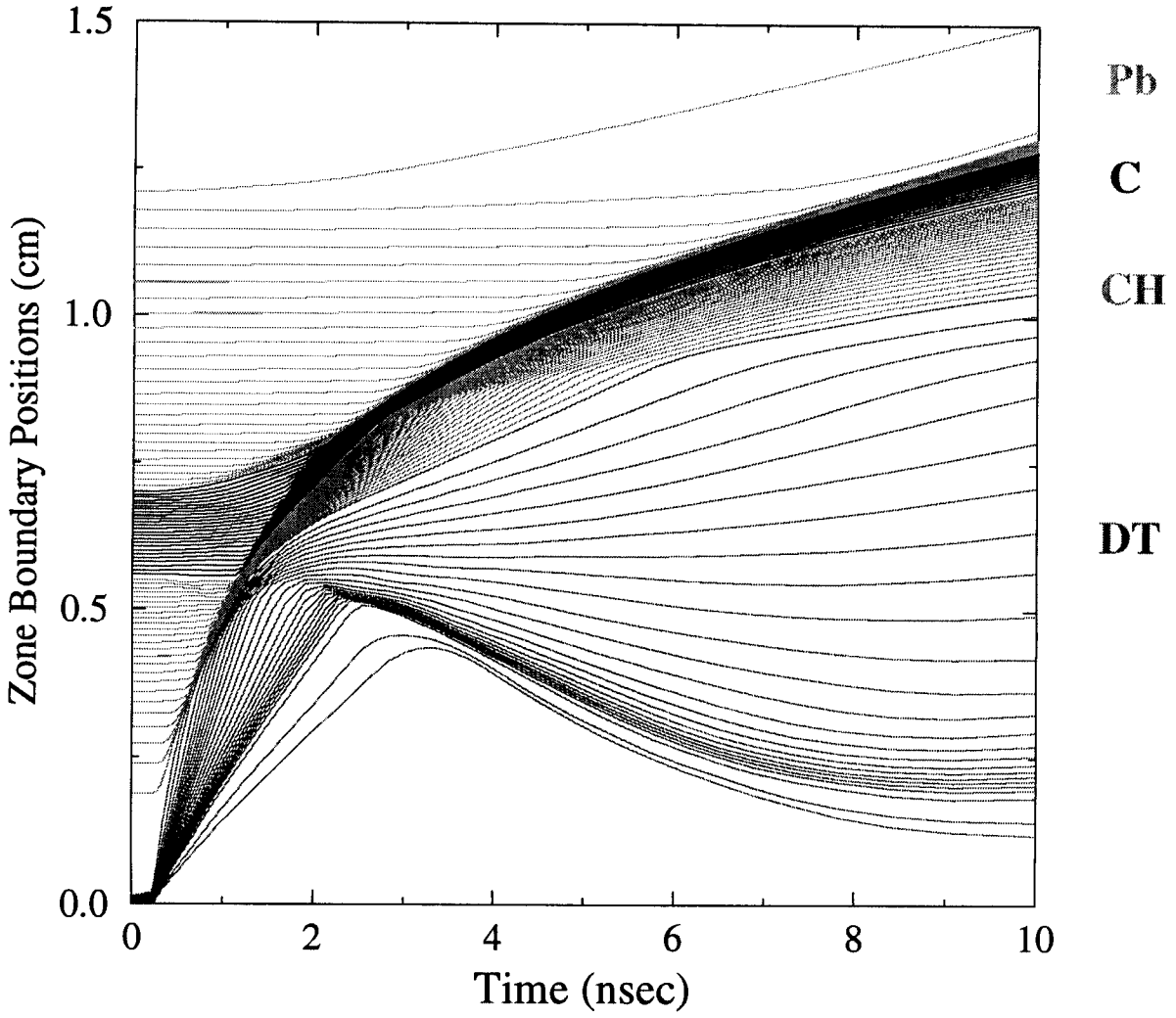

Figure 4.7. Time-dependence of Lagrangian zone boundaries.

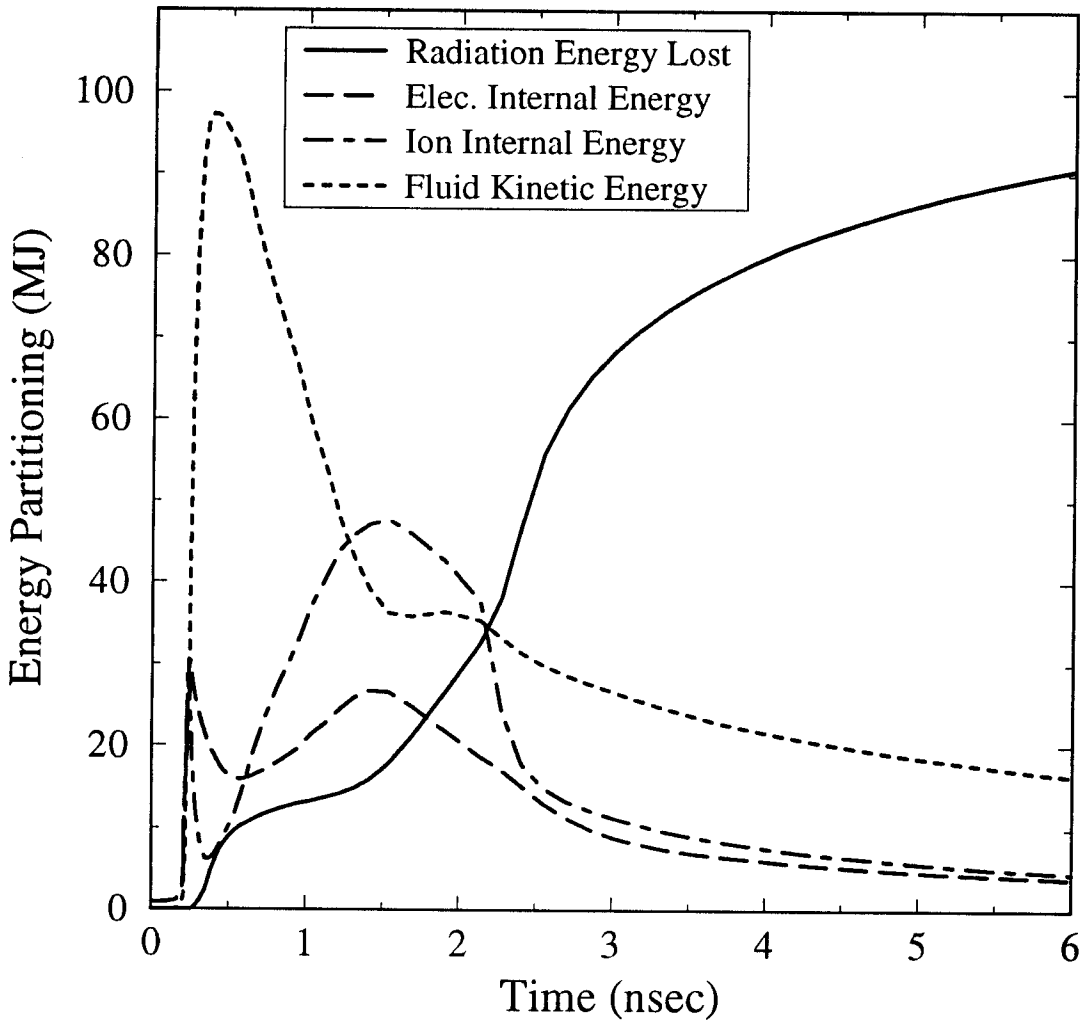

Figure 4.8. Time-dependence of energy partitioning in LIBRA-SP target.

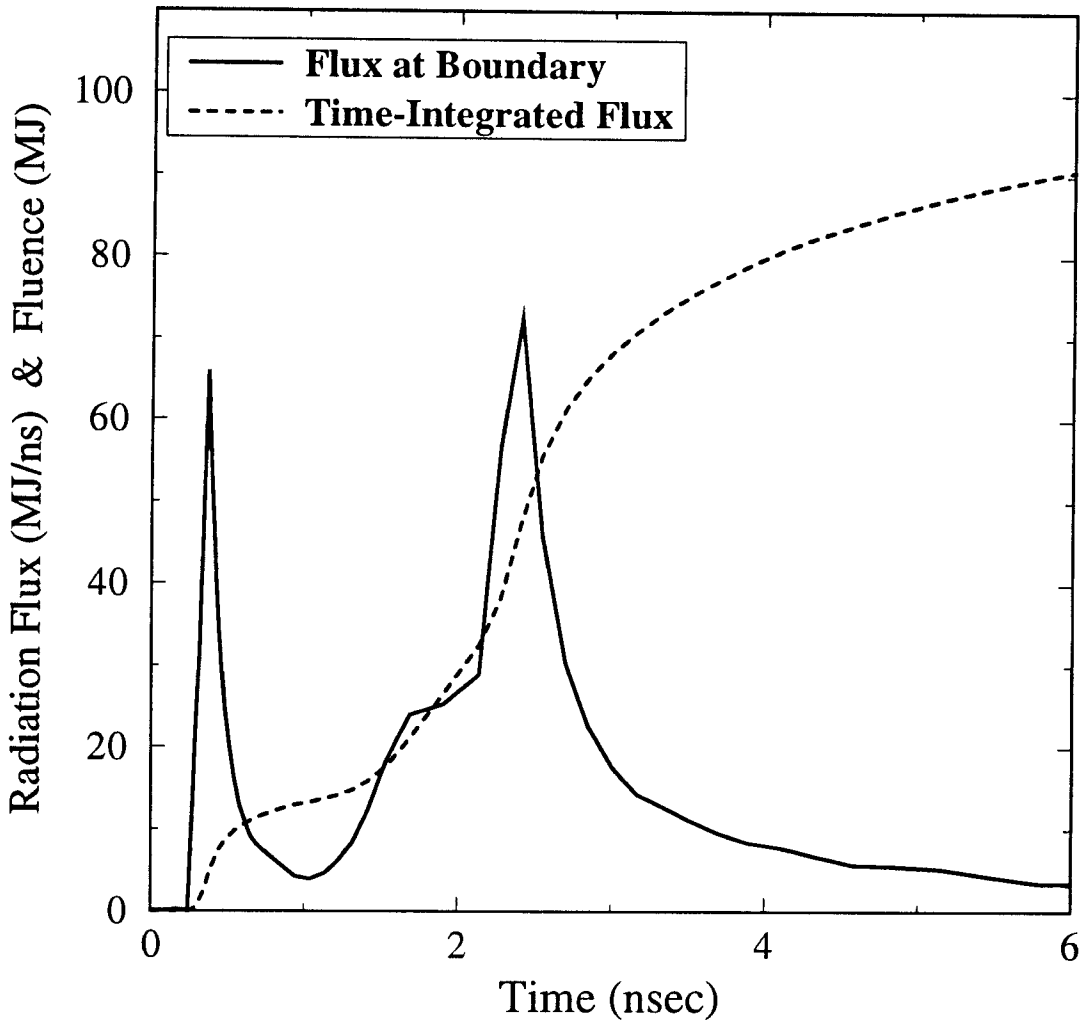

Figure 4.9. Time-dependent and time-integrated radiation power emitted from the boundary of the LIBRA-SP target.

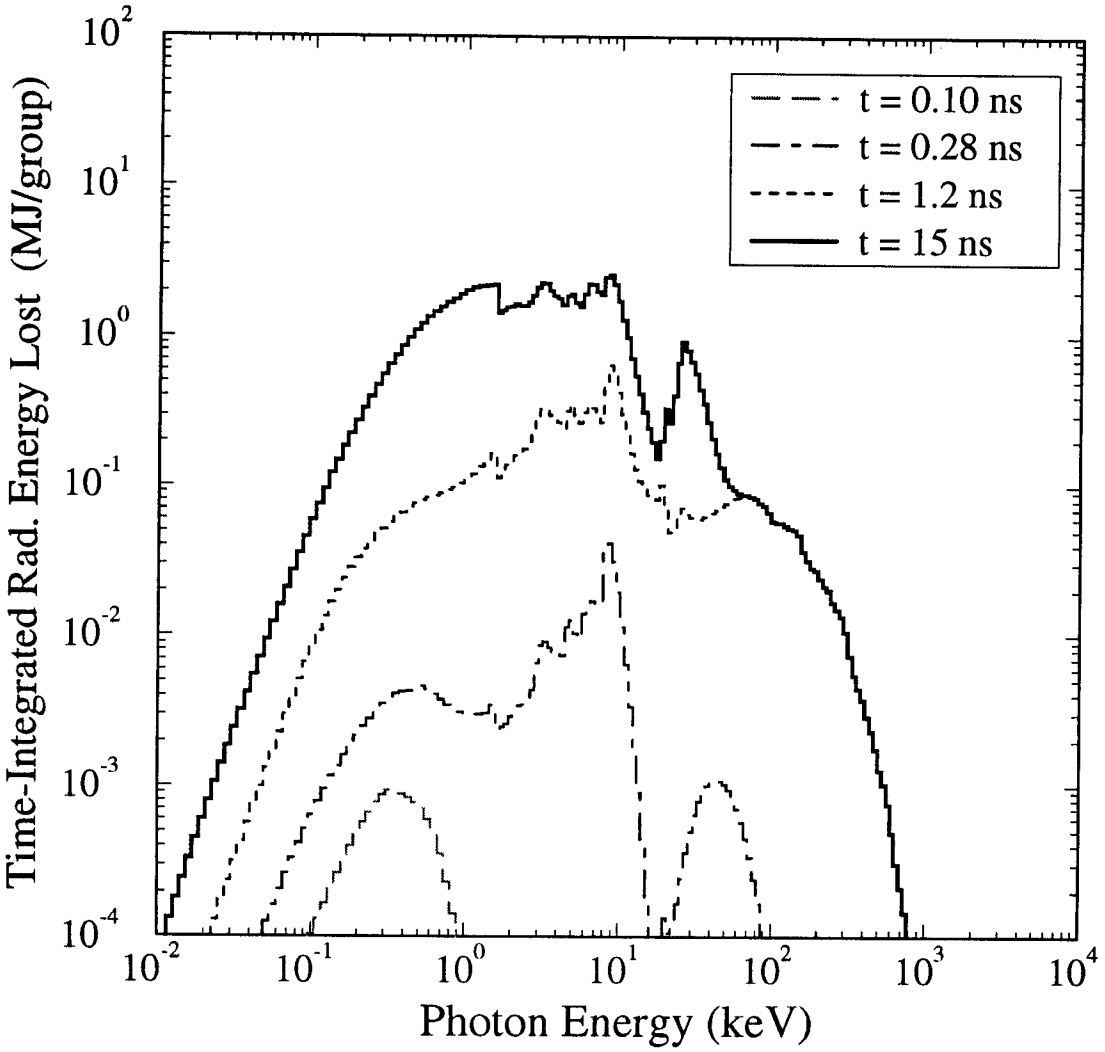

Figure 4.10. Time-integrated spectra of radiation emitted from the target boundary at several simulation times.

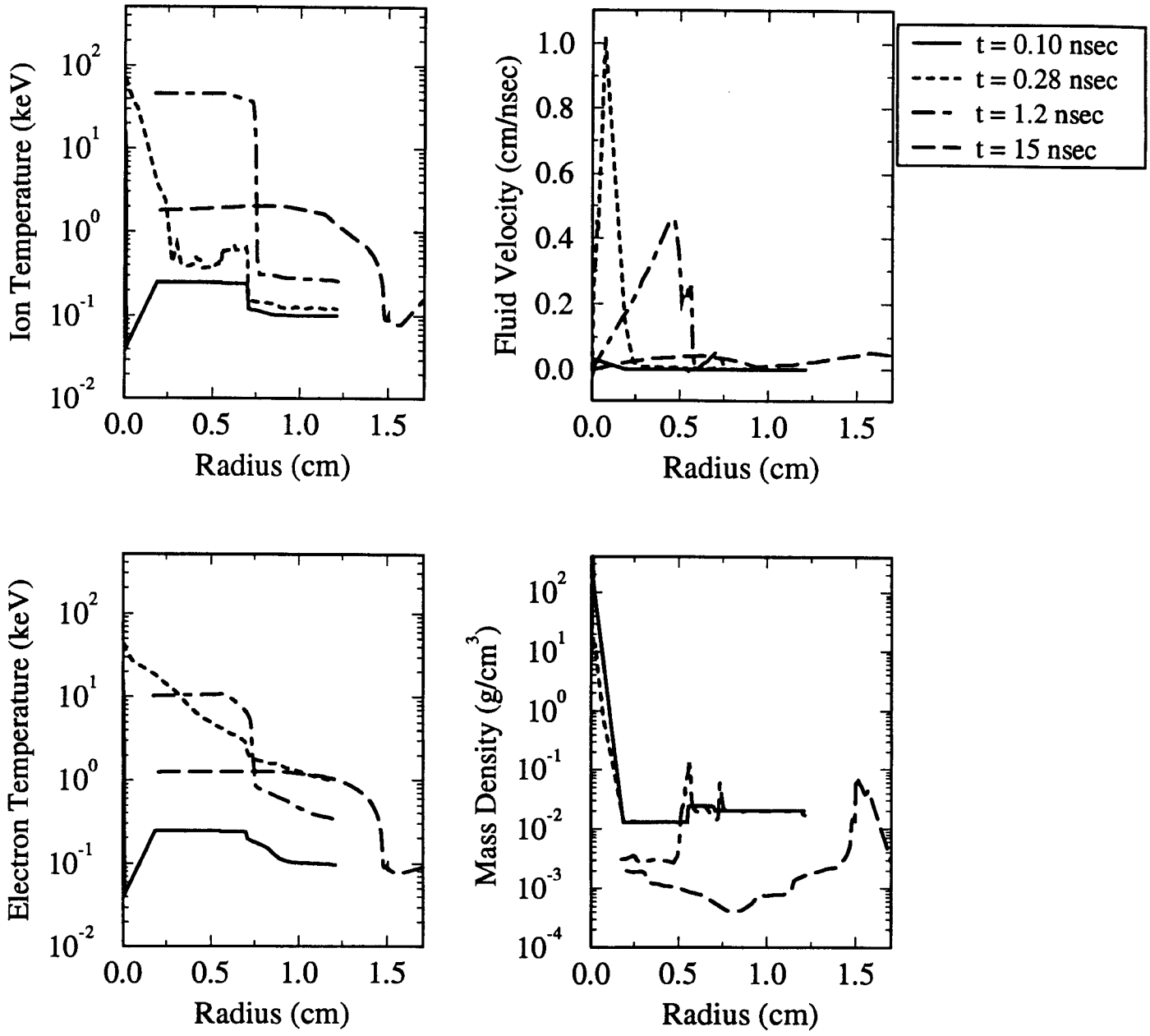

Figure 4.11. Radial profiles of ion temperature, electron temperature, fluid velocity, and mass density at several simulation times.

simulation times. Figure 4.11 shows radial profiles for the ion and electron temperatures, fluid velocity, and mass density at several simulation times.

The fusion burn phase lasts approximately 200 ps and produces a peak ion temperature in the DT fuel of about 300 keV. The DT expands rapidly outward, converting its internal energy into kinetic energy. Note that at 0.4 ns, 98 MJ (or roughly 80% of the total α-particle energy released by the DT fuel) is in the form of kinetic energy (almost all of it in the DT). Figure 4.6 shows a strong shock propagating radially outward through the outer CH, C, and Pb regions. Shortly after the shock enters the Pb region, somewhat more than half of the DT kinetic energy has been converted back into internal energy throughout the target.

The radiation flux from the target is characterized by two main peaks (Fig. 4.8). The first occurs from about 0.2 to 0.5 ns, and is due to hard x-rays emitted directly from the high-temperature DT. By this time, the DT has a significantly larger radius than near the start of ignition, and therefore has a larger radiating surface area. By 1 ns, about 11% of the total α-particle energy generated during the burn phase (i.e., about 13 MJ) escapes the target in the form of hard x-rays. Fig. 4.9 shows that virtually all hard x-rays with $h\nu \gtrsim 50$ keV are emitted by this time.

A burst of softer x-rays is emitted from the target from about 1.5 to 5 ns. These x-rays in large part originate in the Pb region, where electron temperatures reach as high as several keV during this time (see Fig. 4.10). By 5 ns, a total of 85 MJ has been radiated from the target, and by the end of the simulation (t = 20 ns) a total of 97 MJ of radiative energy has escaped the target. The frequency dependence of the escaping radiation (Fig. 4.9) shows the bulk of the radiation comes out between 10^{-1} and 10^{2} keV, with the spectrum being clearly non-Planckian. The structure seen in the spectra is due to the fact that the temperature in the Pb region decreases as the radius increases. These features are thus due to absorption (as opposed to emission), which result from cooler regions absorbing radiation emitted from the higher temperature Pb at smaller radii. In particular, the Pb M-shell and L-shell photoabsorption edges can be seen near 1.6 and 10 keV, respectively.

Table 4.2. Debris Ion Kinetic Energies

Species	Energy (MJ)	Energy per Ion (keV)
H	0.30	0.46
D	0.44	0.69
T	0.101	1.05
He^3	0.047	1.40
C	2.25	10.9
Pb	17.3	309

Table 4.3. Results for LIBRA-SP Target Burn Simulation

	PHD-IV Results	Corrected for Neutron Reabsorption
Total yield	589 MJ	589 MJ
Neutron yield	472 MJ	383 MJ
X-ray yield	97 MJ	1687 MJ
Debris ion yield	20 MJ	35 MJ
Energy lost in endoergic reactions	–	4 MJ

By the end of the simulation a total of 20 MJ remains in the form of kinetic (debris ion) energy. The partioning of the energy between the various target ion species in the PHD-IV simulation is shown in Table 4.2. The debris ion energy, along with the time- and frequency-dependent x-ray spectra, are then used in the LIBRA-SP target chamber simulations to determine the response of the PERIT units and LiPb liquid jet shield to the target explosion. Note that the results listed in Table 4.2 do not include the effects of neutron energy deposition within the target.

The overall partitioning of energy at the end of the PHD-IV simulation is shown in Table 4.3. Also shown in the right column are the values corrected for the redeposition of neutron energy within the target. Details of the neutron transport calculation are discussed in the next section. Overall, approximately 65% of the total energy released by the high-gain target escapes the target in the form of neutrons, while the x-ray and debris ion energy account for 28% and 6% of the energy release, respectively.

Table 4.4. Target Data at Ignition

Region	Material	Density (g/cm^3)	Radius Range (cm)
1	DT	230	0-0.0173
2	CH	0.013	0.0173-0.55
3	C	0.024	0.55-0.6983
4	Pb	11.4	0.6983-0.7

4.4. Target Neutronics

The initial split of energy from a DT fusion reaction is one 14.1 MeV neutron and one 3.5 MeV alpha particle. In an inertial confinement fusion reactor, the DT fuel is heated and compressed to extremely high densities before it ignites. Therefore, neutron fuel interactions cannot be neglected. This results in significant softening of the neutron spectrum as a result of elastic and inelastic collisions with the target constituent materials. In addition, neutron multiplication occurs as a result of (n,2n) and (n,3n) reactions and gamma photons are produced. The energy deposited by the neutrons and gamma photons heats the target and ultimately takes the form of radiated x-rays from the hot plasma and expanding ionic debris.

Neutronics calculations have been performed for the LIBRA-SP target using the one-dimensional discrete ordinates code ONEDANT [17]. The LIBRA-SP target utilizes 5 mg of DT fuel. Although the DT fuel areal density (ρR) value changes during ignition, a value of 4 g/cm^2 is used in the target neutronics calculations. This is representative of the temporal average during ignition and burn. The target data at ignition used in the calculations are given in Table 4.4. The calculations were performed using spherical geometry and 30 neutron - 12 gamma group cross section data based on the ENDF/B-VI nuclear data evaluation [18]. A uniform 14.1 MeV neutron source was used in the compressed DT fuel zone.

Due to (n,2n) and (n,3n) reactions occurring in the target, 1.073 neutrons are emitted from the target for each DT fusion reaction. These neutrons carry an energy of 11.43 MeV implying that the average energy of neutrons emitted from the target is 10.65 MeV. It is interesting to note that only 61.2% of the neutrons emitted from the target are uncollided

Table 4.5. Nuclear Energy Deposition in Target

Region 1	2.53896 MeV/DT fusion
Region 2	0.00345 MeV/DT fusion
Region 3	0.00039 MeV/DT fusion
Region 4	0.00002 MeV/DT fusion
Total	2.54282 MeV/DT fusion

14.1 MeV neutrons. For each DT fusion reaction, 0.0005 gamma photons are emitted from the target with an average energy of 2.4 MeV. The energy spectra of neutrons and gamma photons emitted from the LIBRA-SP target are shown in Figs. 4.12 and 4.13, respectively.

The total energy deposited by neutrons and gamma photons in the target was calculated to be 2.543 MeV per DT fusion. Almost all of the energy is deposited in the DT fuel zone as demonstrated by the results in Table 4.5. This is a direct result of the relatively large ρR value for the DT fuel region. When the 3.5 MeV energy carried by the alpha particle emerging from the fusion reaction is added, a total energy of 6.043 MeV per DT fusion is found to be carried by x-rays and target debris following the microexplosion. Performing an energy balance for the target indicates that 0.127 MeV of energy is lost in endoergic reactions per DT fusion. The detailed partitioning of the energy produced from the target is listed in Table 4.6. For the LIBRA-SP DT fuel yield of 589 MJ, the target yield is calculated to be 584.8 MJ. The neutron and gamma yields are 382.5 and 0.04 MJ, respectively, while the combined x-ray and debris yield is 202.3 MJ.

4.5. Discussion and Future Work

We have performed preliminary calculations for the fusion burn and microexplosion of the LIBRA-SP target. Our results predict a total of 589 MJ of fusion energy is released, providing a gain of 82. The energy released in the form of neutrons is 383 MJ (65%). The bulk of this energy, because of the relatively long mean free paths of neutrons, is deposited in the LiPb blanket (PERIT units). Approximately 28% (167 MJ) of the target energy is

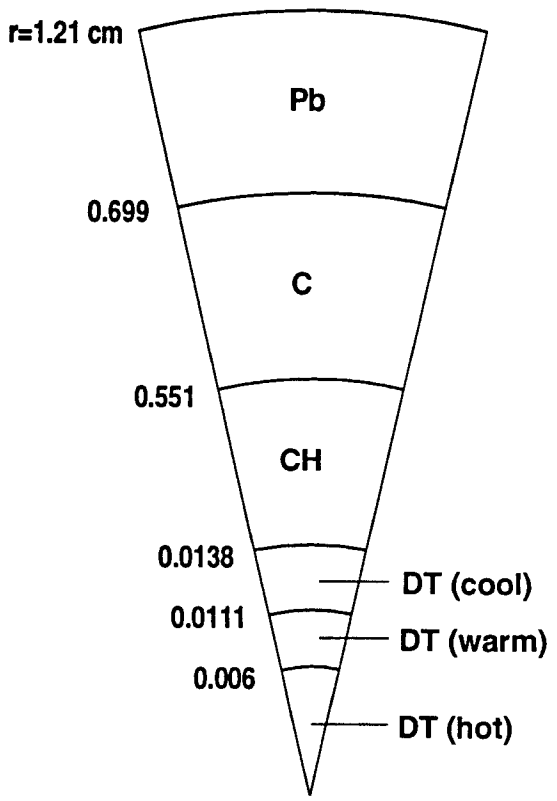

Mass (mg)	Material	T (keV)	ρ (g/cm^3)
120	Pb	0.1	0.020
17.4	C	0.25	0.024
9.1	CH	0.25	0.013
4.2	DT (cool)	0.1	800
0.8	DT (warm)	0.5	166
0.0045	DT (hot)	8	50

Figure 4.6. Conditions at the start of ignition assumed for the PHD-IV LIBRA-SP simulation.

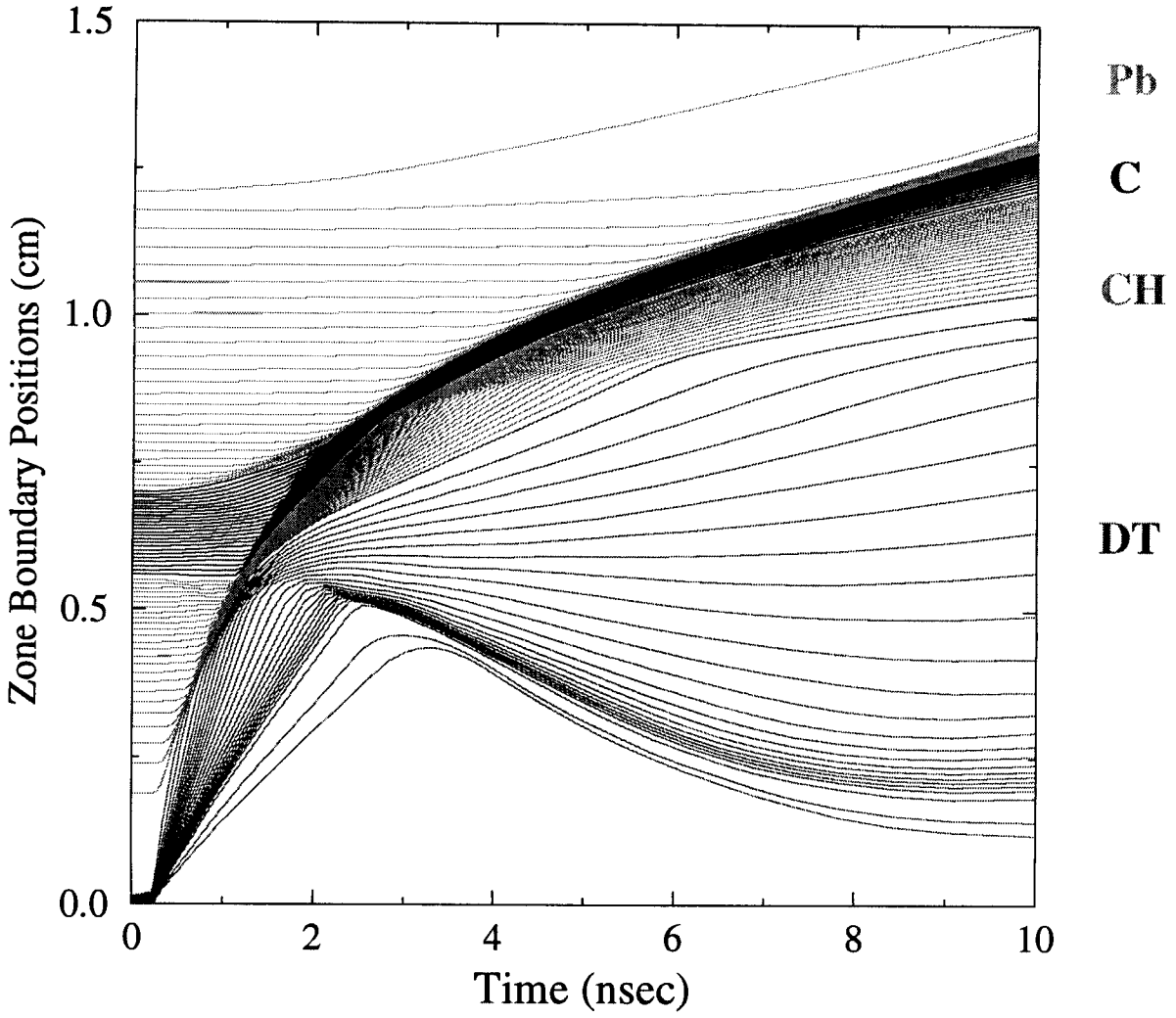

Figure 4.7. Time-dependence of Lagrangian zone boundaries.

Table 4.6. Energy Partitioning from LIBRA-SP Target

Fusion energy	17.6 MeV/DT fusion
Energy carried by neutrons	11.429 MeV/DT fusion (64.94%)
Energy carried by gamma photons	0.001 MeV/DT fusion (0.006%)
Energy carried by x-rays and debris	6.043 MeV/DT fusion (34.34%)
Energy lost in endoergic reactions	0.127 MeV/DT fusion (0.72%)

emitted in the form of x-ray radiation, while 6% (35 MJ) is released in the form of debris ion kinetic energy. The x-ray and debris energy is stopped within the first few microns of the LiPb liquid jets located in front of the PERIT units. The response of the jets to the target x-ray and debris will be addressed elsewhere.

The purpose of these calculations has been to make quantitative predictions for the release of energy from high-gain ICF targets. However, much work remains to be done. Implosion calculations must be done to determine an accurate picture of the target conditions at the start of ignition. In addition, a more accurate, self-consistent simulation of the fusion target microexplosion requires the modeling of the reabsorption of neutron absorption within the target. It is anticipated that these items will be addressed in future work.

References for Section 4

1. B. Badger et al., "LIBRA – A Light Ion Beam Fusion Conceptual Reactor Design," University of Wisconsin Fusion Technology Institute Report, UWFDM-800 (revised Feb. 1990).

2. B. Badger et al., "HIBALL – A Conceptual Heavy Ion Beam Driven Fusion Reactor Study, Preliminary Report," University of Wisconsin Fusion Technology Institute Report UWFDM-450 and KfK-3202.

3. I. N. Sviatoslavsky, et al., "A Near Symmetrically Illuminated Direct Drive Laser Fusion Power Reactor-SIRIUS-P," Eleventh Topical Meeting on the Technology of Fusion Energy, New Orleans, LA, June 1994.

4. G. L. Kulcinski, et al., "Evolution of Light Ion Driven Fusion Power Plants Leading to the LIBRA-SP Design," Eleventh Topical Meeting on the Technology of Fusion Energy, New Orleans, LA, June 1994.

5. R. Olson, private communication, 1994.

6. G. A. Moses, G. Magelssen, R. Israel, T. Spindler, and B. Goel, "PHD-IV – A Plasma Hydrodynamics, Thermonuclear Burn, Radiative Transfer Computer Code," University of Wisconsin Fusion Technology Institute Report UWFDM-194, Aug. 1985.

7. P. Wang, "EOSOPA – A Code for Computing the Equations of State and Opacities of High-Temperature Plasmas with Detailed Atomic Models," Fusion Power Associates Report FPA-93-8, Dec. 1993.

8. B. Badger et al., "LIBRA-LiTE – A Commercial Light Ion Fusion Power Plant," FPA-91-4 and University of Wisconsin Fusion Technology Institute Report UWFDM-880, Dec. 1991.

9. R. Olson, private communication, 1994.

10. G. A. Moses, R. R. Peterson, and T. J. McCarville, "MF-FIRE – A Multifrequency Radiative Transfer Hydrodynamics Code," *Comput. Phys. Commun.*, **36**, 249 (1985).

R. R. Peterson, J. J. MacFarlane, and G. A. Moses, "CONRAD – A Combined Hydrodynamics-Condensation/Vaporization Computer Code," University of Wisconsin Fusion Technology Institute Report UWFDM-670 (revised July 1988).

11. D. A. Liberman, *Phys. Rev.*, **B20**, 4981 (1979).

12. D. G. Hummer and D. Mihalas, *Ap. J.*, **331**, 794 (1988).

13. C. Bauche-Arnoule, J. Bauche, and M. Klapisch, *Adv. At. Mol. Phys.*, **23**, 131 (1988).

14. P. Wang and J. J. MacFarlane, Third International Opacity Workshop and Code Comparison Study, MPI Quantenoptik, Garching, March 7-11, 1994.

15. C. A. Iglesias, F. J. Rogers, and B. G. Wilson, *Ap. J. Lett.*, **322**, L45 (1987).

16. A. Bar-Shalom, J. Oreg, W. H. Goldstein, D. Sharis, and A. Zigler, *Phys. Rev.*, **A40**, 3183 (1989).

17. R. O'Dell et al., "User's Manual for ONEDANT: A Code Package for One-Dimensional, Diffusion-Accelerated, Neutral Particle Transport," Los Alamos National Laboratory, LA-9184-M, 1989.

18. P. F. Rose, "ENDF/B-VI, The U.S. Evaluated Nuclear Data Library for Neutron Reaction Data," Summary Documentation Report ENDF 201, U.S. National Nuclear Data Center, 1992.

5. Design of PERIT Units

5.1. Overall Design

LIBRA-SP is a conceptual design study of an inertially confined 1000 MWe fusion power reactor utilizing self-pinched light ion beams. There are 24 ion beams altogether. Figure 5.1 is a cross sectional view of the reaction chamber which is an upright cylinder with an inverted conical roof resembling a mushroom, and a pool floor. The vertical sides of the cylinder are occupied with a blanket zone consisting of many perforated rigid ferritic steel tubes with a packing fraction of about 50% through which the breeding/cooling material, liquid lead-lithium, flows. This blanket zone, besides breeding T_2 and converting neutronic energy to thermal energy, also provides protection to the reflector/vacuum chamber so as to make it a lifetime component. The distance from chamber center to the first row of tubes is 4.0 m, the thickness of the blanket zone is 1.25 m and the length of the tubes is 10.6 m in two segments of 5.3 m each. The perforated rigid tubes are called PERIT (Perforated Rigid Tubes) units and are made of solid HT-9 ferritic steel. The idea behind the concept is to make the tubes rigid and not flexible, as in LIBRA-LiTE's INPORT units, so they can withstand shock, and to make them perforated so they can maintain a wetted surface through the jet fan spray. There are two rows of 7 and 8 cm diameter PERIT units arranged at 14 cm between centerlines at midplane in the circumferential direction as well as between rows. These front tubes are configured to totally shadow the rear zone, and the spaces between the rows are determined from dynamic motion considerations. The rear tubes are 15 cm in diameter and there are 7 rows of them. Their sole function is to transport the PbLi which moderates neutrons and breeds T_2. Behind the blanket is a 50 cm thick HT-9 ferritic steel reflector which is also the vacuum boundary. Finally, the whole chamber is surrounded by a steel reinforced concrete shield which varies in thickness from place to place but is nominally 2.7 m.

Figure 5.2 shows the distribution of PERIT units and the shield/blanket zone at midplane. Figure 5.1 also shows vacuum tubes located behind the shield/blanket zone at the chamber midplane. There are six such tubes leading to an expansion tank situated below the reaction chamber. The function of this tank is to provide volume for the vapor to expand

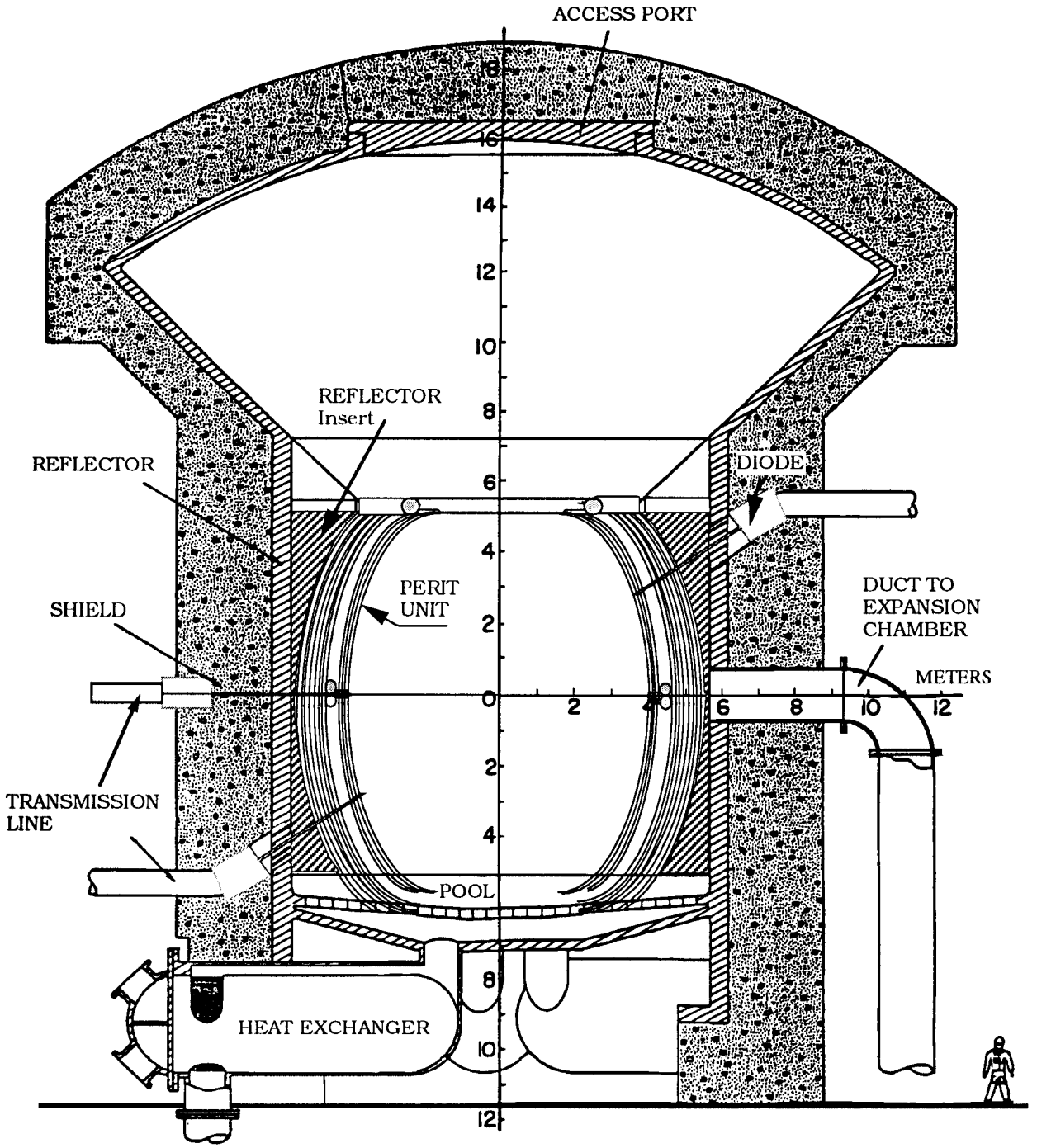

Figure 5.1. Cross-sectional view of the reactor chamber.

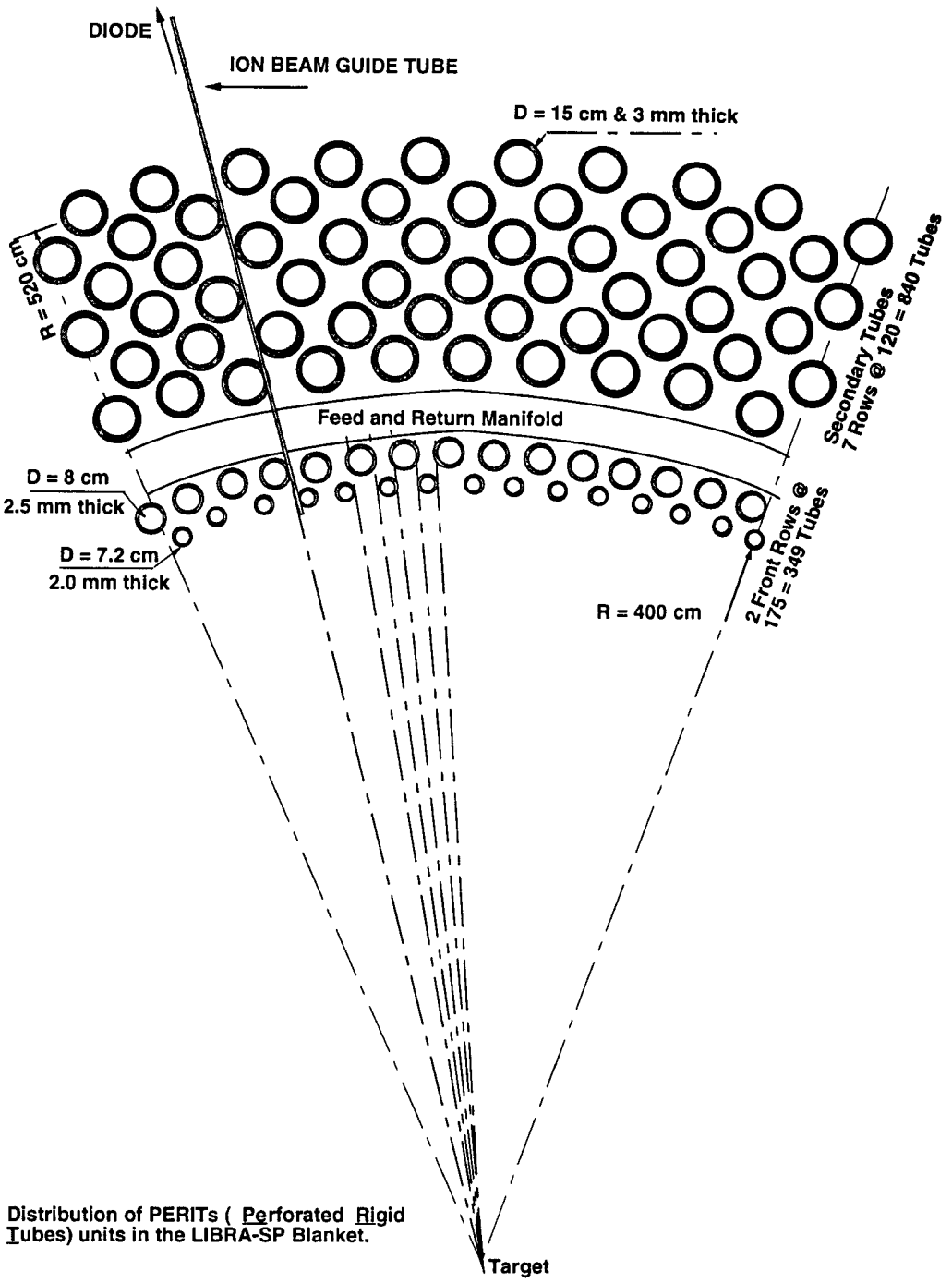

Distribution of PERITs (Perforated Rigid Tubes) units in the LIBRA-SP Blanket.

Figure 5.2. The distribution of PERIT units and the shield/blanket zone.

into, following a shot. As the vapor flows into the expansion tank it exchanges heat with the PERIT units, and cools itself by virtue of an isentropic expansion. Vacuum pumps which are attached to the expansion tank then evacuate the noncondensable species in preparation for the next shot.

The chamber roof is not protected with PERIT units and for this reason is removed to a distance of 16 m from the target, also making it a lifetime component. The roof with its integral shield is designed to be removed to provide access during internal reactor chamber component maintenance. Since the roof will be cooled, it also will condense vapor and have a wetted surface which will be vaporized after each shot. Another function of the mushroom shape is to protect the side walls which are shadowed by the PERIT units and to provide additional volume in the chamber for the vapor to expand into.

Figure 5.3 shows a view of one of the PERITs feed/return arrangement. PERITs are made of ferritic steel HT-9 consisting of two tubes stacked on top of each other; each is 5.30 m long and has an inner bore of 7 cm and an outer diameter of 7.6 cm. Each segment of the cooling tubes has a separate manifold at its top end. The coolant feed pumps only supply the liquid metal to the open liquid tank at the top of each segment group. The liquid metal flows under the effect of gravity down the coolant tubes and through the perforations. A very thin sheet of liquid metal that jets from the tube's perforations (fan sheet spray) is provided at a short distance from the tube to be the first defense against target x-rays and microexplosion debris. Figure 5.4 is a view of three of the PERIT units showing these fan sheet sprays. The rest of the shield/blanket zone is made of ferritic steel HT-9. The PbLi coolant enters the reactor at 370°C and exits at an average temperature of 500°C. After flowing through the PERIT and shield/blanket zone the PbLi collects in the bottom pool. The collected PbLi drains through a perforated plate into a sump leading to the intermediate heat exchangers (IHX) located in the base of the chamber. In the IHX the PbLi exchanges heat with liquid PbLi, which in turn is pumped to a steam generator. A fraction of the PbLi flow is diverted to a T_2 removal system. Steam is used in a double reheat cycle to generate electricity at 43% efficiency.

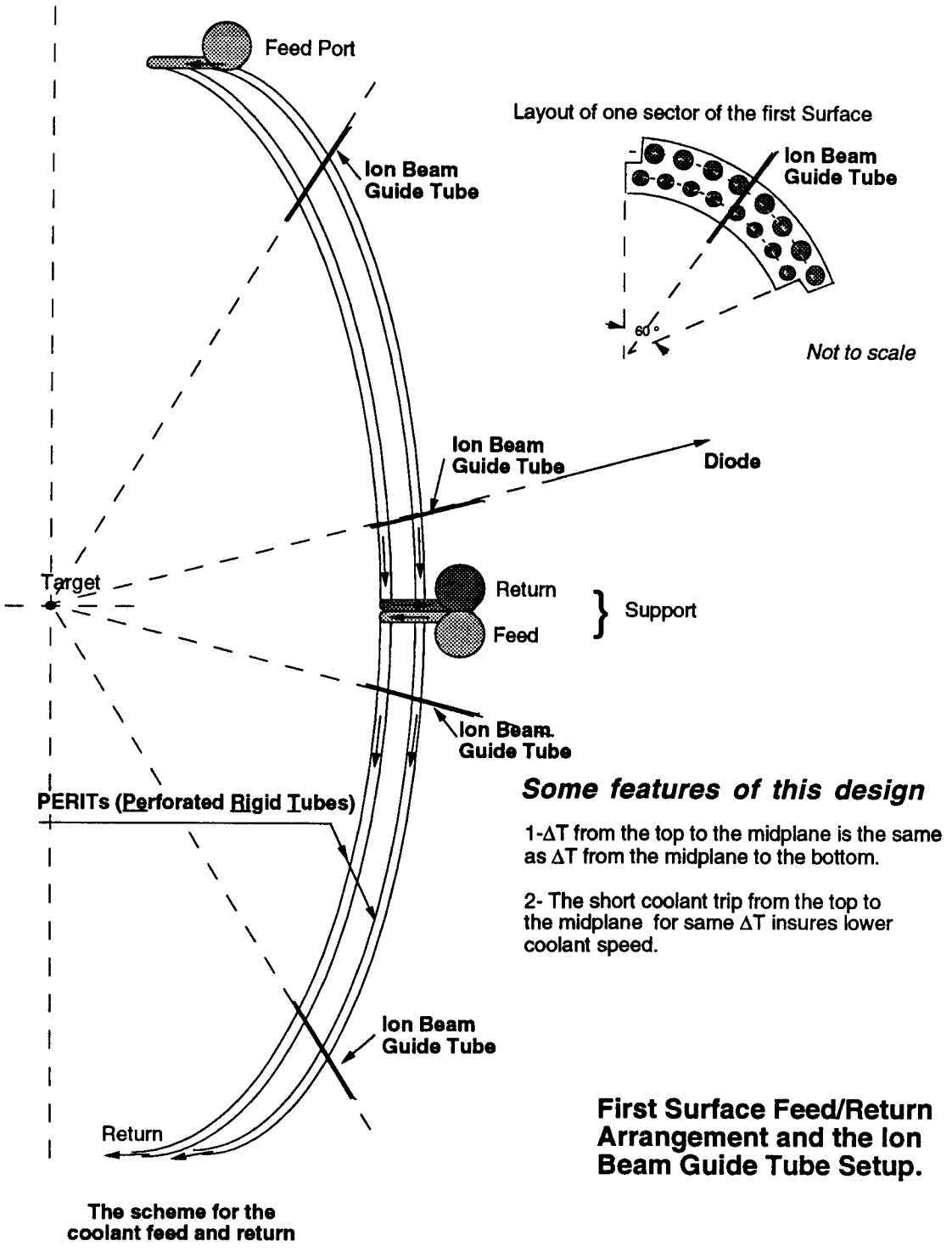

Figure 5.3. First surface feed/return arrangement.

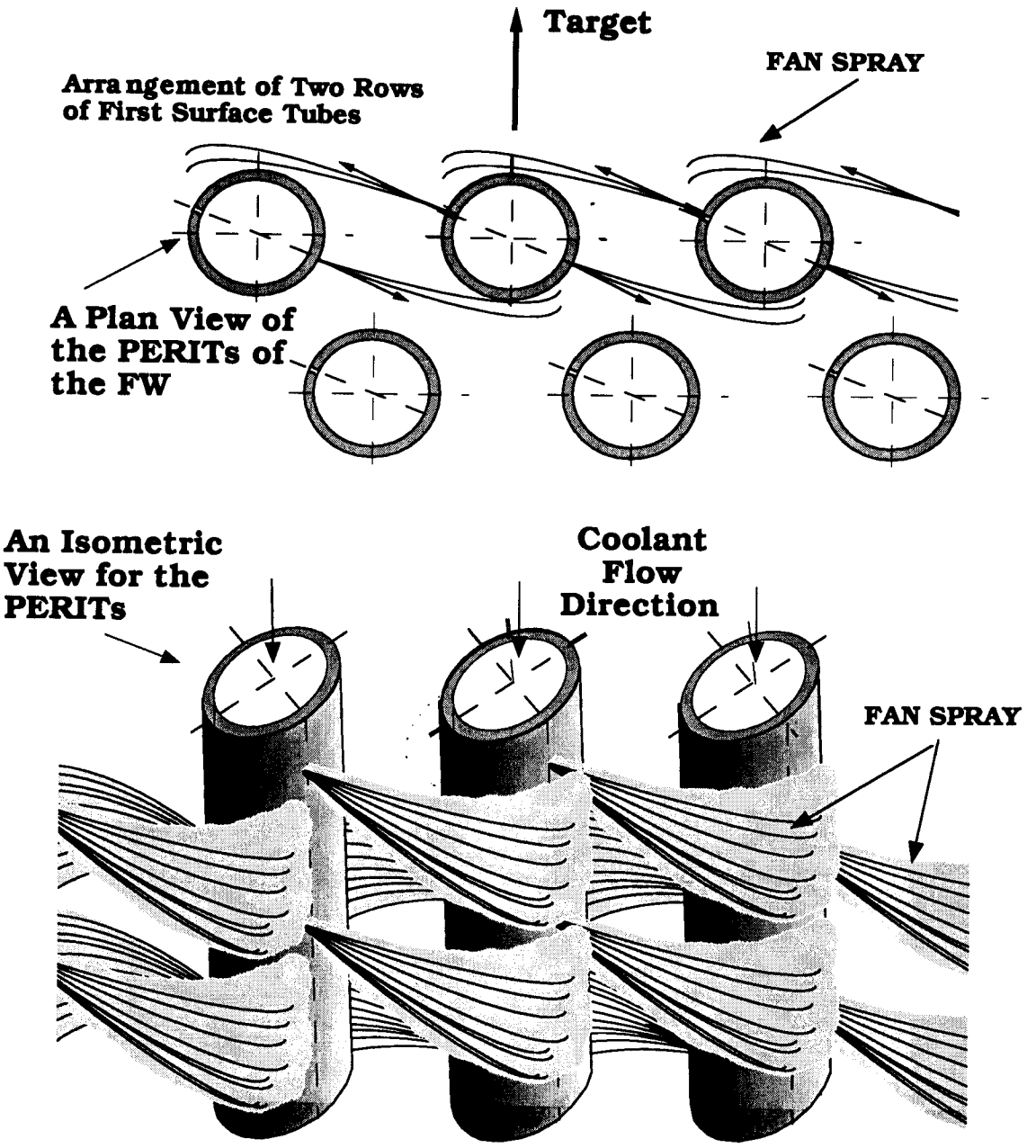

Figure 5.4. First surface protection by fan sheet spray.

5.2. First Surface Protection

5.2.1. Motivation and Introduction

One of the major changes in the LIBRA design is the method used for the first surface protection. In the previous designs of LIBRA and LIBRA-LiTE, we flexible woven steel tubes, INPORT (INhibited flow PORous Tubes) units, are used [1,2,3]. In this way the coolant is allowed to seep through the porous wall of the flexible woven steel tube to keep the coolant tube outer surface wet all the time. The target microexplosion releases x-rays, neutrons and ion debris that deposit in the target chamber vapor and structure. The x-rays are deposited in the liquid metal film on the INPORTs and rapidly vaporizes some of the liquid. This vapor expands into the target chamber exerting a relatively high impulsive load on the INPORTs. To limit the resulting three dimensional motion of the tubes, axial tension must be applied on the INPORTs.

A major motivation for switching from the flexible woven INPORT units to the solid PERIT units is due to the uncertainty with respect to the applied tension needed for the INPORT units. This applied tension is a major input parameter in determining the natural frequency of the INPORT units and, therefore, has control on the mode and the deflection of the oscillations. Not only is it important that the tension is correct from the start of pulsing, but it is imperative that it does not change with time. A small change in the tension could drive the tubes toward the fundamental or a harmonic frequency with dire consequences to the operation of the reactor. It would be impossible to vary the tension of each individual INPORT unit during operation and even more impossible to ascertain that the tension will stay constant over time. Such uncertainty is due to the possibility that the tensioning mechanism will itself loosen, or the material properties of the tubes changing from radiation and other effects. Other second order effects, such as changes in the porosity of the woven material and deviation from a circular tube shape, have also been taken into account in making the switch from woven to solid tubes.

5.2.2. Recent Work and Discussion

LIBRA-SP uses solid coolant tubes for the first surface, blanket and shield to improve the performance of the target chamber. Shortening the coolant tube span will improve both mechanical and thermal hydraulics characteristics of the first surface tubes.

Formation of Liquid Sheets. Conventional thinking about the formation of liquid sheets may be visualized by considering a fluid that is issuing from an orifice with an elongated exit, or even from a slit, to produce the required liquid sheet which is flattened in the direction of the long axis of the orifice. But, due to surface tension and the eccentricity in the jet cross section the fluid velocity in the direction of the longest axis of the jet cross section is much greater than it is in the perpendicular direction. Energy is conserved and each particle then travels at a constant speed. Due to differences in pressure between the jet center and the jet free surface, the jet eventually will transform itself to a diverging jet with its longest axis becoming normal to the original one [4]. Practically this method is not useful.

Liquid sheets are either flat or conical. In this work, our attention will be concentrated on flat liquid sheets.

When two equal cylindrical coplanar jets collide they form an expanding sheet in the plane at right angles to the line containing their axes. If the two jets are coaxial the sheet is symmetrical so that its thickness at any point depends only on distance from the axis. This condition is sketched in Fig. 5.5 (a). If the jets are coplanar but not coaxial and meet at an angle 2θ the sheet formed is not symmetrical but it is flat and it bisects the angle between them. The sheet expands radially from the region of the collision and extends furthermost in the direction of the component of velocity of the jets in the plane of the sheet. This condition is indicated in Fig. 5.5 (b). As the angle θ decreases the extension of the sheet in the opposite direction decreases and eventually disappears leaving the sheet in the condition shown in Fig. 5.5 (c) [4].

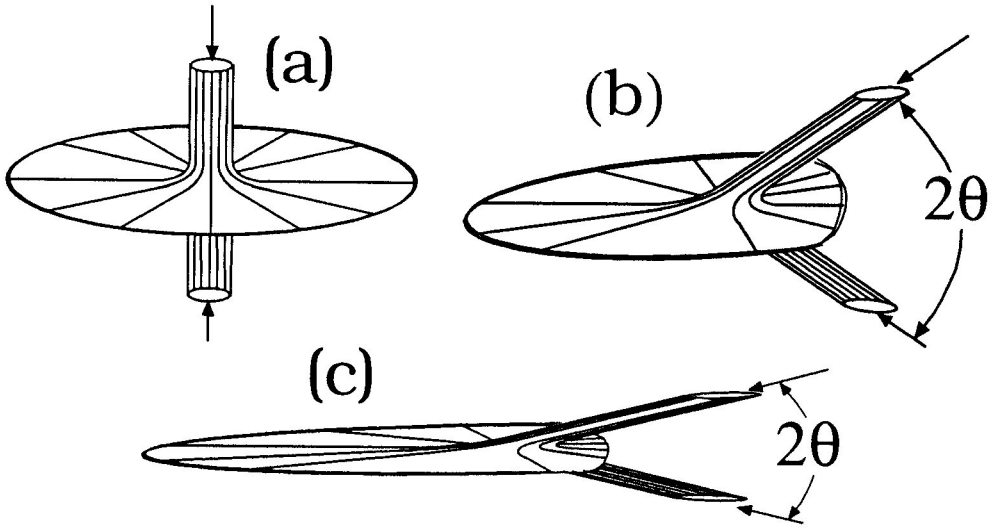

Figure 5.5. Sketch of sheets formed by impact of two cylindrical jets [4].

In practice, in the fan sheet nozzle, two streams of liquid are made to impinge behind an orifice by specially designed approach passages and a sheet is formed in a plane perpendicular to the plane of the streams. The principle is illustrated in Fig. 5.6 (a) which shows liquid flowing through a rectangular orifice formed at the end of the rectangular tube. Under these conditions the flow through the orifice is constricted in only one plane and the streamlines converge to form an origin of pressure behind the orifice. A flat sheet is produced as the liquid freely spreads through the orifice limited only by the side walls. The spreading angle of the sheet can further be increased by extending the opening to the sides of the orifice, as in Fig. 5.6 (b). A commercial nozzle is shown in Fig. 5.6 (c). It is designed on this principle, made of ceramic material and contains a rectangular orifice which is produced by the interpenetration of two rectangular slots.

In the absence of surface tension, the edges of the sheet would travel in straight lines from the orifice so that a sector of a circle would be formed. However, as a result of surface tension, the edges contract and a curved boundary is produced as the sheet develops beyond the orifice. Liquid at the edge moves along the curved boundary, and later becomes disturbed and disintegrates. When this occurs, the resulting drops sustain the direction of flow of the edge at the point at which the drops are formed and remain attached to the

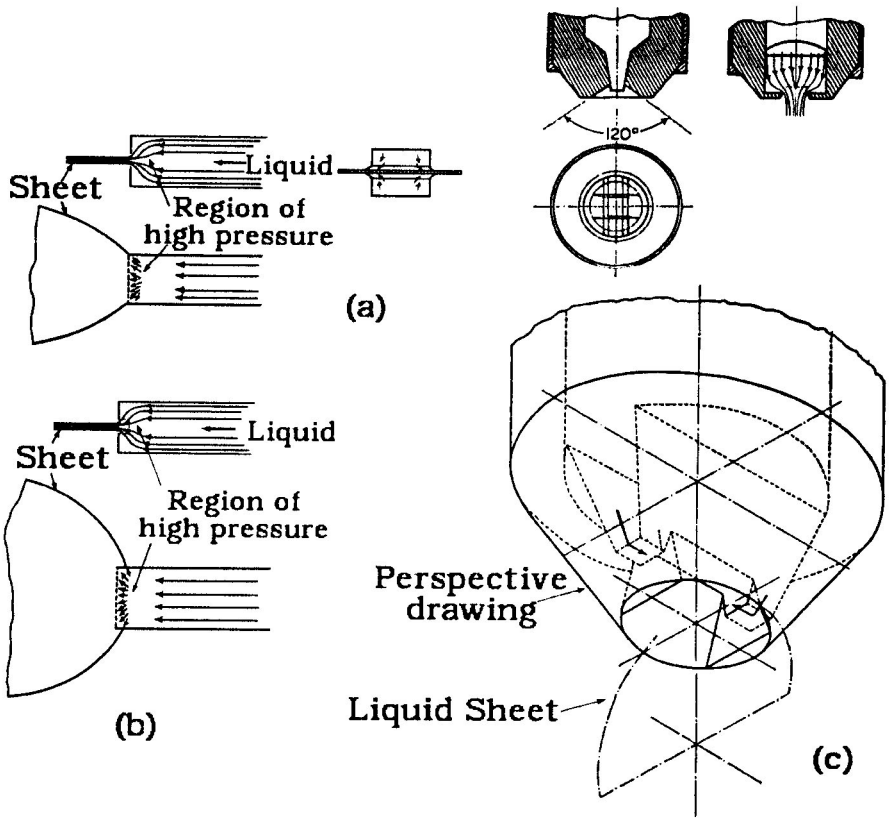

Figure 5.6. Sketch of mechanism of flow through fan sheet nozzles [5].

receding surface by thin threads which rapidly disintegrate into streams of drops (Fig. 5.7) [4]. The breakdown of the edges is restrained by viscosity. At higher injection velocities the contraction is less pronounced, and the placid sheet eventually becomes ruffled, and experiences violent oscillations due to a flag-like instability caused by the reaction of the surrounding gas with the sheet. The sheet then disintegrates before the two edges coalesce.

5.2.3. Analysis of Flow in Sheets

In order to examine the nature of the fluid stream lines in a fan sheet, investigators [4,5] have used photographs of jets containing aluminum particles. Figure 5.7 demonstrates the direction of flow of liquid within the sheet and as it passes through the sheet edges into the ambient atmosphere. Two points of interest can be observed:

1. The sheet streaklines are straight and unaffected by the curved boundaries.

2. The drops leave the edges tangentially at an angle different from that of the streak.

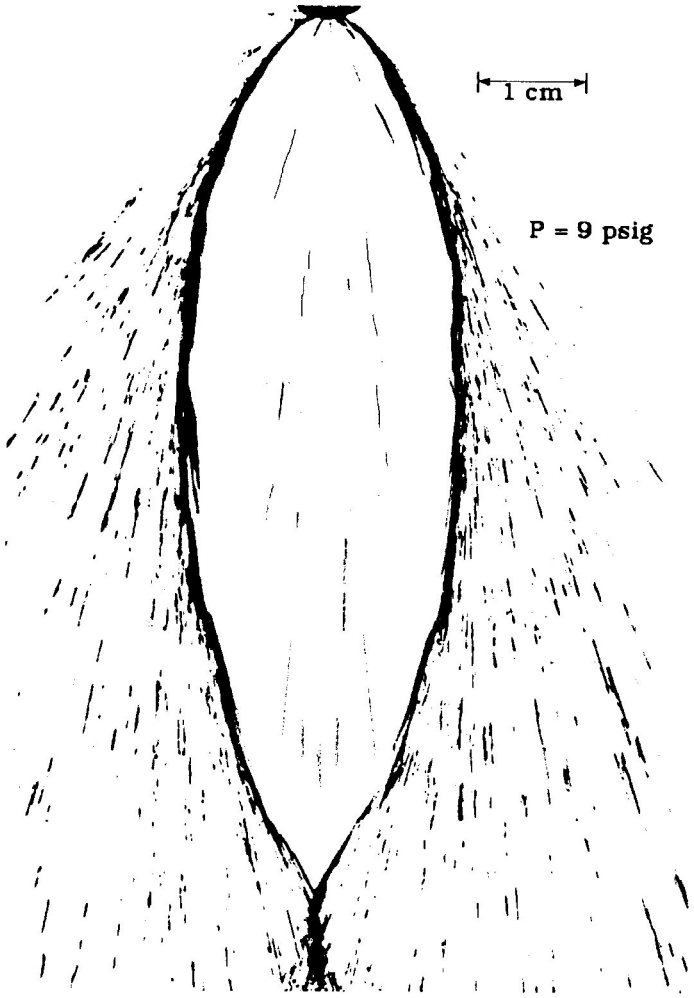

Figure 5.7. Streaklines in a sheet spray.

Measurements from successive photographs with different conditions indicate that the stream velocity is constant along the sheet and its absolute value depends only on the differential injection pressure.

It will be assumed for the following analysis that,

1. The liquid flows from the nozzle as if there were a line of high pressure perpendicular to the sheet.
2. The contraction of the edges by surface tension does not affect the flow pattern of the sheet, i.e. the liquid corresponding to the "vanished" part of the sheet is concentrated at the curved boundary.

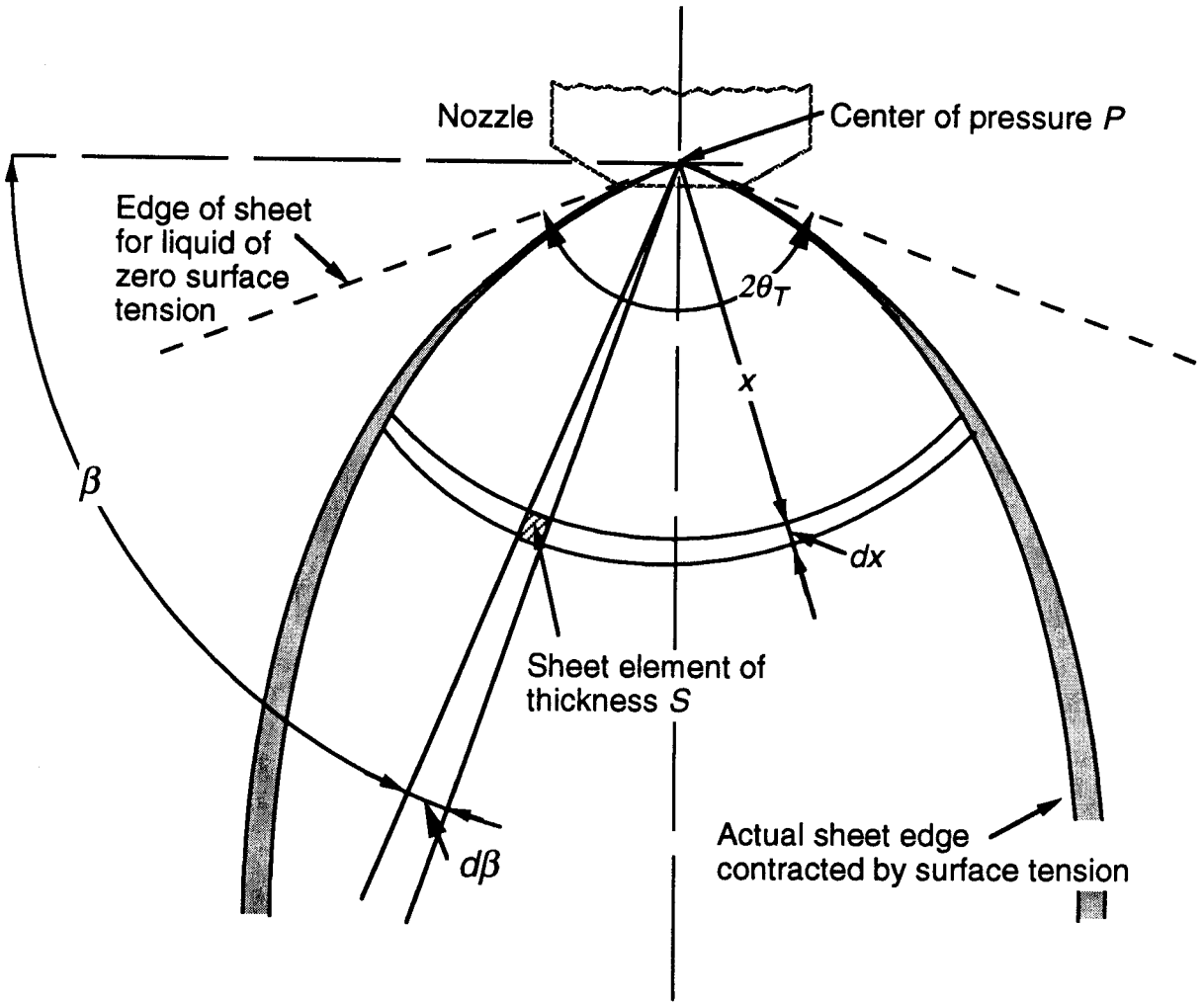

Figure 5.8. Flow parameters in sheet analysis.

Figure 5.8 shows a diagram of this simplified flow pattern. θ_T is the angle at which the sheet edges first issue from the orifice, and x is the radial distance of a point on the edge from the pressure center.

G. I. Taylor [4] and N. Dombrowski, et al. [5] analyzed this problem and the latter reached an approximate expression for the trajectory

$$x = g \cdot P \cdot K \cdot C_Q^2[1 - \sin(\beta + \theta)]/(2\gamma)$$

with a boundary condition of $\beta = \pi/2 - \theta$ as $x \to 0$, where:

g gravitational acceleration

P the differential injection pressure

K constant $= S \cdot x$

S sheet thickness

C_Q orifice discharge coefficient

b the angle defined in Fig. 5.8

g the free surface energy per unit area (surface tension coefficient).

From this simple analysis of the flow it can be seen that θ_T, the sheet angle at the orifice, and the trajectory of the sheet edge may be predicted from a knowledge of the sheet thickness as expressed in terms of K. Then after substitution of the value K, we obtain an expression for the sheet thickness, S:

$$S = (2\gamma)/g \cdot P \cdot C_Q^2 \left[1 - \sin\left(\beta + \theta\right)\right].$$

Using the parameters from Table 5.2 the calculations are performed to design the required nozzle needed to produce a satisfactory liquid metal sheet for LIBRA-SP. Figure 5.9 shows the trajectory of the sheet edge of the liquid PbLi for a 5 mm $\times$ 1.5 mm fan spray nozzle. Figure 5.9 also shows the sheet thickness distribution along the jet with an average value of 37 μm. To get full coverage for the PERIT every consecutive sheet must overlap. The required overlap gives the distance between each consecutive nozzle to be 8 cm.

From the structural dynamics (fatigue) point of view, it is better to have the perforations as close as possible to the bending plane (less stress concentration). Then, the direction of the jet is chosen to make the sheet 1.0 mm away from the surface of the next PERIT. This makes the angle ϕ approximately equals to 13° (Figure 5.9). Exactly on the opposite side of the PERIT there is another system of perforations but staggered 4.0 cm in the vertical direction to complete the coverage of the cavity first surface. The mechanical advantage of having both perforations on the opposite sides is that the lateral jet reaction is canceled.

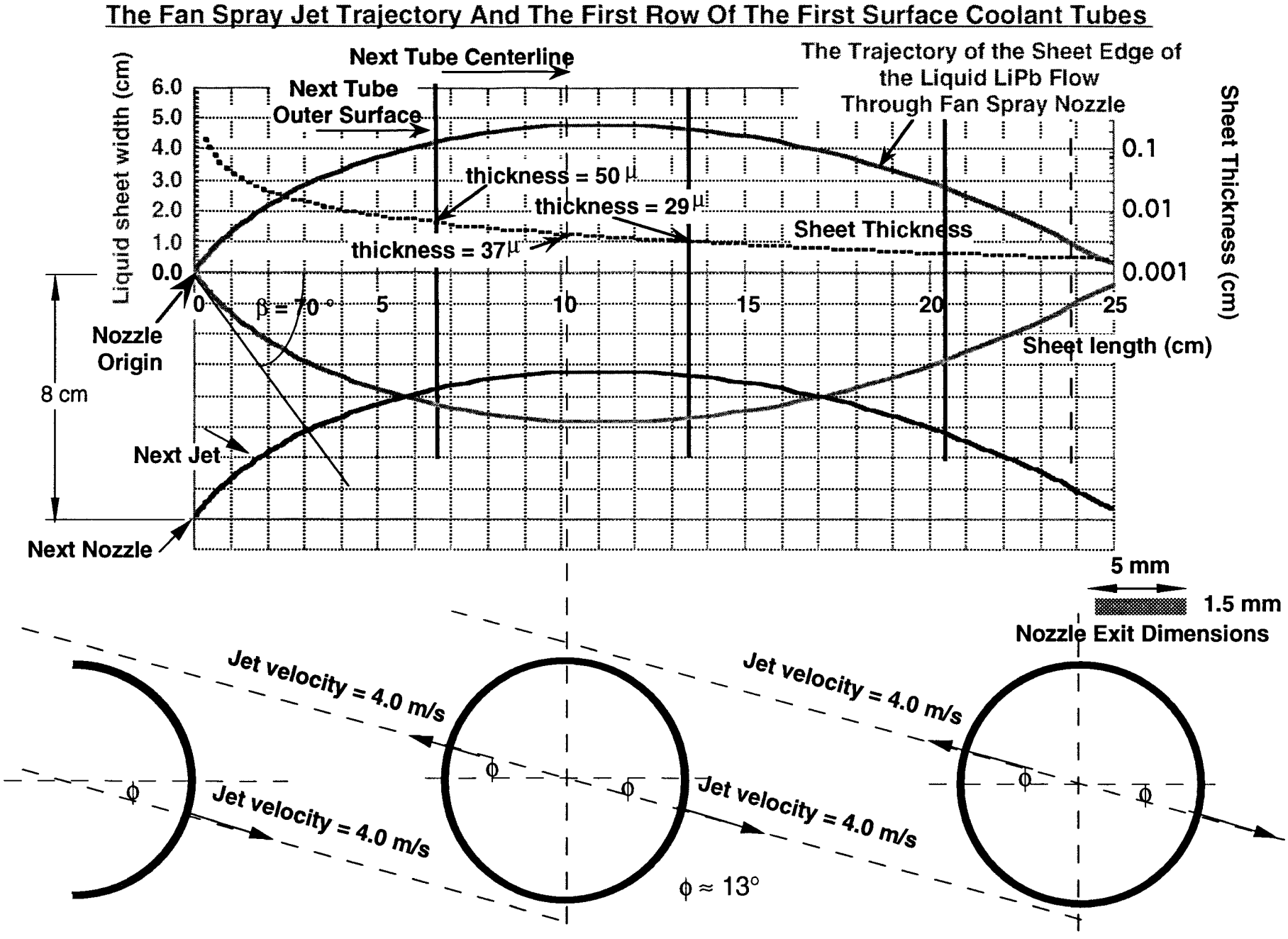

Figure 5.9. The fan spray jet trajectory and the first row of the first surface coolant tubes.

5.3. Mechanical Response

It is expected that the first two rows of PERIT units will be subjected to the radial impulse load from the blast wave. It is assumed that the pressure load is uniformly distributed over the length of the tube and is applied at the rep rate of the reactor. The primary response of the tube will be a radial displacement (or planar displacement), however, it has been shown that the tubes could begin to "whirl" under certain operating conditions. If three-dimensional motion were to take place, it is assumed that the maximum displacement would not be greater than the maximum planar displacement, therefore characterizing the planar motion (and the resulting stresses) was the focus of this study.

The general equation of motion describing the mechanical response of the PERIT units under sequential impulse loadings can be expressed as

$$EI\,\frac{\partial^4 y}{\partial x^4} + \gamma\frac{\partial^2 y}{\partial t^2} + c\frac{\partial y}{\partial t} = 2RI_p \sum_{n=0}^{n\tau_{imp}\le t} \delta(t - n\tau_{imp})$$

$$\begin{aligned}
y &= \text{radial displacement coordinate}\\
x &= \text{spatial coordinate}\\
t &= \text{time}\\
E &= \text{modulus of elasticity}\\
I &= \text{area moment of inertia}\\
\gamma &= \text{mass per unit length of the beam}\\
c &= \text{coefficient of viscous damping per unit length}\\
R &= \text{radius of the beam}\\
I_p &= \text{impulse pressure.}\\
\tau_{imp} &= \text{impulse period.}
\end{aligned}$$

Using separation of variables and assuming the tubular units are clamped (or "fixed") at both ends, the homogeneous solution is given by :

$$\begin{aligned}
y_h(x,t) &= \sum_{i=1}^{\infty} q_i(t)\,\phi_i(x)\\
q_i(t) &= C_i\, e^{-\zeta_i\omega_i t}\,\sin((\omega_d)_i\, t + \phi_i)\\
(\omega_d)_i &= \omega_i\sqrt{1-\zeta_i^2}\\
\omega_i &= k_i^2\sqrt{\frac{EI}{\gamma}}
\end{aligned}$$

$$\begin{aligned}
\phi_i(x) &= \cosh(k_i x) - \cos(k_i x) - \alpha_i(\sinh(k_i x) - \sin(k_i x)) \\
k_i L &= 4.73004074,\ 7.85320462,\ \cdots \\
\alpha_i &= 0.982502215,\ 1.000777312,\ \cdots
\end{aligned}$$

where k_i and α_i are separation constants [6], C_i and ϕ_i are integration constants, L is the length of the beam and ζ_i represents the modal damping. If the tube is initially at rest, the homogeneous solution is equal to zero. Variation of parameters can then be used to find the particular solution [7]. Consequently, a solution of the following form is assumed:

$$y_p(x,t) = \sum_{i=1}^{\infty} T_i(t)\phi_i(x)$$

where $q_i(t)$ has been replaced by an unknown function $T_i(t)$. Inserting the assumed solution in the governing equation and using the orthogonality property of the shape functions, $\phi_i(x)$, it can be shown that

$$\begin{aligned}
T_i(t) &= \frac{4RI_p\alpha_i}{\gamma L k_i(\omega_d)_i}\left[1-(-1)^i\right] q_i^*(t) \\
q_i^*(t) &= \sum_{n=0}^{n\tau_{imp}\le t} e^{-\zeta_i\omega_i(t-n\tau_{imp})}\sin\left[(\omega_d)_i\, t - (\omega_d)_i n\tau_{imp}\right].
\end{aligned}$$

Therefore, the general solution for the displacement of the tube starting from rest and driven by sequential impulses is given by

$$y(x,t) = \frac{8RI_p}{\gamma L}\sum_{i=1,3,5,\cdots}^{\infty} \frac{\alpha_i}{k_i(\omega_d)_i}\,\phi_i(x) q_i^*(t)\,.$$

It should be noted that the response solution will be the same considering the impulse loadings as a series of external forcing functions or as increases in the velocity of the tube simulating an initial value problem.

For the PERIT units, the bending stress σ is equal to

$$\sigma(x,t) = Ec\,\frac{\partial^2 y}{\partial x^2}$$

where c is the perpendicular distance from the neutral axes of the tube to the outer diameter. Finally, the general expression for the bending stress along the beam is given by

$$\sigma(x,t) = \frac{8RI_pEc}{\gamma L} \sum_{i=1,3,5,\cdots}^{\infty} \frac{k_i\alpha_i}{(\omega_d)_i}\,\phi_i^*(x)q_i^*(t)$$

$$\phi_i^*(x) = \cosh(k_ix) + \cos(k_ix) - \alpha_i(\sinh(k_ix) + \sin(k_ix))\,.$$

For the proposed LIBRA-SP cavity, a number of the PERIT design parameters have been set by power requirements and heat transfer requirements, e.g., using HT-9 as the tube material and LiPb as the liquid metal. Table 5.1 lists the system parameters that have been used to calculate the mechanical response. In addition, two damping levels (2.0% and 1.0%) were used to show the effect that damping has on the dynamic displacements and stresses. The magnitude of the impulse load was approximated at 150 Pa-s, so calculations were performed using impulse loads of 100 Pa-s and 200 Pa-s. The results scale linearly so the displacements and stresses can be easily determined for any impulse magnitude.

Table 5.1. PERIT System Parameters

Density of HT-9	$\rho_{\mathrm{HT-9}} = 7625$ kg/m^3
Elastic modulus of HT-9	E = 163.0 GPa
Density of LiPb	$\rho_{\mathrm{LiPb}} = 9440$ kg/m^3
Tube diameter	3 cm
Tube thickness	3 mm
Flow velocity	4.0 m/s
Rep Rate	3.88 Hz

The length of the tubes remained as a design parameter to be optimized. Parametric studies were performed to determine the necessary length to preclude resonant conditions and minimize the radial displacements and normal stresses. Figure 5.10 shows the midspan displacement amplitude as a function of the impulse frequency (or rep rate) for a tube span of 5.3 m for a damping level of 2.0%. A maximum allowable displacement of 3.5 cm (to prevent tube interference) has also been noted on the figure. For a rep rate of 3.88 Hz, the absolute displacement of the tube is well below the allowable. The corresponding stresses are given in Fig. 5.11 with the yield strength of the material [8] marked as shown. Both figures illustrate the frequencies or rep rates associated with resonant conditions, i.e., the

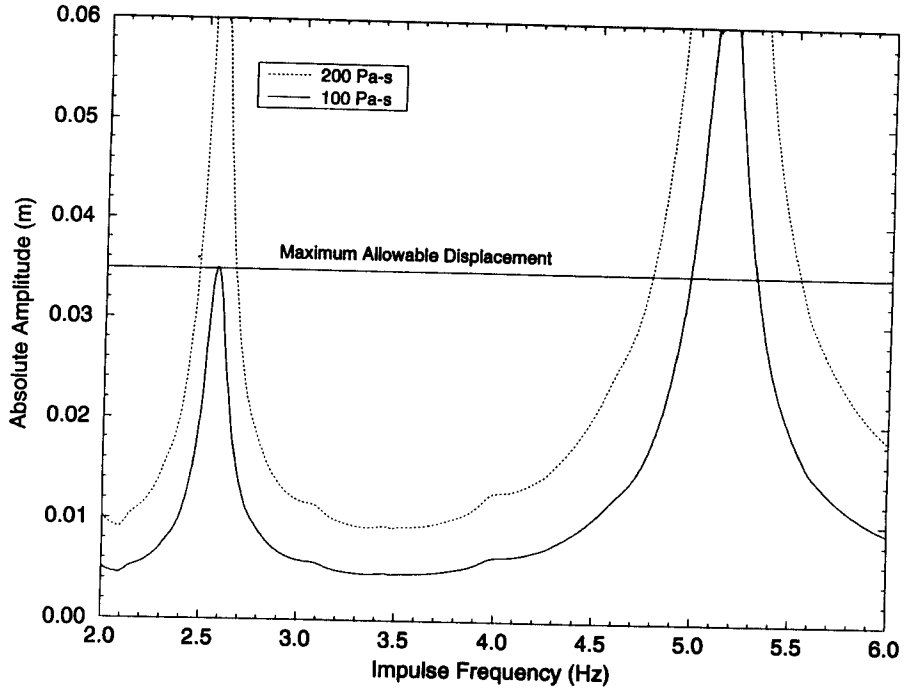

Figure 5.10. Maximum radial displacement of the PERIT units as a function of impulse frequency. Damping has been set to 2%.

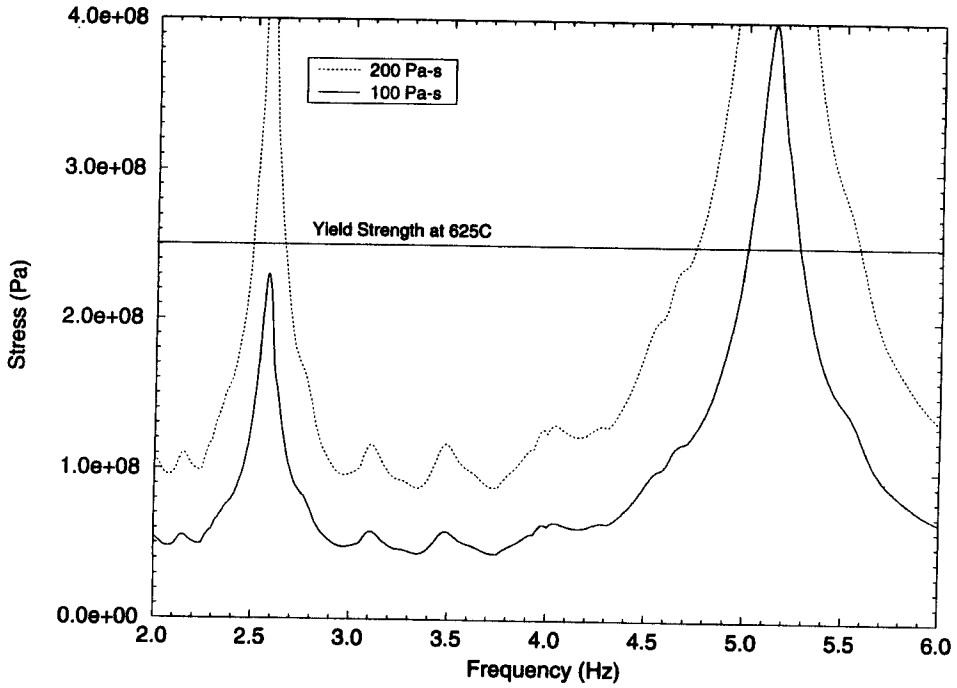

Figure 5.11. Maximum normal stress of the PERIT units as a function of impulse frequency. Damping has been set to 2%.

peaks in the response curves. These peaks would effectively shift if the length of the tube changes. Therefore, it is necessary to establish the free span of the tube at approximately 5.3 m. The effect of lowering the damping level to 1% can be seen in Figs. 5.12 and 5.13. With the higher modes contributing to the response, the curves are not as smooth, however, at a rep rate of 3.88 Hz the actual values of displacement and stress are about the same as with damping at 2%.

5.4. Neutronics Analysis

Neutronics analysis has been performed for the LIBRA-SP chamber using one-dimensional spherical geometry calculations. The discrete ordinates code ONEDANT [9] was utilized along with 30 neutron – 12 gamma group cross section data based on the most recent ENDF/B-VI nuclear data evaluation [10]. A point source is used at the center of the chamber emitting neutrons and gamma photons with the LIBRA-SP target spectrum. The target spectrum takes into account neutron multiplication, spectrum softening and gamma generation resulting from the interaction of the fusion neutrons with the dense target material as discussed in Section 3. The results presented here are normalized to a 589 MJ DT fuel yield and a repetition rate of 3.88 Hz which correspond to a fusion power of 2285 MW.

The primary goal of the neutronics analysis performed for LIBRA-SP is to determine the blanket design that satisfies tritium self-sufficiency, large energy multiplication (M), and wall protection requirements. The blanket is made of banks of PERIT tubes with 0.5 packing fraction. The $Li_{17}Pb_{83}$ eutectic with 90% ^{6}Li enrichment is used as breeder and coolant. It flows in tubes which are made of the ferritic steel alloy HT-9. The tubes consist of 8 vol.% HT-9 and 92 vol.% $Li_{17}Pb_{83}$. A 0.5 m thick reflector consisting of 90 vol.% HT-9 and 10 vol.% $Li_{17}Pb_{83}$ is used behind the blanket. A minimum local (1-D) tritium breeding ratio (TBR) of 1.3 is required in the PERIT tubes and reflector. This relatively high TBR is required to achieve overall tritium self-sufficiency with a simple roof design that does not have a breeding blanket. In addition, the PERIT tubes are required to provide adequate protection for the front of the reflector (chamber wall) to make it last for the whole reactor life. In this study, we adopted a conservative end-of-life dpa limit of 150 dpa for the ferritic steel HT-9. Hence,

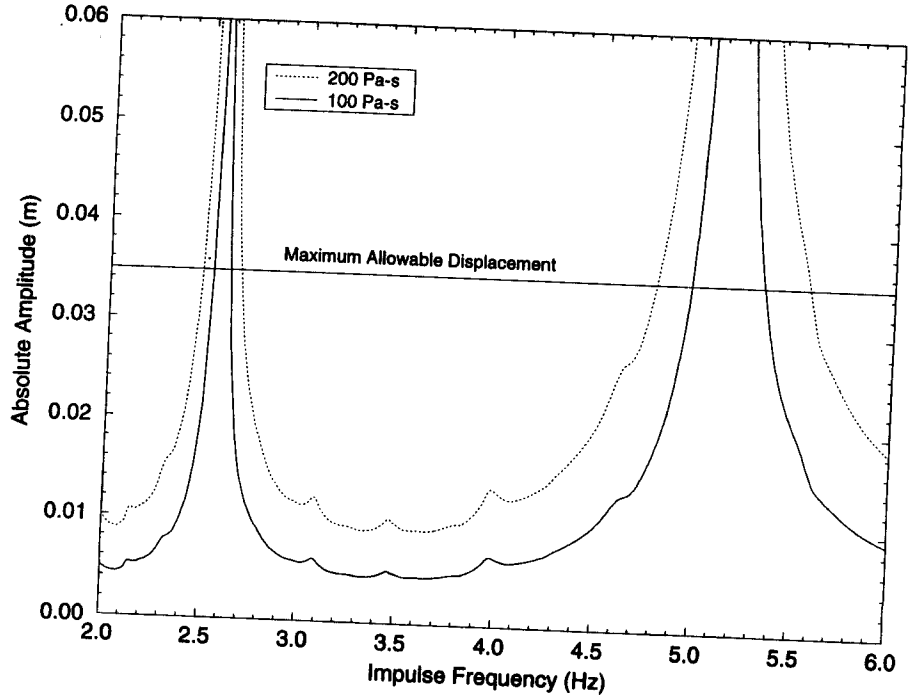

Figure 5.12. Maximum radial displacement of the PERIT units as a function of impulse frequency. Damping has been set to 1%.

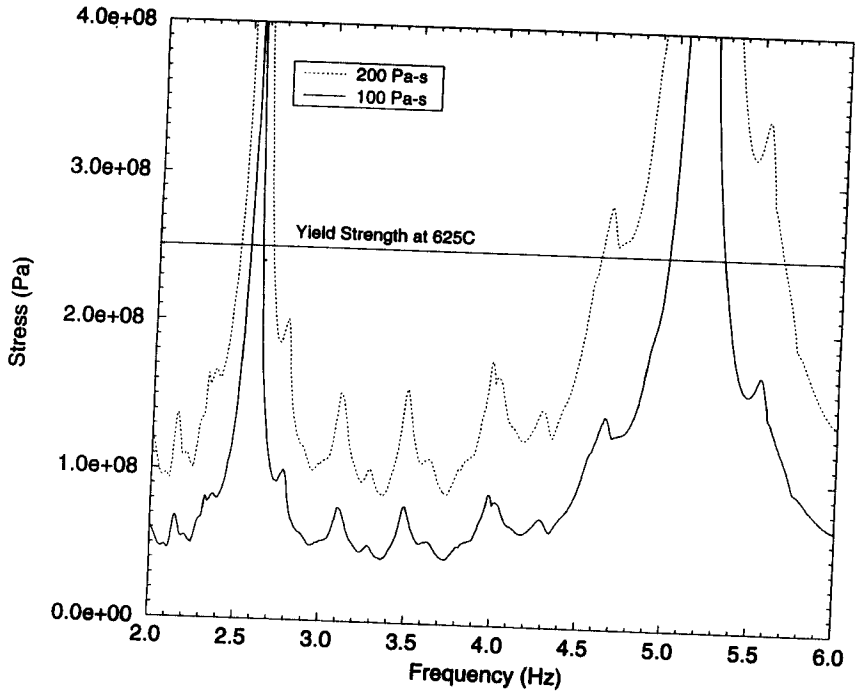

Figure 5.13. Maximum normal stress of the PERIT units as a function of impulse frequency. Damping has been set to 1%.

for 30 full power years (FPY) of operation, the peak dpa rate in the HT-9 chamber wall should not exceed 5 dpa/FPY.

Several calculations have been performed to determine the blanket thickness required for adequate chamber wall protection. This scoping analysis implied that the PERIT tube zone (blanket) should be 1.2 m thick. In the reference LIBRA-SP chamber design, the inner chamber wall radius is 5.2 m. The front surface of the PERIT units is at a radius of 4 m and is exposed to a neutron wall loading of 7.4 MW/m^2.

The peak dpa rate in the PERIT units is 94.2 dpa/FPY implying a lifetime of 1.6 FPY. A gradual reduction in the damage rate and consequently the replacement frequency for the PERIT tubes is obtained as one moves toward the back of the blanket. The peak helium production rate is 436 He appm/FPY. The peak dpa rate in the chamber wall is 4.2 dpa/FPY implying an end-of-life damage of 126 dpa. The chamber will last for the whole reactor life. The peak helium production rate is only 0.9 He appm/FPY. Since spherical geometry has been used in the calculations, the damage rates given above represent the worst case conditions at the midplane of the cylindrical chamber. The radial variation of damage rate in HT-9 at the reactor midplane is shown in Fig. 5.14.

The local TBR is 1.48 and the local blanket and reflector nuclear energy multiplication M_n, defined as the ratio of nuclear heating to the energy of incident neutrons and gamma photons, is 1.292. To take into account the surface energy deposited by x-rays and ion debris and the energy lost in target endoergic reactions, an overall energy multiplication factor (M_o) is defined as the ratio of total power deposited to the DT fusion power. For the target design used here, M_o is related to M_n via

$$M_o = 0.9928\ [0.6541\ M_n + 0.3459]\ .$$

The overall energy multiplication for the reference LIBRA-SP design is 1.182 implying a total power of 2702 MW deposited in the chamber with 785 MW deposited at the front surface of the PERIT tubes and 1917 MW deposited volumetrically in the blanket and shield by neutrons and gamma photons.

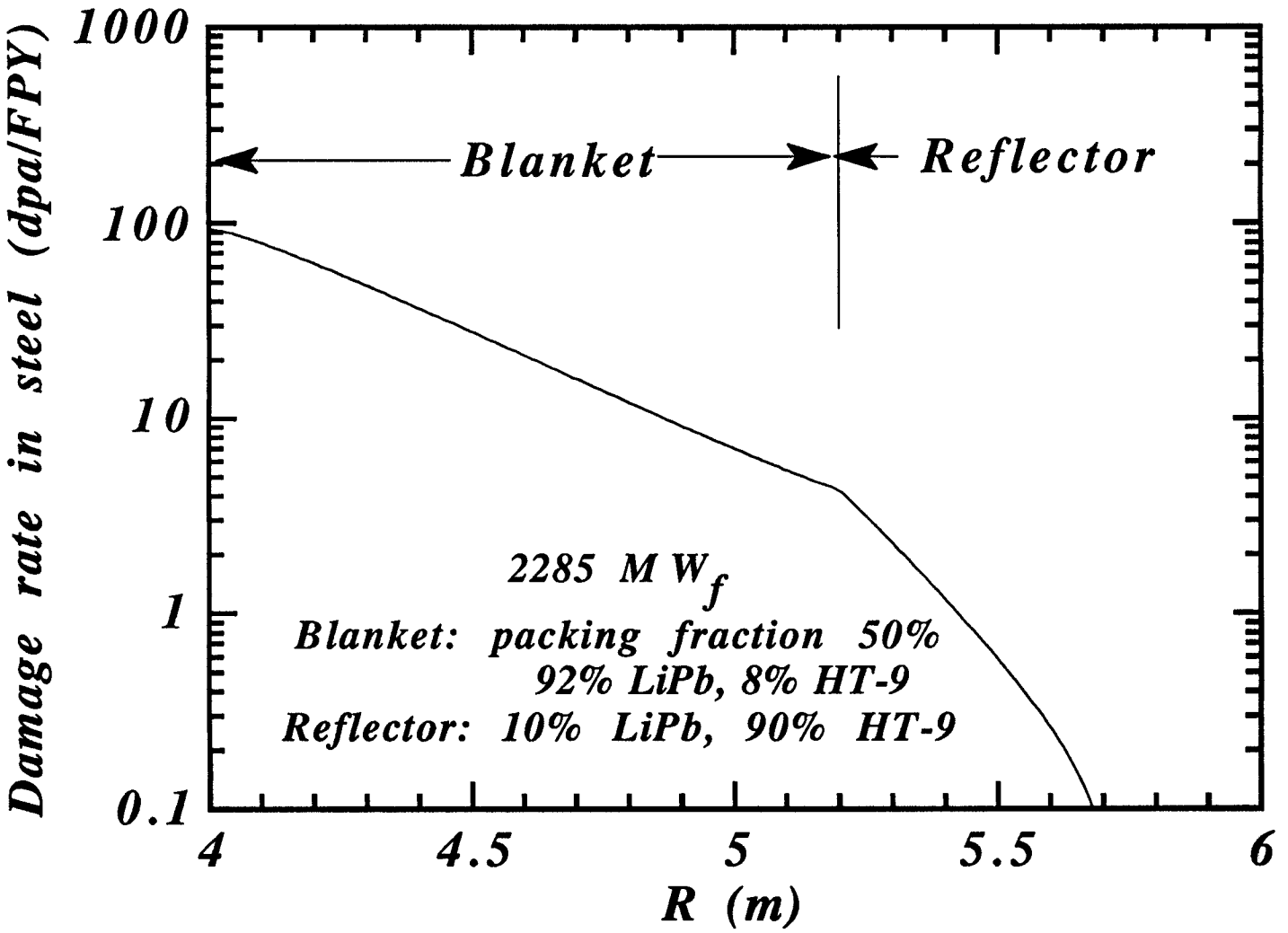

Figure 5.14. Radial variation of damage at reactor midplane.

Table 5.2. Chamber Neutronics Parameters

Inner radius of blanket	4 m
Chamber wall radius	5.2 m
Neutron wall loading	7.4 MW/m^2
Local TBR	1.48
Nuclear energy multiplication, M_n	1.292
Overall energy multiplication, M_o	1.182
Peak dpa rate in PERIT tubes	94.2 dpa/FPY
Lifetime of front PERIT tubes	1.6 FPY
Peak helium production rate in PERIT tubes	436 He appm/FPY
Peak power density in PERIT tubes	18.3 W/cm^3
Peak dpa rate in chamber wall	4.2 dpa/FPY
Peak end-of-life damage in chamber wall	126 dpa
Peak helium production rate in chamber wall	0.9 He appm/FPY
Peak power density in chamber wall	0.52 W/cm^3

The spatial variation of nuclear heating has been calculated for use in the thermal hydraulics analysis. The results at the midplane are given in Fig. 5.15. The power density peaks at 18.3 W/cm^3 in the front PERIT tubes and drops to 2.4 W/cm^3 in the back tubes. The peak power density in the chamber wall is 0.52 W/cm^3. This large drop is due to the large neutronic and gamma attenuation in the enriched $Li_{17}Pb_{83}$ used in the PERIT tube region. Table 5.2 gives a summary of the LIBRA-SP chamber neutronics parameters.

5.5. Thermal Hydraulic Analysis

5.5.1. Introduction

The thermal hydraulics performance of the PERIT tubes and the rest of the blanket/shield zone is discussed in the next section.

5.5.2. Geometry

The PERIT units in the LIBRA-SP blanket have the configuration of a barrel shape surrounding the target at the center of the reactor chamber. The general shape of the reactor chamber is a mushroom-like configuration, the stem being the cooling units, and the head

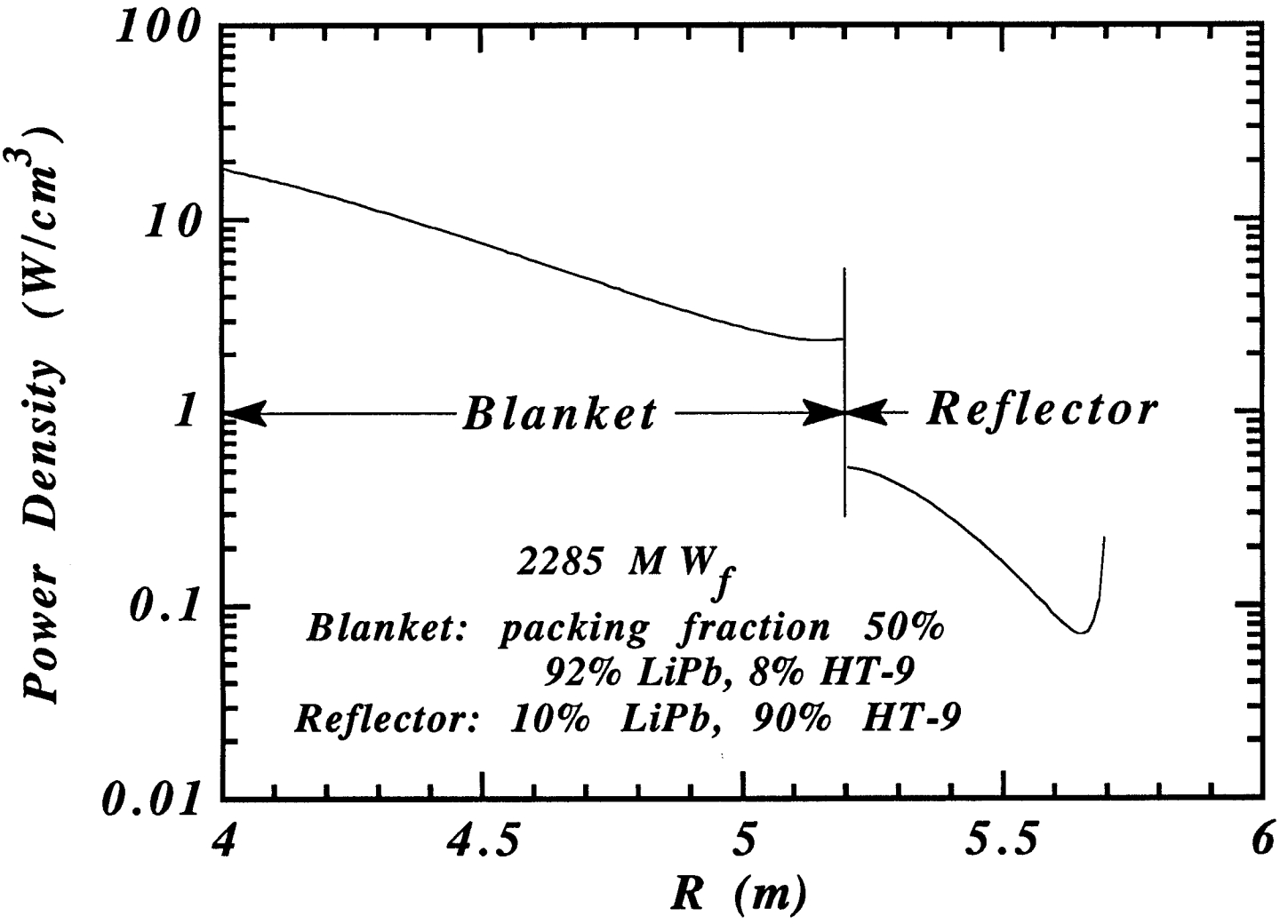

Figure 5.15. Radial variation of power density at reactor midplane.

is the roof (Fig. 5.1). The cooling units consist of two groups. The first one is at the front (PERIT units) and the second are solid curved circular tubes in the back. Both are made of vertically curved ferritic stainless steel, low activation HT-9 tubing. A detailed description of these two groups follows:

- First group: The front group consists of one row of solid perforated metallic tubing. The perforated walls of this system of tubing allow the internal coolant/breeder fluid to jet through the perforated walls and form flat thin vertical sheets of liquid metal as previously described in Section 5.2. Also, it wets the outer surface of the tube. The lead-lithium sheet jet and the wetted wall is designed to protect the metallic material from x-rays, charged particles and target/reaction debris.
- Second group: The secondary tubes consist of 8 concentric rows of solid HT-9 tubing. The first group after the PERITs is staggered to close the gap between the PERIT tubes. The rest are positioned in the back behind the feed and return manifold (Fig. 5.2). It is expected that the lead-lithium vapor will recondense on all of the tube surfaces. The general parameters for the PERIT unit geometry are as follows:

The front (PERIT) group	
Number of rows	1
Number of tubes/row	175
Diameter of each tube (cm)	7.0
Diameter of the first row (cm)	800.0

The second group	
Number of rows	8
Number of tubes/row	175/first - 120/rest
Total number of tubes	1015
Diameter of each tube (cm)	8.0/first - 15/rest

5.5.3. Thermal Hydraulics Calculations

In Section 5.4 the neutronics analysis is given, which utilizes a one-dimensional model to calculate the distribution of the volumetric nuclear heating in the blanket and PERIT unit. Also, in Section 1, results of a one-dimensional hydrodynamics calculation are given which determines the cavity performance and accounts for the effects of vaporization/condensation processes on the surface heat flux. The steady state nuclear heating distribution at the midplane is shown in Fig. 5.15. For thermal hydraulics calculations consider the following thermal load assumptions of the first surface (FS) of the LIBRA-SP reactor:

- The first surface is the first two rows of the coolant tubes (the first 20 cm of the blanket).
- According to the spatial distribution of the neutron heating, nearly 37% of the total neutron heating is generated in the first 20 cm of the blanket.
- All X-ray and debris power is consumed in evaporating PbLi (6.62 kg per shot).
- All PbLi vapor eventually will recondense on the first surface only and cools down to 620°C.

Table 5.3 presents the results, using these assumptions.

Figure 5.16 shows the temperature variation and variation of coolant speed in the first row of PERIT units. Figure 5.17 shows the maximum temperature in the HT-9 of the first row of PERIT units. The maximum surface temperature of the HT-9 is chosen not to exceed 625°C to avoid the rapid decline in the HT-9 mechanical properties. Figure 5.18 shows a graph of the heat transfer coefficient used for liquid metal (PbLi) at a temperature of 400°C and tube diameter of 7.0 cm. Figures 5.19, 5.20 and 5.21 show the material data base used for liquid metal (PbLi) here and in Section 5.2. Figure 5.22 shows a graph of the material data base used for structural material (HT-9).

Table 5.3. Thermal Hydraulics Parameters

Number of the coolant tubes in the FS	350
Total surface area (m^2)	1910.6
Weight of evaporated PbLi/shot (kg)	6.62
Thickness of PbLi recondensed per second (mm)	1.35
Heat flux due to recondensation at FS (W/cm^3)	107
Maximum value of volumetric heating at FS (W/cm^3)	38.6
Average nuclear volumetric heating in front tube (W/cm^3)	35.03
Temperature rise in the coolant tube wall	
(HT-9 wall thickness = 3 mm) due to:	
1. Surface heat flux only (condensation) (°C)	117.5
2. Volumetric heating only (°C)	7.5
Total temperature rise in the FS coolant tube wall (°C)	125
Maximum FS coolant velocity (at inlet) (m/s)	4.0
Minimum FS coolant velocity (at exit) (m/s)	2.9
Inlet FS coolant bulk temperature (°C)	370
Exit FS coolant bulk temperature (°C)	430 (32.32×10^4 kg/s)
Average coolant bulk temperature of outside coolant (°C)	650 (12.26×10^4 kg/s)
Exit blanket coolant bulk temperature (°C) (V = 17.4 cm/s)	600 (5.23×10^4 kg/s)
Total mass flow rate (kg/s)	49.78×10^4
HX inlet coolant bulk temperature (°C)	502
Pumping power (inside cavity) (MW)	47.61

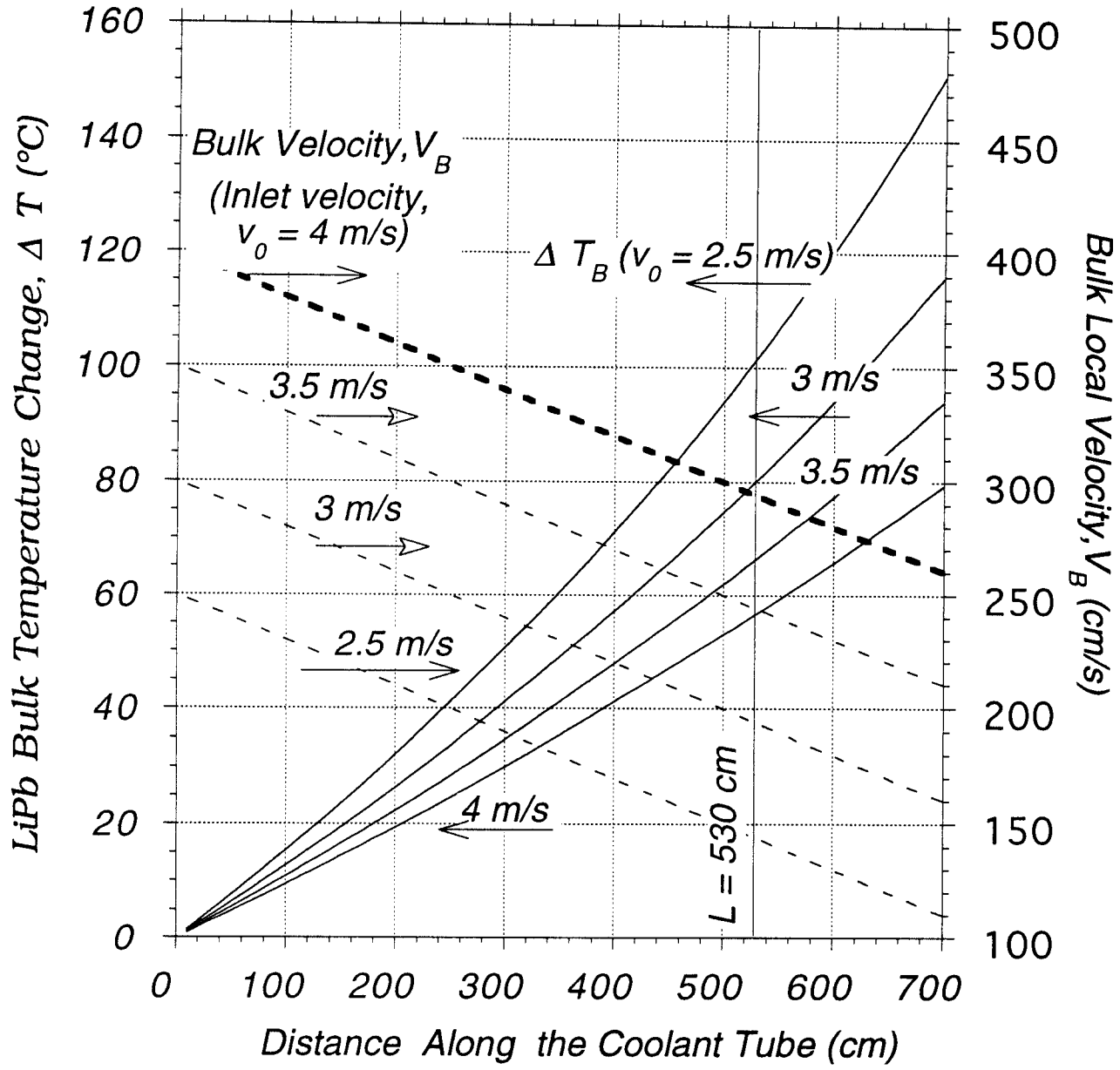

Figure 5.16. The temperature variation and variation of coolant speed in the first row PERITs.

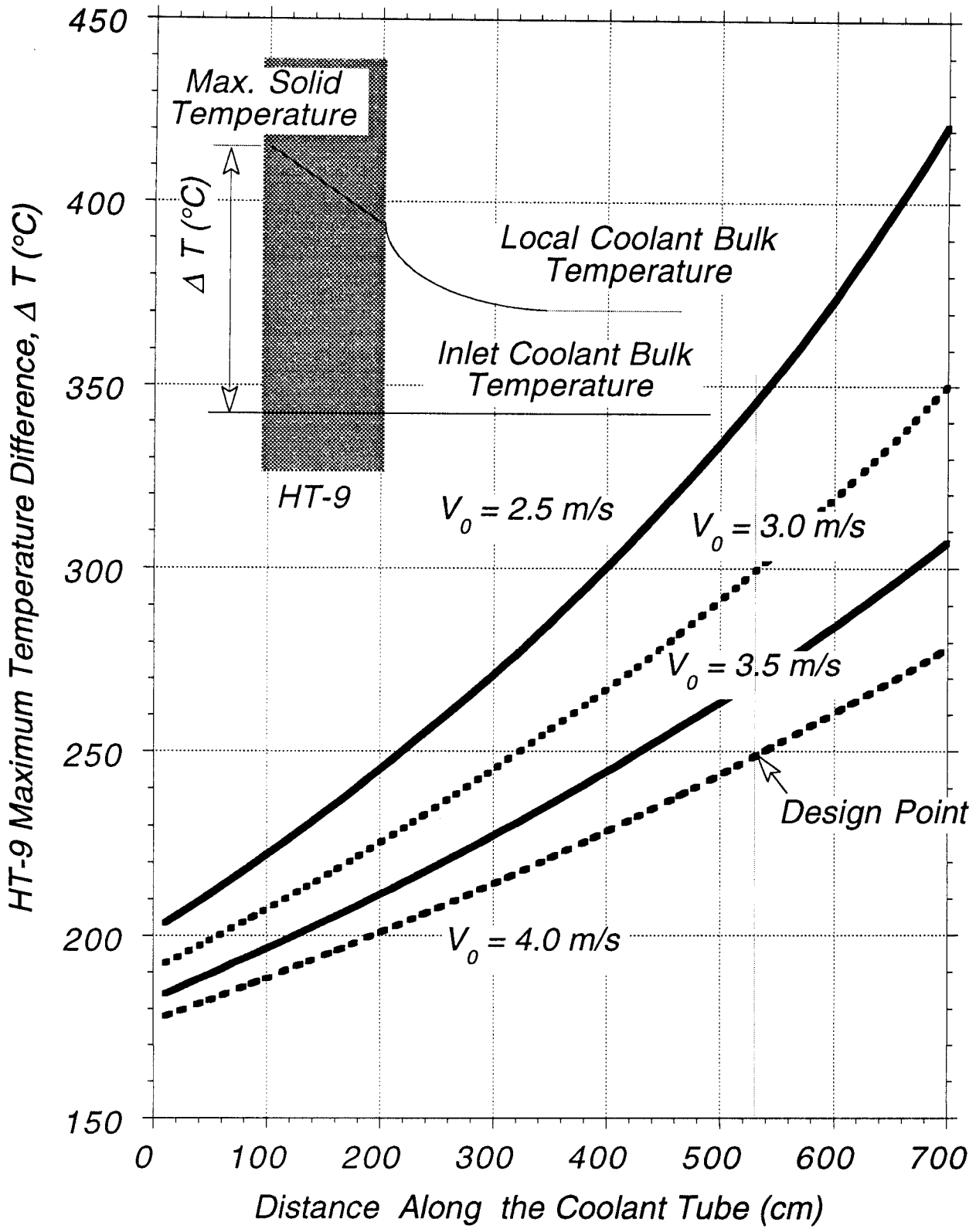

Figure 5.17. Maximum temperature in the HT-9 of the first row PERIT.

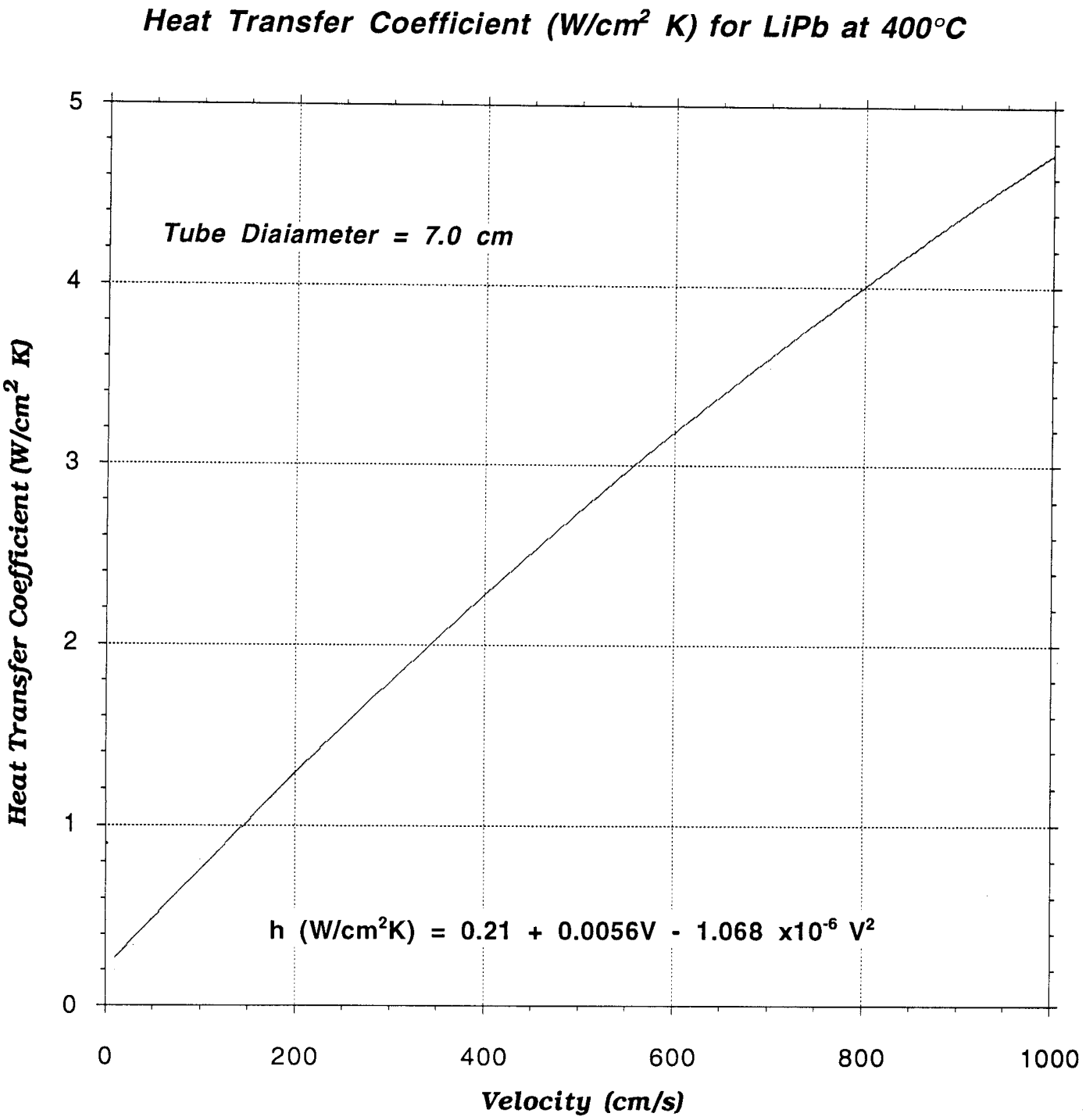

Figure 5.18. A graph of the heat transfer coefficient used for liquid metal (PbLi).

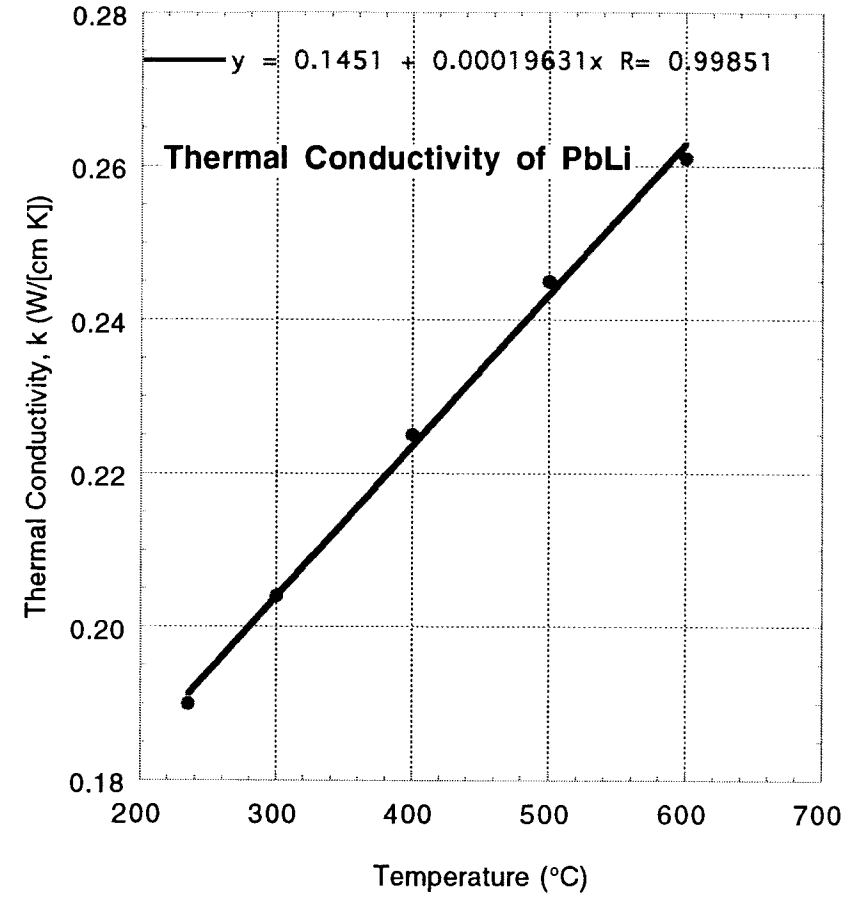

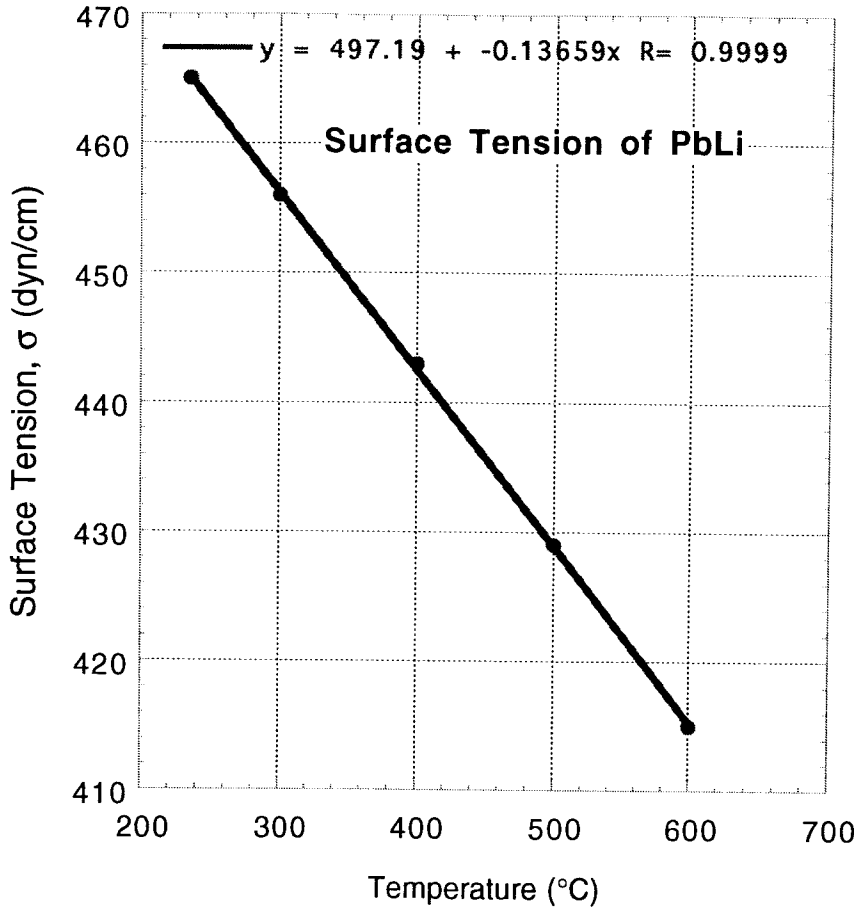

Figure 5.19. A graph of the material data base used for liquid metal (PbLi), thermal conductivity and surface tension.

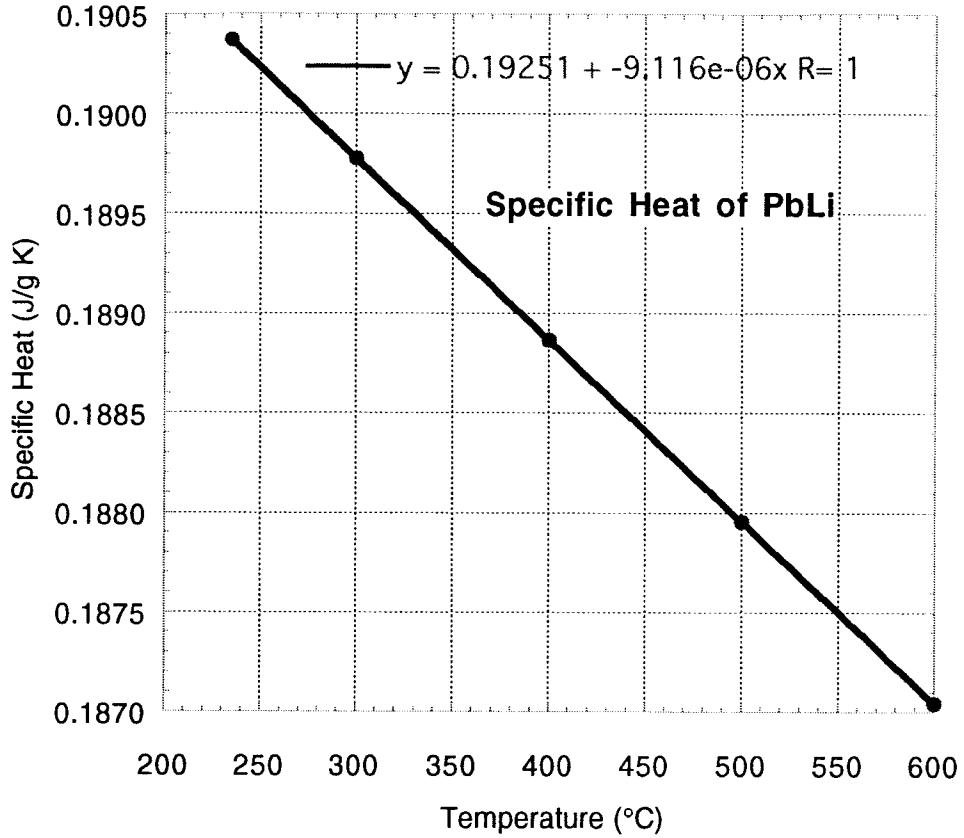

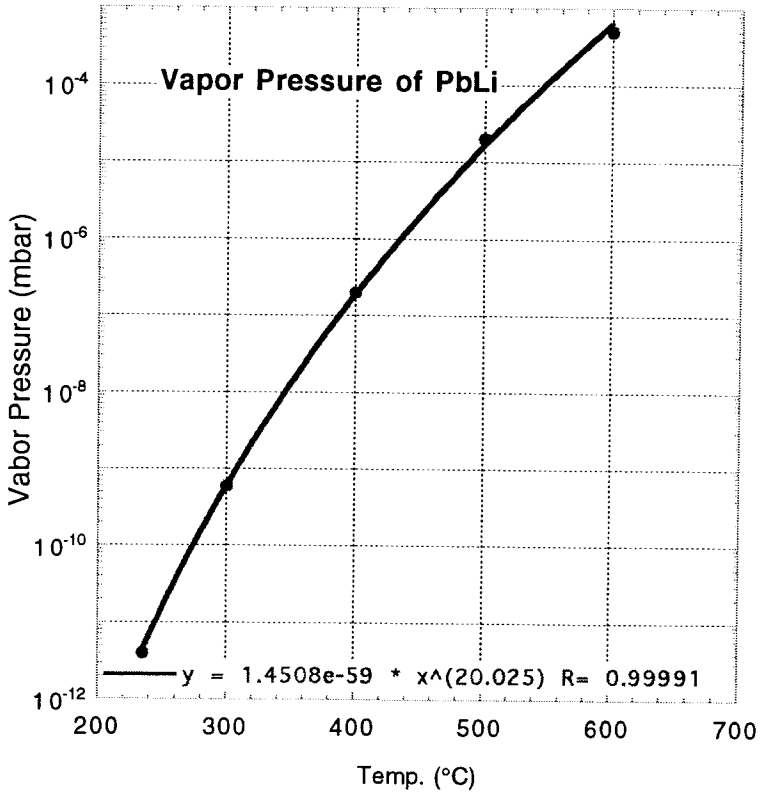

Figure 5.20. A graph of the material data base used for liquid metal (PbLi), specific heat and vapor pressure.

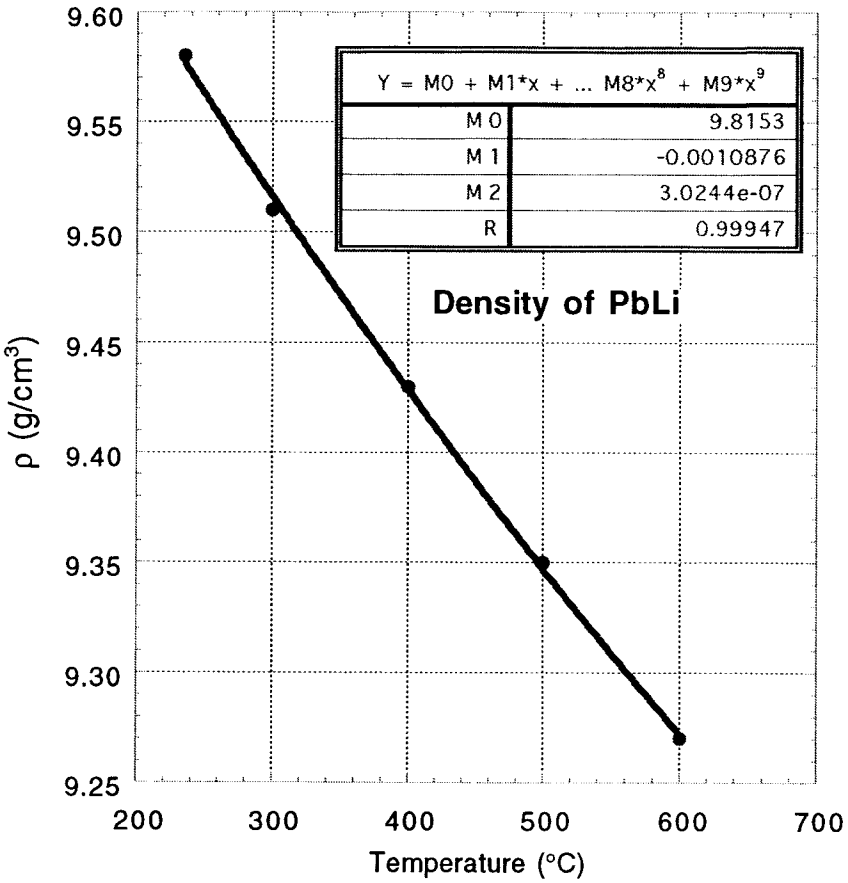

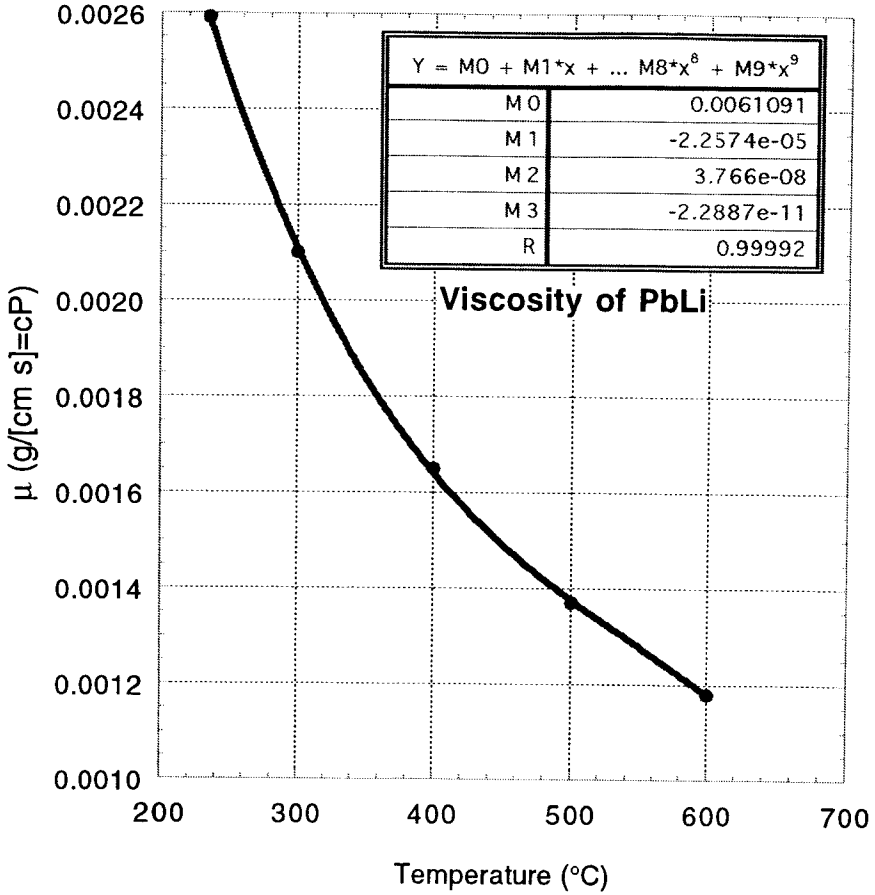

Figure 5.21. A graph of the material data base used for liquid metal (PbLi), density and viscosity.

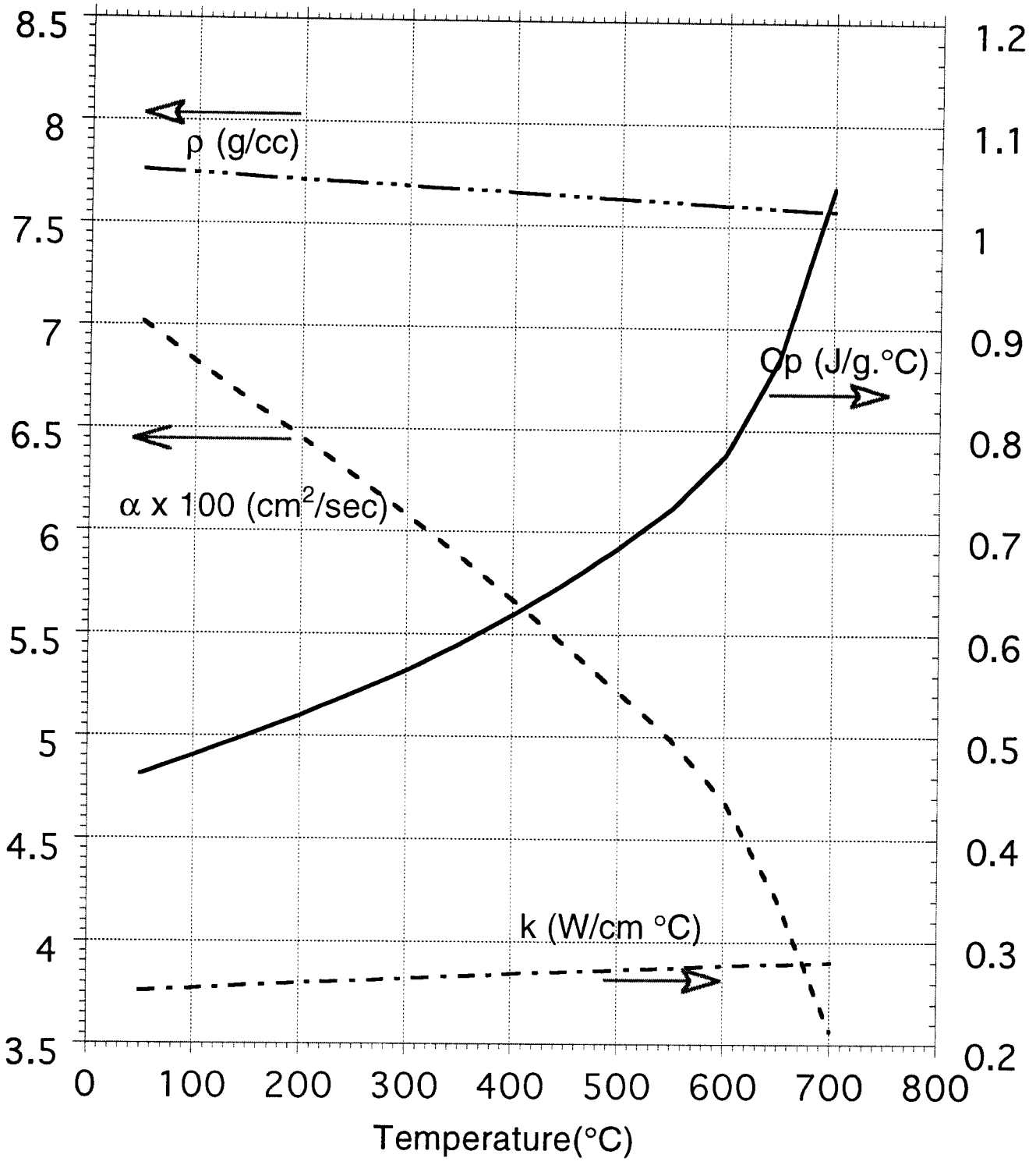

Figure 5.22. A graph of the material data base used for structural material (HT-9), specific heat, density, thermal conductivity an thermal diffusivity.

References for Section 5

1. G. L. Kulcinski, et al., "The INPORT Concept – An Improved Method to Protect ICF Reactor First Wall," J. Nucl. Matls., 102 & 104, 103-108 (1981).

2. B. Badger et al., "LIBRA – A Light Ion Beam Fusion Conceptual Reactor Design," University of Wisconsin Fusion Technology Institute Report, UWFDM-800, Feb. 1990.

3. B. Badger et al., "LIBRA-LiTE – A Commercial Light Ion Fusion Power Plant," FPA-91-4 and University of Wisconsin Fusion Technology Institute Report, UWFDM-880, Dec. 1991.

4. G. I. Taylor, "Formation of Thin Flat Sheets of Water," The Scientific Papers of Sir Geoffrey Ingram Taylor, Edited by G. K. Batchelor, Trinity College, Cambridge, UK, Vol. IV, Paper #33, pp. 378-396, 1971.

5. N. Dombrowski, D. Hasson and D. E. Ward, "Some Aspects of Liquid Flow Through Fan Spray Nozzles," Chemical Engineering Science, Pergamon Press Ltd., London, Vol. 12, pp. 35-50, 1960.

6. R. D. Blevins, *Formulas for Natural Frequency and Mode Shape*, Robert E. Krieger Publishing Co., Malabar, FL, 1987, p. 108.

7. F. B. Hildebrand, *Advanced Calculus for Applications*, Prentice-Hall, Englewood Cliffs, NY, 1976, p. 484.

8. Nuclear Systems Materials Handbook, Vol. 1, Design Data (March 1984).

9. R. O'Dell et al., "User's Manual for ONEDANT: A Code Package for One-Dimensional, Diffusion-Accelerated, Neutral Particle Transport," Los Alamos National Laboratory, LA-9184-M, 1989.

10. P. F. Rose, "ENDF/B-VI, The U.S. Evaluated Nuclear Data Library for Neutron Reaction Data," Summary Documentation Report ENDF 201, U.S. National Nuclear Data Center, 1992.

6. Beam Ports and Diode Damage Assessment

6.1. Diode Enclosure Environment

The diodes' atmosphere must be physically separated from that of the reactor chamber, since they require a much higher vacuum to operate properly. The pressure in the chamber just prior to a shot is 0.2 torr at 300 K or 0.52 torr at the maximum LiPb temperature of 773 K. However, the pressure in the diodes' enclosure must not exceed 10^{-4} torr, more than three orders of magnitude lower. The beam port aperture for the self-pinched propagation must be ~ 2 cm in diameter. Such a large hole connecting the huge volume of the reactor chamber to the very small volume of the diodes makes it impossible to maintain a pressure of 10^{-4} torr by using steady state differential pumping. It has always been assumed that some sort of shutter system will be used to isolate the diodes from the reaction chamber. Several schemes have been envisioned, such as counter rotating double discs as well as single discs. In these schemes, holes in the rotating discs overlap with the beam aperture in the chamber at the moment the beam is fired, thus ingesting the chamber atmosphere only when the aperture is open. There are some steady state leaks taking place through the clearances around the discs, but they are small and can be pumped out by the vacuum system in each of the diode enclosures.

6.1.1. Double Rotating Discs

In this scheme, two discs with holes at the same radius are mounted on concentric uniaxial shafts and rotate at different speeds either in the same direction or in opposing directions. The slow disc rotates at the rep-rate of the reactor, while the fast disc rotates at a much higher rotational speed. The holes in the two discs overlap at many points depending on the rotation of the high speed disc and one of these points overlaps with the beam aperture. Thus the beam aperture is open onto the chamber only for the duration it takes for the high speed disc to sweep across it. All the other times when the high speed disc overlaps with the beam aperture, it is obscured by the slow disc. Although this scheme is very effective for limiting the time the diode enclosure is in communication with the chamber,

it is complicated and would be prone to failure in the severe environment of a fusion reactor. Further, we have found that a single disc rotating at a slow rate can perform the function of isolating the two environments and be much more reliable.

6.1.2. Single Rotating Discs

The scheme adopted for LIBRA-SP has a single rotating disc with a radius of 25 cm and a 2 cm diameter hole located at a radius of 20 cm. The disc rotates at a frequency equal to the rep-rate of the reactor and the time the beam aperture is open is determined by rotation frequency and the radius at which the hole is located from the shaft. Using the disc parameters and a rep-rate of 3.9 Hz, the time it takes for the hole in the disc to sweep across the beam aperture is 8.2 ms and the beam aperture is fully open at 4.1 ms.

The beam, after passing through the beam aperture, travels down a tube 150 cm long, which puts it beyond the limit of the blanket composed of PERIT tubes, and then travels through open space to the target at the reactor center. This tube plays a major role in the dynamics of the chamber gas. Its conductance limits the access of gas from the chamber thus minimizing the total amount ingested during the time the beam port is open.

6.1.3. Modeling the Problem

Figure 6.1 is a schematic of the system, showing the diode enclosure connected to the beam tube through the beam aperture. The rotating disk is shown with the hole 180° from the beam aperture. It is entirely enclosed in the space between the diode and the beam tube which is sealed to the diode enclosure. This means that gases which fill the disc enclosure can only come through the beam tube.

Figure 6.2 is a plot of the overlapped aperture area and the cumulative area time product as a function of time. This cumulative area-time product curve will be used in computing the effective conductance of the beam aperture. The conductance of the system is the sum of the inverse of each individual conductance if they are located in series. This will be done for the first 4.1 ms of the beam aperture opening when the pressure in the reaction chamber is low, and for the second 4.1 ms, after the pulse, when the chamber pressure is high.

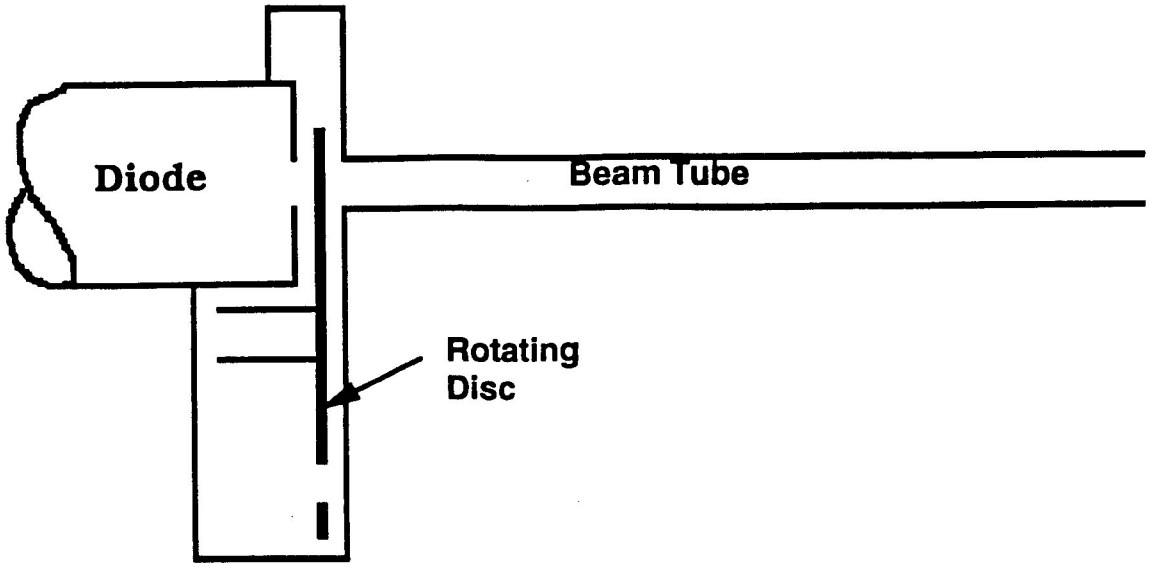

Figure 6.1. Schematic of diode/chamber interface.

The total throughput is the sum of the gas leakage over the 8.2 ms. This throughput raises the pressure in the diode enclosure and must be evacuated back to 10^{-4} torr in $\sim$ 250 ms before the next pulse arrives.

6.1.4. System Conductances

The conductance of a cylindrical tube in the viscous flow regime is expressed as [1]:

$$C = \frac{r^4(\overline{p})}{1.91\eta L} \qquad \ell/\mathrm{s}$$

where r is the tube radius in cm, $\overline{p}$ is the average pressure in torr, η is the gas viscosity in poises (g/cm·s) and L is the tube length in cm.

The pressure in the reaction chamber prior to the pulse is 0.52 torr (consistent with an atom density of $7 \times 10^{15}/\mathrm{cm}^3$ at $T = 770$ K), the pressure in the diode enclosure is 10^{-4} torr, which gives the average pressure $\overline{p}$ of 0.26 torr. Viscosity of He gas at 770 K is 3.94×10^{-4} poise and is independent of pressure, and the tube length L is 150 cm. The beam tube conductance is:

$$C_{bt} = \frac{(1)^4(0.26)}{(1.91)(3.9 \times 10^{-4})(150)} = 2.3\,\ell/\mathrm{s}\,.$$

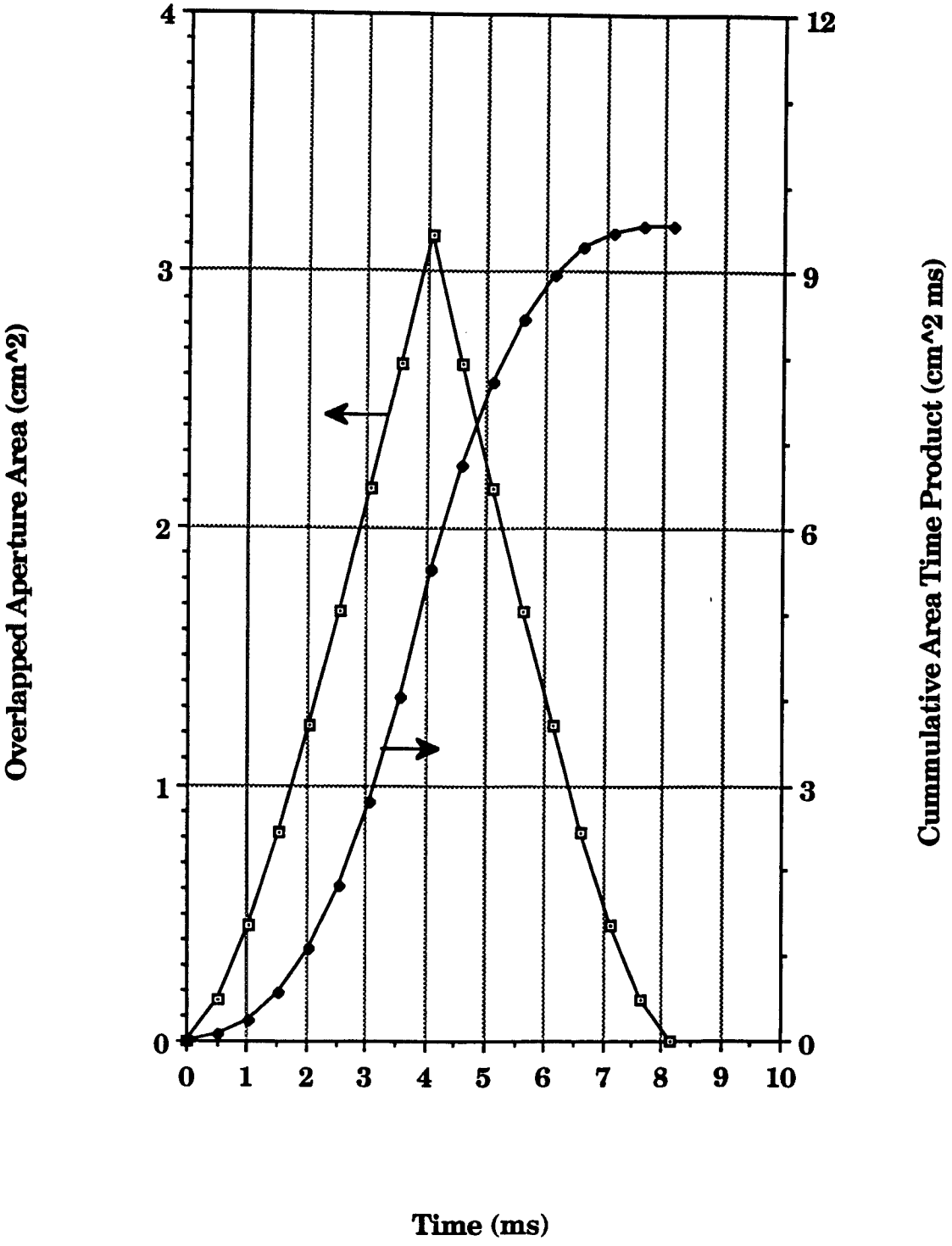

Figure 6.2. Overlapped aperture area and cumulative area-time product as functions of time.

The beam aperture changes with time as the hole in the disc overlaps with it. To calculate an equivalent constant aperture we make use of the area-time product curve in Fig. 6.2. At 4.1 ms the cumulative area-time product is 5.5 cm^2ms which is an equivalent area of 1.34 cm^2 or an aperture radius of 0.65 cm. The conductance of an aperture in the viscous flow regime is [1]:

$$C = \frac{1.142 \times 10^{-2} r^2}{\eta(1 - p_1/p_0)} \qquad \ell/\mathrm{s}$$

where p_0 is the source pressure and p_1 the sink pressure in torr. The conductance of the aperture is then:

$$C_a = \frac{1.142 \times 10^{-2}(0.65)^2}{3.9 \times 10^{-4}(1 - 10^{-4}/0.52)} = 12.25\ \ell/\mathrm{s}\,.$$

The conductance of the system consisting of the tube and aperture, which are in series is:

$$\frac{1}{C_s} = \frac{1}{C_{bt}} + \frac{1}{C_a}$$

and

$$C_s = \frac{C_{bt} C_a}{C_{bt} + C_a} = \frac{(2.3)(12.25)}{2.3 + 12.25} = 1.94\ \ell/\mathrm{s}\,.$$

The same procedure is followed for determining the conductances after the pulse, the remaining 4.1 ms when the pressure and temperature in the chamber rise, and the He gas viscosity also rises as a result of the higher temperature.

The target yield is 589 MJ, of which 34%, or 200 MJ, is in x-ray and ion debris, which when deposited in the gas raises the pressure in the chamber to 260 torr. Although this pressure does not last the full 4.1 ms, we will use it to make the calculation conservative. Under these conditions the equivalent conductance of the system is 6.93 ℓ/s.

6.1.5. Required Pumping Speed

Using the conductances determined above we can now calculate the throughput which is ingested into the diode enclosure during the 8.2 ms. In the first 4.1 ms, the throughput is:

$$(1.94\ \ell/\mathrm{s})(0.52\ \mathrm{torr}) = 1.0\ \mathrm{torr}\ \ell/\mathrm{s}$$

and the total quantity is

$$\frac{1.0 \text{ torr } \ell}{\text{s}} \left(\frac{4.1}{1000}\right) \text{ s} = 4.1 \times 10^{-3} \text{ torr } \ell \,.$$

In the second 4.1 ms the throughput is:

$$(6.93 \ \ell/\text{s})(260 \text{ torr}) = 1802 \text{ torr } \ell/\text{s}$$

and the total quantity is 7.39 torr ℓ. It is estimated that the volume of the diode enclosure is $1.7{\times}10^5$ cm^3 or 170 liters. The pressure rise in the diode enclosure is $\frac{7.39 \text{ torr } \ell}{170 \ \ell}$ or $4.3{\times}10^{-2}$ torr.

The vacuum pump capacity must reduce the pressure from 4.3×10^{-2} torr to $1{\times}10^{-4}$ torr in <256 ms. The capacity will be based on 230 ms. The equation for determining pumping speed is:

$$S = \frac{V}{t} \ln p_1/p_2$$

where S is pump speed in ℓ/s, V the enclosure volume in liters, t is time in seconds, p_1 is initial pressure and p_2 is final pressure. The pump speed is:

$$S = \frac{170}{0.23} \ln \frac{4.3 \times 10^{-2}}{1 \times 10^{-4}} = 4482 \ \ell/\text{s} \,.$$

Each diode will need a pump of such capacity close coupled to it, to maximize the conductance in the coupling joint. Pumps of such capacity are readily available, utilizing turbomolecular units backed up by roots blowers. Table 6.1 gives the parameters of the diode evacuation system.

6.2. Neutronics Analysis

Radiation damage to the sensitive components of the diodes is affected by the detailed geometrical configuration and neutron streaming through the ports. A multi-dimensional neutronics calculation is required to properly model the complicated geometrical configuration. However, at this time, the detailed reference diode design is not well defined. A schematic of a preliminary diode design is shown in Fig. 6.3. Hence, preliminary one-dimensional neutronics calculations have been performed to estimate the expected damage levels in the diode components.

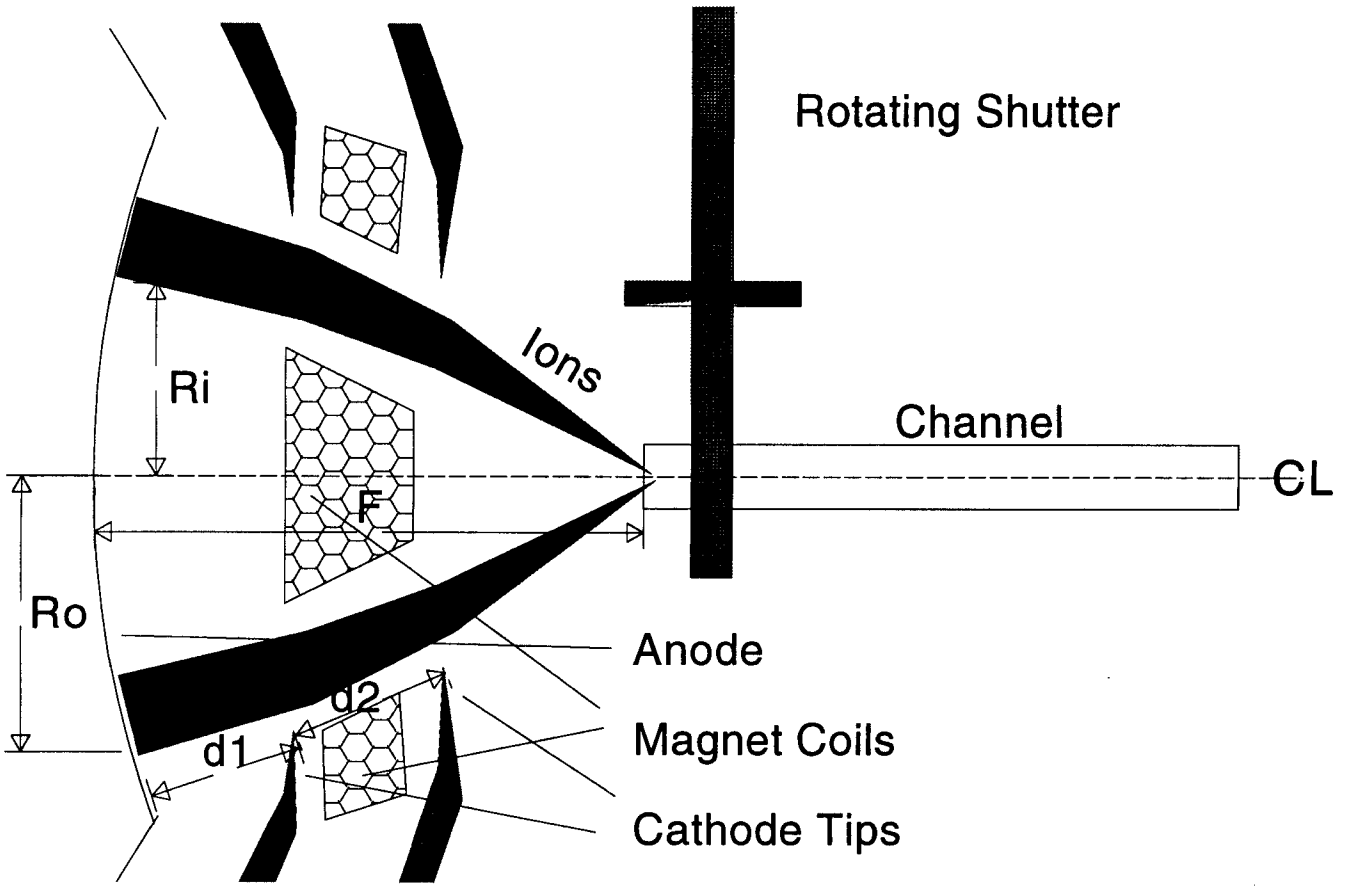

Figure 6.3. A schematic of the preliminary diode design.

Table 6.1. Diode Vacuum System Parameters

Initial He atom density in chamber (#/cm^3)	7×10^{15}
Initial chamber pressure in chamber (torr)	0.52
Pressure in chamber after a pulse (torr)	260
Volume of reaction chamber (m^3)	2325
Pressure required in diode enclosure (torr)	10^{-4}
Volume of diode enclosure (m^3)	0.17
Diode beam aperture diameter (cm)	2.0
Diameter of beam tube (cm)	2.0
Length of beam tube (cm)	150
Rotating disc diameter (m)	0.5
Hole in the disc is at a radius of (m)	0.2
Rep-rate of reactor (Hz)	3.9
Rep-rate of disc (Hz)	3.9
Pressure rise in diode enclosure (torr)	4.3×10^{-2}
Pump capacity for each diode (ℓ/s)	4500

Several conservative assumptions are made to give an upper bound conservative estimate. The calculations have been performed in spherical geometry representative of the blanket and reflector dimensions at the reactor midplane. Because of the cylindrical configuration of the chamber, more shielding will be provided for the diodes which are placed at angles above and below the reactor midplane. In addition, the model used in the one-dimensional calculation assumes that the diode is located right at the back of the reflector at a distance of 5.7 m from the target. The radiation damage will be lower if the diodes are located farther from the target. The results presented here are normalized to the DT fusion power of 2285 MW.

The diode components most sensitive to radiation damage are the diode casing and the magnets. The diode casing is assumed to be made of the ferritic steel alloy HT-9. In this study, we adopted a conservative end-of-life dpa limit of 150 dpa for HT-9. In the normal magnet, we are concerned with both electrical and mechanical degradation of the ceramic insulation and the electrical resistivity of the copper conductor, resulting primarily from neutron-induced transmutations. An additional irradiation problem is radiolytic decomposition of the water coolant, leading to corrosion and erosion product formation.

Among the most important mechanisms mentioned above, only one was found during the MARS [2] study as lifetime limiting for the normal magnet, namely the neutron-induced swelling in the ceramic insulator. Among the common ceramic insulators that are used in the normal magnets, spinel ($MgO{\cdot}Al_2O_3$) is of particular interest in the high-neutron-irradiation environment because of the superior absence of swelling in this insulator. Assuming that a 3 vol.% neutron induced swelling in polycrystalline spinel can be accommodated in the normal magnet structure without causing stress problems, the neutron-fluence limit for the use of solid-polycrystalline spinel is 4×10^{22} n/cm^2 (E $>$ 0.1 MeV) in the temperature range 100 to 300°C.

The peak dpa and helium production rates in the HT-9 diode casing located behind the chamber at a distance of 5.7 m from the target are 0.06 dpa/FPY and 0.0006 He appm/FPY, respectively. The end-of-life dpa in the diode casing is, therefore, only 1.8 dpa for 30 FPY. This is a factor of 83 lower than the design limit. This implies no diode replacement is needed based on damage to the casing. However, this represents a lower bound estimate for casing damage since no contribution from streaming neutrons is included. Although the casing is entirely behind the chamber and no part of it will be exposed to the direct source neutrons from the target, neutrons streaming into the diode through the port will interact with the magnets and other diode components resulting in a backscattered secondary neutron component that enhances damage in the casing. A very conservative estimate for casing damage can be obtained by performing the calculation without any material between the target and the diode casing at 5.7 m radius. This results in a dpa rate of 30 dpa/FPY

implying 5 FPY diode casing lifetime. Again this is a very conservative damage estimate since the diode casing is completely out of the direct line-of-sight of source neutrons and the actual dpa rate in the casing should only be slightly larger than the 0.06 dpa/FPY with the full shield in place and it is expected that damage to the diode casing will not limit the diode lifetime. This needs to be confirmed by detailed multi-dimensional calculations.

It is clear from Fig. 6.3 that some magnets will be in the direct line-of-sight of source neutrons. For this reason, two calculations were performed to determine the fast neutron fluence per FPY at the magnet in both cases with and without the blanket and reflector placed between the target and the magnet. In these calculations, the conservative assumption that the magnet is located at 5.7 m from the target was also made. The fast neutron fluence per FPY at the magnet behind the chamber is 1.67×10^{20} n/cm^2 and the end-of-life fluence will be 5×10^{21} n/cm^2 after 30 FPY. This is a factor of 8 lower than the design limit for the spinel insulator. On the other hand, the fast neutron fluence per FPY at the magnet in the direct line-of-sight of source neutrons is 6.4×10^{21} n/cm^2 implying a 6.25 FPY lifetime. Again, this is a very conservative estimate particularly for magnets located away from the direct line-of-sight of source neutrons which are expected to last for the whole reactor lifetime. However, several replacements might be needed for magnets located along the direct line-of-sight of source neutrons. These results need to be confirmed by performing a detailed multi-dimensional neutronics calculation once the reference diode design gets well defined.

References for Section 6

1. H. A. Steinberg, "Handbook of High Vacuum Engineering," Reinhold Publishing Corp., 1963.

2. B. G. Logan et al., "MARS Mirror Advanced Reactor Study Commercial Fusion Electric Plant," Lawrence Livermore National Laboratory, UCRL-53480 (1984).

7. Tritium and Safety Analysis

7.1. Tritium Issues

The principal tritium systems considered are related to the fueling and breeding functions. These systems consist of many components, each designed for a specific processing function. The functions of these sub-components are briefly described and their tritium inventories are estimated. Such information is required in order to evaluate the potential radiological hazard to plant personnel and the local environment due to routine and off-normal release of tritium.

7.1.1. Target Fuel Preparation

The targets will be filled with liquid DT, as described in the LIBRA [1] study, and stored in a target fabrication facility adjacent to the reactor building. Each capsule contains 5.77 mg (DT) and 337,000 targets per day are required; however, only one-hour batches will be prepared at a time so that only $\sim$ 49 g(T) is being processed. In addition, two batches of filled targets are stored in a cryogenic freezer at $\sim$ 19 K so that a uniformly thick coating of solid DT can form on the inside of the capsule. The total vulnerable tritium which could be released in a severe accident is $\sim$ 146 g(T), as noted in Table 7.1.

The daily amount of tritium processed in this facility is $\sim$ 1200 g. Experience at TSTA [2] has indicated that with proper design of gloveboxes surrounding all processing equipment, the tritium release to the stack would be only $\sim$ 12 Ci/day. A one-day's supply of purified T_2 may be stored but not processed in a vault so that the off-gas would be small ($\sim$ 2 Ci/d) and no release from an accident would occur.

7.1.2. Reactor Building Tritium Inventory

A one-hour supply of targets (49 g(T)) is kept in the target injector facility above the reactor. All of this tritium could be released in a major reactor accident; however, the routine release from the frozen fuel would be low, $\sim$ 4 Ci/d.

Table 7.1. Tritium Inventory and LIBRA-SP Release Summary

Location	System	Inventory	Tritium Routine Release	Tritium Accidental Release
Target factory	–	g	Ci/d	g(T)
	In process	146	12	146
	Storage	1200	2	0
Reactor building	Targets	49	4	49
	Breeder alloy			
	Primary	31.5	15	10
	Secondary	1.0	1	1
Fuel reprocessing	Equipment	107	13	107
	Cryo-still	14	12	0
Storage	Vault	2000	2	0
Steam generator	Water	0	50	0
	Coolant	Routine release Air 61 Ci/d Water 50 Ci/d		312

The LiPb coolant-breeder contains tritium which must be separated and recycled, as is described later. The steady-state tritium inventory in this molten alloy is $\sim$ 3 g. Because all of this hot liquid is multiply contained, the routine tritium release to the environment is small, $\sim$ 16 Ci/d. A major rupture in this piping would cause some of the hot liquid to come in contact with air or water. This alloy was selected, however, because it does not react vigorously with the atmosphere or water and a solidified surface coating would prevent reactions which would release all of the dissolved tritium. Consequently only $\sim$ 1/3 of the tritium ($\sim$ 10 g) would be released.

The fuel reprocessing equipment receives DT gas separated from the liquid breeder at the exit from the reactor cavity and the helium gas (a product of the fusion reaction) evacuated from the reactor cavity. These gases are chemically purified through a series of

adsorbers and filters. Such equipment contains $\sim$ 2 hr of inventory, $\sim$ 107 g(T). Finally, the fuel gases are liquified and introduced into a cryogenic distillation column where pure DT is recovered from the He and excess D_2 (added as a carrier in the breeder separation chamber). Special techniques [3] have been developed so that the liquid in the cryo-still would contain only $\sim$ 14 g(T). The routine release from the enclosure surrounding the reprocessing equipment should release only 25 Ci/d. In the event of a severe accident rupturing the fuel reprocessing system all the tritium could be released, 107 g(T). The cryo-still, however, is installed in a sealed refrigerated box which contains an evacuated chamber sufficiently large so that all the DT gas, if released, can be captured. Consequently, none of this gas should escape to the environment.

7.1.3. Tritium Breeding and Recovery from the Liquid $Li_{17}Pb_{83}$ Alloy

The DT fuel in each target is ignited by the implosion of the ablating capsule; however, only a limited quantity of DT ($\sim$ 30%) undergoes nuclear fusion so that the unburned fuel and the tritium produced by nuclear reactions of the LiPb in the PERIT tubes must be recovered and reprocessed to sustain the fuel cycle. All of these materials together with the target debris are swept to the bottom of the reactor cavity into a pool of the liquid alloy. The target debris may not be soluble in this liquid and will have to be removed by filtration. The helium produced by the fusion reactions will not be soluble and must be evacuated by mechanical pumps. The hydrogen isotopes, D+T, have limited solubility in the alloy with a solubility constant [4] at 500°C (773 K) of 1.2×10^{-7} at.frac. (D+T)/$Pa^{1/2}$.

The injection rate of D+T into the reactor cavity is 14.9 mg(T)/s (4.98×10^{-3} g.at. (T)/s) and 6.32 mg(D)/s (3.16×10^{-3} g.at. (D)/s). The recovery system utilized must remove the D and T at the same rate and reduce the tritium concentration (pressure) sufficiently so that tritium permeation to the steam generator is acceptable. The recovery system chosen was vacuum degassing of small liquid droplets in an evacauated chamber, similar to the technique utilized for the removal of T_2 from liquid Flibe [5,6]. Such a system must consider the vapor pressure of the alloy, Fig. 7.1, which indicates that the vapor pressure of Pb (in

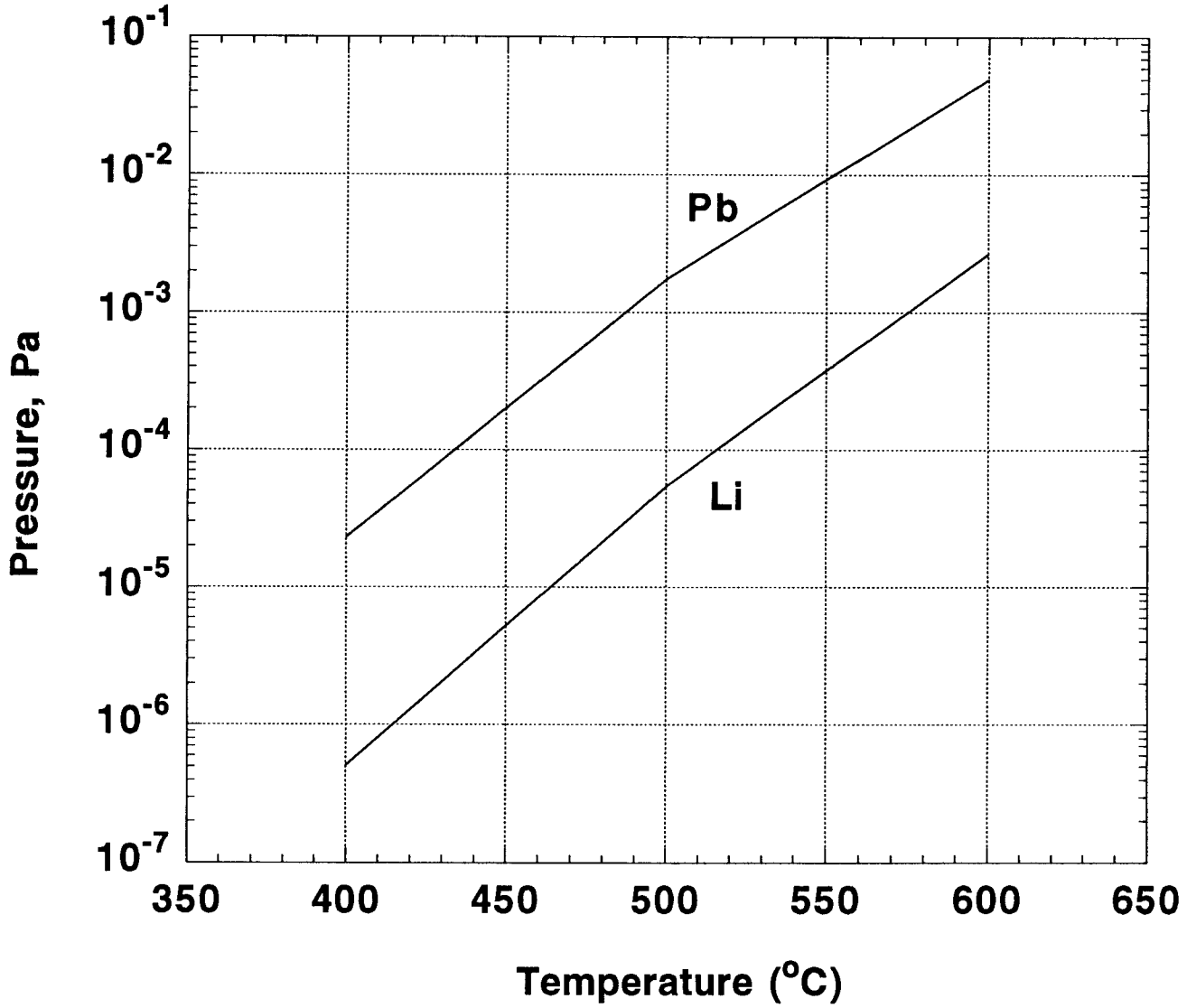

Figure 7.1. Vapor pressure [7] of Pb and Li above the liquid $Li_{17}Pb_{83}$ over the useful temperature range of the alloy contained in ferritic steel.

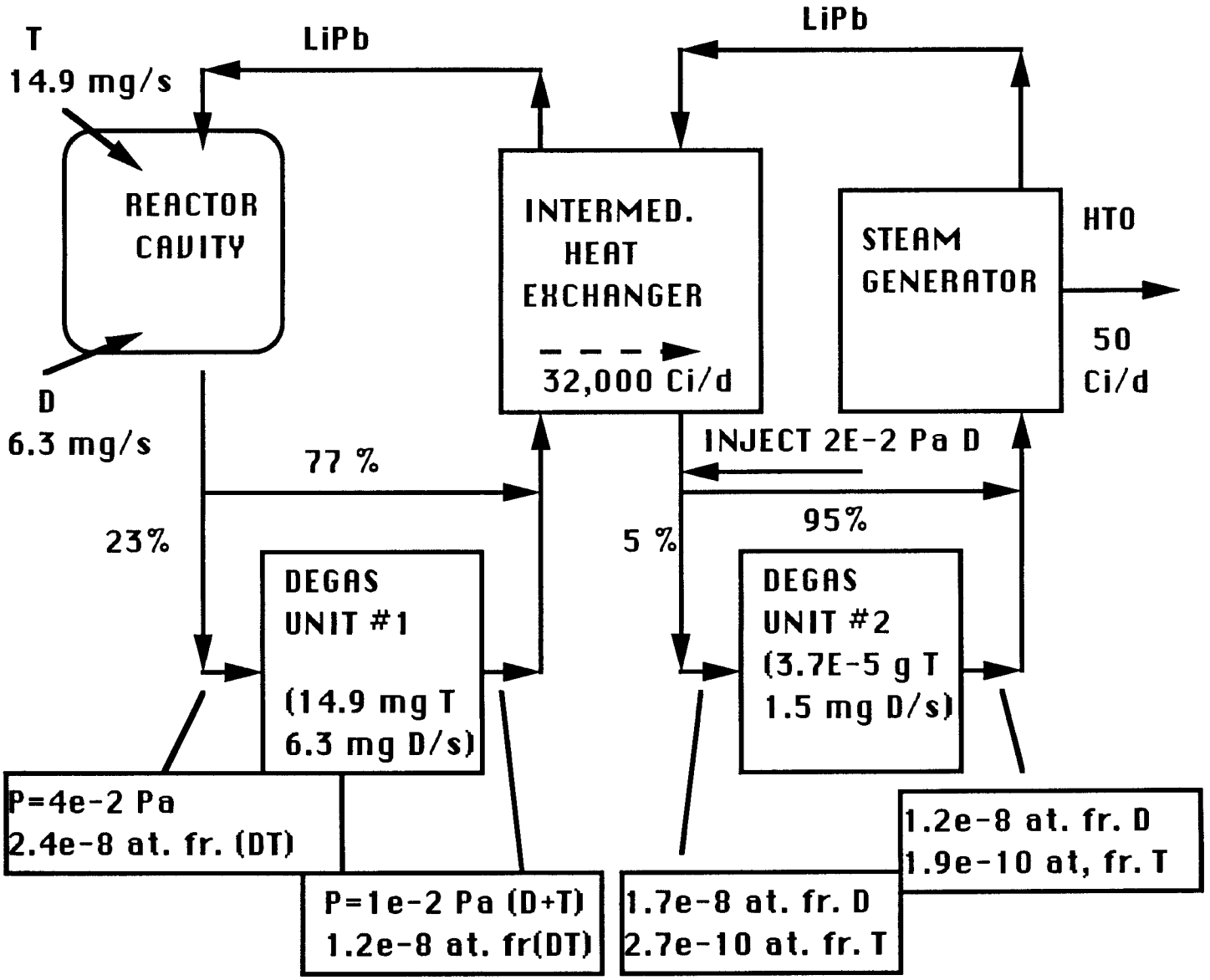

Figure 7.2. Schematic flow diagram for the removal of tritium from the LiPb circuits.

liquid LiPb) is 1.3×10^{-3} Pa at 500°C, the alloy temperature at the exit from the reactor cavity; consequently the lowest pressure in the degassing chamber was limited to 10^{-2} Pa. The lowest concentration of D+T in the alloy would be limited, therefore, to 1.2×10^{-8} at.frac. (D+T). The previously given rate of D+T addition to the reactor cavity would be absorbed in the alloy flowing at the rate of 5×10^5 kg/s (2.9×10^6 moles LiPb/s) to yield a concentration of 2.8×10^{-9} at.frac. (D+T) per pass. At startup approximately 8 cycles through the reactor will bring the gas concentration up to 2.4×10^{-8} at.frac. (D+T) and 23% of the flowing alloy will be diverted to the Degassing Unit #1, as shown in Fig. 7.2, where the rate of D+T removal will equal its input rate. This degassing step is not sufficient to meet acceptable radiological objectives because 32.000 Ci/d of HTO would be lost through the steam generator to the environment. Even at the vacuum limit of 10^{-2} Pa of T_2 the permeation of tritium would still be 160 times too large.

In order to reduce the tritium permeation through the steam generator a secondary loop also containing the LiPb alloy was utilized. Deuterium gas at a pressure of 2×10^{-2} Pa is introduced into this secondary loop so that the T can be removed by isotopic dilution. In Degassing Unit #2 the D_2 pressure is reduced from 2×10^{-2} Pa to 1×10^{-2} Pa and with only 5% of the stream diverted to Unit #2, the tritium concentration is reduced from 2.7×10^{-10} at.frac. to 1.9×10^{-10} at.frac. T, and T and D are removed at the rate of their input. With the concentration of 2.7×10^{-10} at.frac. T in the secondary loop, the permeation of tritium through the steam generator, with a barrier factor of 10 due to an oxide coating on the steam-side, is a reasonable 50 Ci/d to the coolant water.

7.2. Environmental and Safety Assessment

7.2.1. Introduction

A strong emphasis has been given to the environment and safety issues in the LIBRA-SP reactor design. Low activation ferritic steel (modified HT-9) has been used in the blanket and reflector to avoid a high level of induced radioactivity in both regions. Similarly, the use of LiPb as a coolant and breeder eliminates the hazard posed by the energy

producing chemical reactions usually associated with the use of lithium and hence reduces the risk of mobilizing the radioactive inventory present in the reactor. The methodology used in this analysis does not depend on the probability of accident initiating scenarios. We have rather adopted the principle of considering the worst possible accident scenario. To evaluate the possible radiological hazard to the public, we used a two step approach in calculating the possible off-site dose. The first step in our approach is the identification of the sources and locations of the radioactive inventories inside the reactor building. However, since the existence of radioactivity does not in itself represent a safety hazard, the second step in our approach was to consider a set of pessimistic but rather credible accident scenarios for mobilizing and releasing the radioactive inventory.

In this section a detailed activation analysis has been performed in order to calculate all possible radioactive inventories for the current LIBRA-SP design. Results of the radioactivity calculations are used to evaluate the following:

a. The biological dose rate at different locations inside the reactor containment following shutdown to assess the feasibility of hands-on maintenance.

b. The radwaste classification for each region of the reactor.

c. The maximum public dose from routine operational effluents.

d. The off-site doses from accidental release of the radioactive inventories present in the containment building, target factory and fuel reprocessing facility.

7.2.2. Safety Design Goals

The main safety goals pursued for the LIBRA-SP reactor design are:

1. Limiting the need for remote maintenance and allowing for hands-on maintenance by reducing the biological dose rate following shutdown below 25 μSv/hr by increasing the biological shield where it is possible.

2. Disposing the reactor structure and coolant as either Class A or Class C low level wastes as regulated by the Nuclear Regulatory Commission's (NRC) 10CFR61 guidelines.

3. Limiting the public dose to the maximally exposed individual (MEI) from routine operational effluents to less than 5 mrem/yr.

4. Producing the lowest possible whole-body (WB) early dose during a conservative accident scenario. The low off-site dose will allow for the avoidance of early fatalities in case of an accidental release of radioactivity.

5. Eliminating the need for the use of N-Stamp nuclear grade components.

7.2.3. Off-Site Definitions

Off-site dose is used to predict the degree of radiological hazard to the public posed by any routine or accidental release of radioactivity from the reactor. However, the health effects to the various human organs are dependent on both the length and method of exposure. While dose from external exposure (cloudshine and groundshine) is only limited to the length of the exposure, decay of the radionuclides inside the irradiated body (from inhalation and ingestion) leads to a continuous internal exposure. In this chapter we used the following dose definitions:

Prompt Dose at 1 km: The dose delivered to a particular organ at 1 km from the release, from cloudshine during plume passage, 7 days of groundshine and the dose commitment over an organ-dependent critical acute time period from inhalation during plume passage.

WB: Whole body, t_{acute} = 2 days.
BM: Bone marrow, t_{acute} = 7 days.
Lung: Lung, t_{acute} = 1 year.
LLI: Lower large intestine, t_{acute} = 7 days.

WB Early Dose: The whole body early dose, where early dose is the dose from initial exposure; i.e., cloudshine during plume passage, 7 days of groundshine, plus the 50-year dose commitment from radioactivity inhaled during plume passage.

WB Chronic Dose at 1 and 10 km: The whole body dose at 1 and 10 km from the release due to both initial and chronic (50-year) exposures.

Inh + grd:	Chronic exposure considers the 50-year groundshine exposure plus the 50-year dose commitment from inhaled resuspended radioactivity.
Ing:	Chronic exposure considers the ingestion pathway only.
Total:	Chronic exposure considers all three pathways: groundshine, resuspension and ingestion.

Cancers: Total number of cancers in a 50-mile radius from initial and chronic exposure.

Sum Organs:	The number of cancers where the body is treated as a sum of individual organs and calculations are based on organ-specific dose factors and dose responses.
WB:	The number of cancers where the body is treated as a single organ and the whole body dose conversion factors and dose response are used.

Population Dose WB (Man-Rem): Total whole body man-rem due to both initial exposure plus an 80-year chronic exposure to the whole body.

7.2.4. Calculational Procedure

Neutron transport calculations have been performed using the one-dimensional discrete ordinates neutron transport code ONEDANT [8]. The analysis uses a P_3 approximation for the scattering cross sections and S_8 angular quadrature set. The problem has been modeled in spherical geometry with a point source at the center of the chamber. The source emits neutrons and gamma photons with energy spectra determined from target neutronics calculations for a specific light ion fusion target. The neutron flux obtained from the neutron transport calculations has been used in the activation calculations. The calculations have been performed using the computer code DKR-ICF [9]. The DKR-ICF code allows for accurate modeling of the pulsing schedule. The pulse sequence used in the activation calculations is shown in Fig. 7.3. In order to achieve 75% availability, the reactor has been assumed to shut down for a period of 5 days following every 25 days of operation for routine maintenance and for the last 40 days of each calendar year for an annual extended

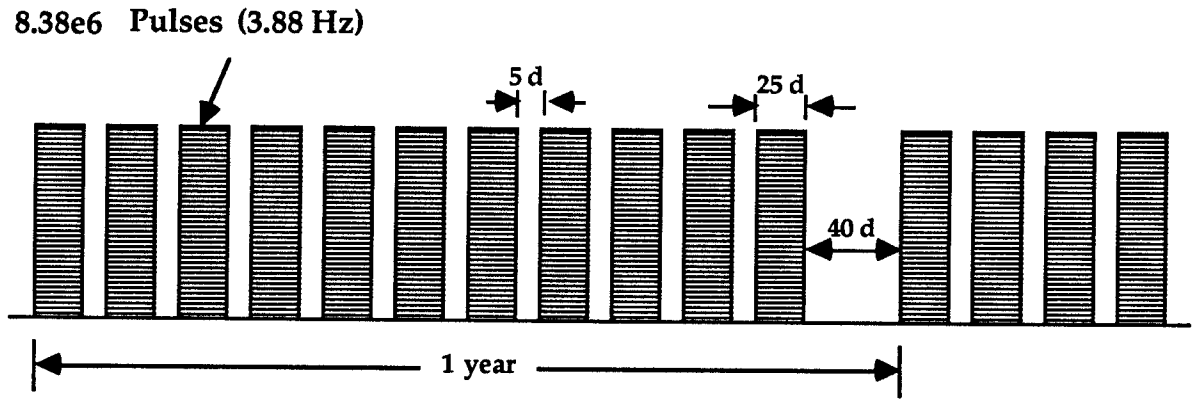

Figure 7.3. Pulse sequence used in activation analysis.

maintenance. The radioactivity generated in the reactor chamber and shield has been calculated for the 40 year reactor lifetime.

The decay gamma source produced by the DKR-ICF code is used with the adjoint neutron flux to calculate the biological dose rate after shutdown using the DOSE [9] code. The dose rate calculations have been performed at different locations inside the reactor containment. The activation results have been also utilized in the radwaste classification and the off-site dose calculations performed by the FUSCRAC3 [10] code. The off-site doses are produced by the accidental release of the radioactive inventory from the reactor containment building assuming the worst case weather conditions. Finally, the EPA code AIRDOS-PC [11] has been used to estimate the off-site dose due to the routine release of tritium.

7.2.5. Activation Analysis

The radioactivity generated in the blanket, reflector, shield and LiPb breeder of LIBRA-SP has been calculated for the 40 year reactor lifetime with 75% availability. The reactor blanket and reflector are made of a low activation ferritic steel (modified HT-9). The chamber is surrounded by a biological shield to allow for hands-on maintenance at selected locations behind it. The steel-reinforced concrete shield is made of 70% concrete, 20% mild steel and 10% helium coolant. In the mean time a separate calculation has been performed

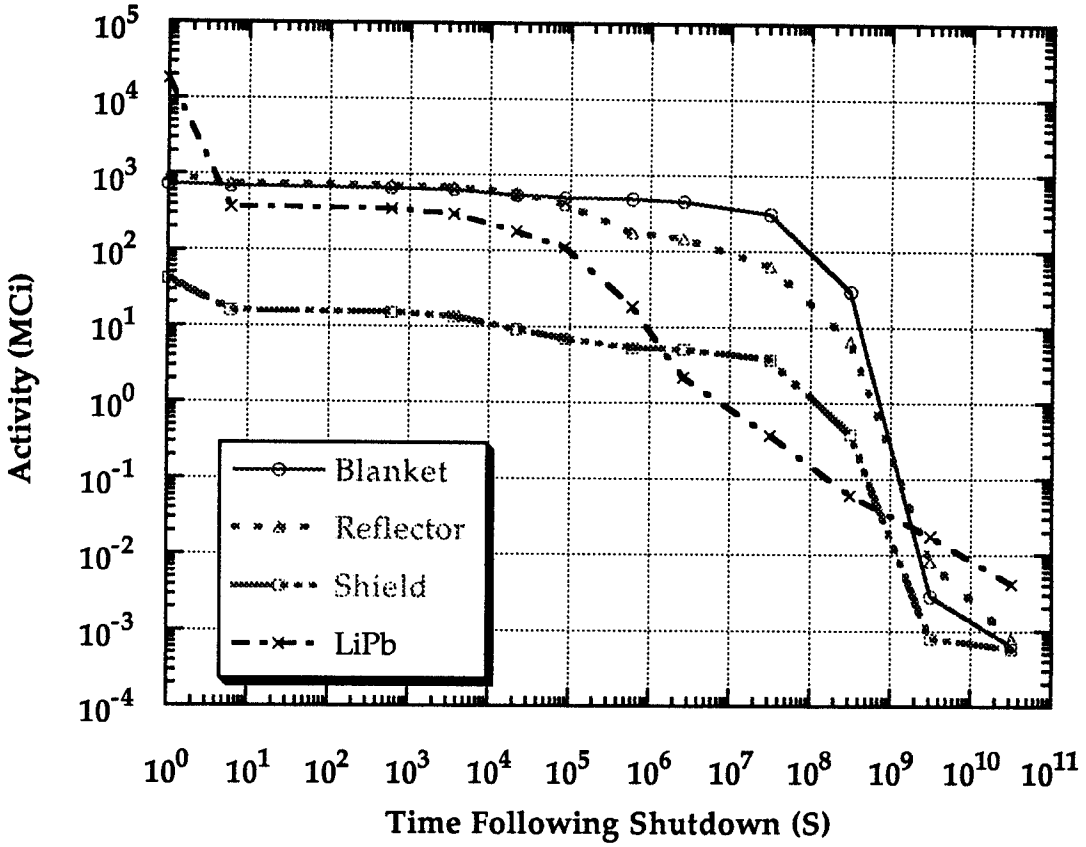

Figure 7.4. Activity following shutdown in different regions of LIBRA-SP.

for the LiPb coolant. The residence time of the LiPb coolant in the chamber is 5 seconds. The total inventory of LiPb takes 15 seconds to go through the reactor chamber. Therefore, the coolant activity has been calculated to allow for the fact that LiPb spends only 33% of the time exposed to neutrons in the reactor chamber. The total activity generated in the different regions of LIBRA-SP as a function of time following shutdown is shown in Fig. 7.4.

The total activity in the blanket at shutdown is 721 MCi and drops to 498 MCi in one day and 307 MCi in one year. The activity induced in the reflector at shutdown is 924 MCi and drops to 407 MCi in one day and 63 MCi after one year. Most of the steel-reinforced concrete shield activity is due to its steel component. At shutdown, the total activity amounts to 41.2 MCi and drops to 6.9 MCi within a day and 3.69 MCi within a year. On the other hand, due to the rapid decay of ^{207m}Pb ($T_{1/2}$ = 0.8 s), the activity

Table 7.2. Dominant Contributors to Radioactivity

Time After Shutdown	Shield	LiPb
< 1 day	^{56}Mn, ^{54}Mn, ^{55}Fe	^{207m}Pb, ^{209}Pb, ^{203}Hg
1day – 1 yr	^{55}Fe, ^{54}Mn, ^{187}W	^{204}Tl, ^{110m}Ag, ^{108m}Ag
1 yr – 10 yr	^{55}Fe, H^3, ^{54}Mn	^{204}Tl, ^{108m}Ag, ^{205}Pb
> 10 yr	^{14}C, ^{63}Ni, ^{53}Mn	^{205}Pb, ^{108m}Ag, ^{208}Bi

Table 7.3. Radioactivity After Shutdown

Time After Shutdown	Activity (MCi)		Decay Heat (MW)		BHP (km^3 air)	
	Blanket	Reflector	Blanket	Reflector	Blanket	Reflector
0	721	924	2.99	3.34	3.7e+8	1.63e+9
1 hour	620	684	2.18	2.88	8.9e+7	8.02e+7
1 day	498	407	0.46	1.09	8.2e+7	5.54e+7
1 week	480	175	0.42	0.18	8.01e+7	3.2e+7
1 month	449	147	0.39	0.14	7.5e+7	2.7e+7
1 year	307	63	0.22	5.63e-2	3.7e+7	9.24e+6
10 years	29	6.5	1.23e-2	1.05e-2	1.05e+6	2.0e+6
100 years	2.78e-3	8.2e-3	1.39e-6	2.72e-6	1.02e+4	4.1e+4

of LiPb drops from 1790 MCi to 370 MCi within a minute from shutdown. The LiPb activity drops to 110 and 0.37 MCi during the first day and first year following shutdown, respectively. Table 7.2 shows the dominant contributors to the activity generated during different time periods following shutdown. Table 7.3 compares the activity, decay heat and biological hazard potential (BHP) in the blanket and reflector regions. The biological hazard potential has been calculated using the maximum permissible concentration limits in air for the different isotopes according to the Nuclear Regulatory Commission (NRC) regulations specified in 10CFR20 [12].

The temporal variation of the decay heat and BHP after shutdown is similar to that of the activity. In general, the decay heat and biological hazard potential are dominated for the most part by the same nuclides shown in Table 7.2. One value which is useful for predicting the thermal response of the structure to a loss of coolant accident is the integrated decay

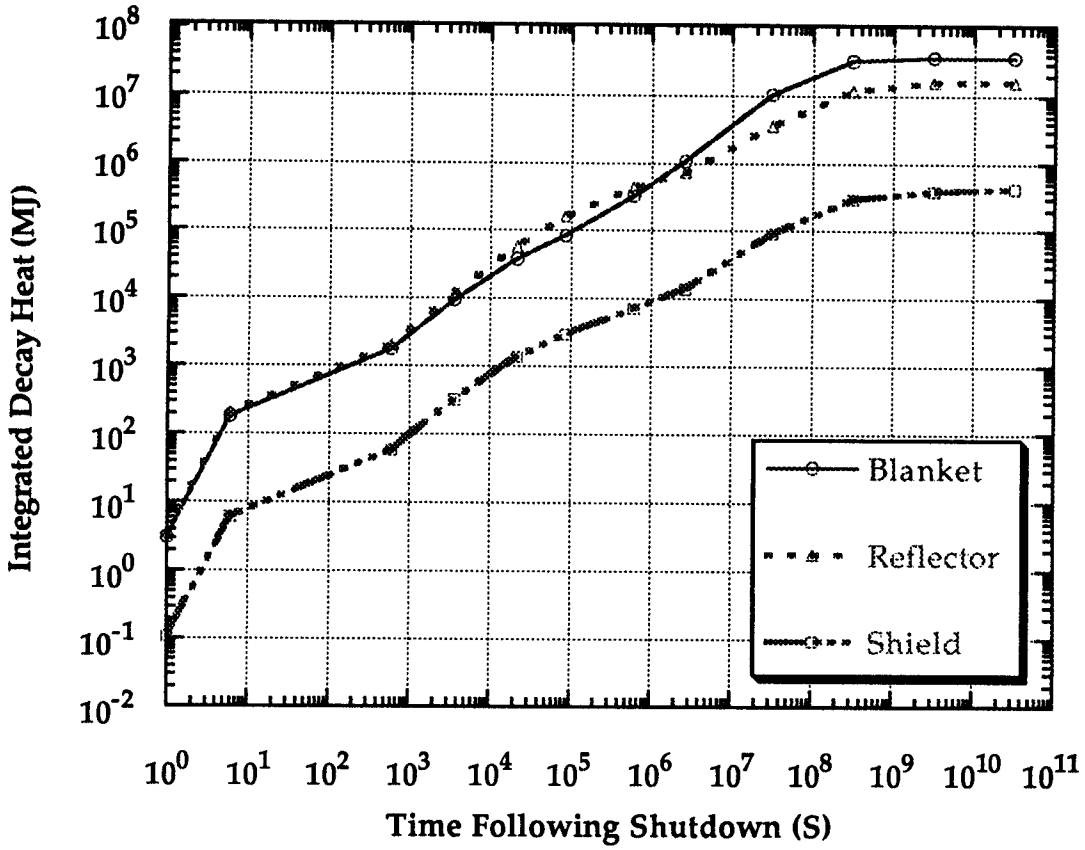

Figure 7.5. Integrated decay heat following shutdown in different regions of LIBRA-SP.

heat. Fig. 7.5 shows the integrated decay heat generated following shutdown in the different regions of LIBRA-SP. The integrated decay heat generated during the first day following shutdown in the blanket and reflector are 78 and 150 GJ, respectively. The integrated decay heat generated in the reactor shield following shutdown is very low. Only 13 GJ of decay heat is generated in the shield during the first month following shutdown.

7.2.6. Maintenance

Biological dose rate calculations have been performed at selected locations to assess the possibility of hands-on maintenance. Fig. 7.6 shows the calculated dose rates as a function of time following shutdown. At all locations, ^{56}Mn ($T_{1/2}$ = 2.6 hr) and ^{54}Mn ($T_{1/2}$ = 313 day) dominate the biological dose rates during the first day. The dose is dominated by ^{54}Mn and ^{55}Fe ($T_{1/2}$ = 2.7 yr) within the first few years.

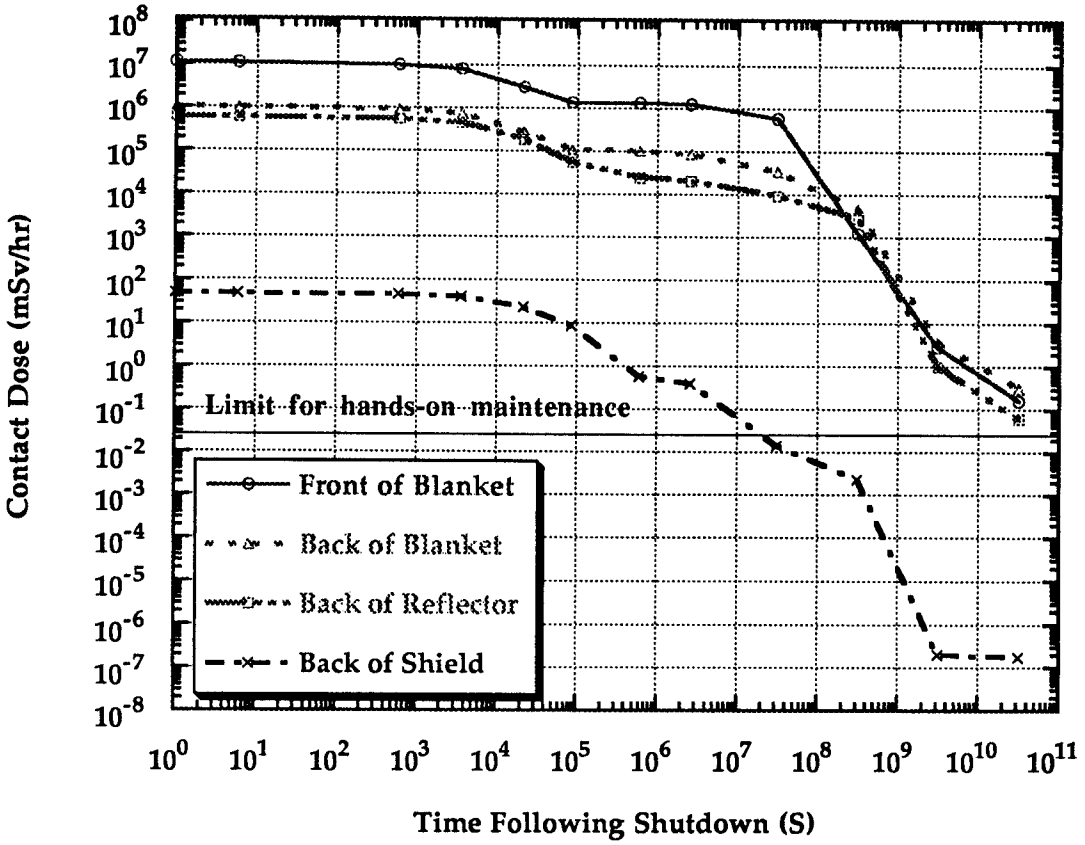

Figure 7.6. Contact dose rates following shutdown.

As shown in the figure, hands-on maintenance is impossible anywhere inside the reactor chamber. The size of the concrete biological shield required for acceptable occupational dose rate during operation has not been determined. In this calculation an 80 cm thick shield was used. As a result only remote maintenance is possible behind the biological shield. Increasing the shield thickness should allow for the possibility of hands-on maintenance. The dose rate behind the biological shield drops to 13.6 μSv/hr after one year following shutdown. A limit of 25 μSv/hr for hands-on maintenance is used in this analysis assuming that the maintenance personnel work for 40 hours a week and 50 weeks a year. Hence, hands-on maintenance will only be allowed behind the current 80 cm concrete shield after 1 year following shutdown.

7.2.7. Radwaste Classification

The waste disposal ratings for LIBRA-SP have been evaluated according to both the NRC 10CFR61 [13] and Fetter [14] waste disposal concentration limits (WDL). The 10CFR61 regulations assume that the waste disposal site will be under administrative control for 100 years. The dose at the site to an inadvertent intruder after the 100 years is limited to less than 500 mrem/year. The waste disposal rating (WDR) is defined as the sum of the ratio of the concentration of a particular isotope to the maximum allowed concentration of that isotope taken over all isotopes and for a particular class. If the calculated WDR ≤ 1 when Class A limits are used, the radwaste should qualify for Class A segregated waste. The major hazard of this class of waste is to individuals who are responsible for handling it. Such waste is not considered to be a hazard following the loss of institutional control of the disposal site. If the WDR is > 1 when Class A WDL are used but ≤ 1 when Class C limits are used, the waste is termed Class C intruder waste. It must be packaged and buried such that it will not pose a hazard to an inadvertent intruder after the 100 year institutional period is over. Class C waste is assumed to be stable for 500 years. Using Class C limits, a WDR > 1 implies that the radwaste does not qualify for shallow land burial. Fetter developed a modified version of the NRC's intruder model to calculate waste disposal limits for a wider range of long-lived radionuclides which are of interest for fusion researchers than the few that currently exist in the current 10CFR61 regulations. Fetter's model included more accurate transfer coefficients and dose conversion factors. However, while the NRC model limits the whole body dose to 500 mrem or the dose to any single organ (one of seven body organs) to 1.5 rem, the Fetter limits are based on the maximum dose to the whole body only.

The specific activities calculated for the different radionuclides have been used to evaluate the radwaste classification of the blanket, reflector, shield and LiPb breeder. Table 7.4 shows the waste disposal ratings (WDR) for each of the reactor regions in the compacted and non-compacted (between brackets) forms. Compacted values correspond to crushing the solid waste before disposal. On the other hand, non-compacted values are based

Table 7.4. Waste Disposal Ratings (WDR) of the Different Regions of LIBRA-SP

WDR	Blanket	Reflector	LiPb	Shield
Class A (10CFR61 limits)	40.5 (1.62) (^{94}Nb, ^{3}H)	8.5 (7.66) (^{94}Nb, ^{60}Co)	0.2 (0.064) (^{63}Ni, ^{60}Co)	(0.125) (^{14}C, ^{94}Nb
Class C (10CFR61 limits)	2.57 (0.103) (^{94}Nb, ^{14}C)	0.68 (0.61) (^{94}Nb, ^{14}C)	9.6e-4 (3.2e-4) (^{63}Ni)	(8.64e-3) (^{14}C, ^{94}Nb
Class C (Fetter limits)	41.5 (1.66) (^{192m}Ir, ^{158}Tb)	28.4 (2.56) (^{192m}Ir, ^{108m}Ag)	40 (13.1) (^{108m}Ag, ^{208}Bi)	(2.78e-3) (^{94}Nb, ^{14}C)

• All WDR values are given after a one year cooling period.

on averaging over the total volume of a particular region implying that internal voids will be filled with concrete before disposal. As shown in the table, the blanket may only qualify for disposal as Class C low level waste if it were disposed in its non-compacted form and only according to the 10CFR61 limits. The reflector could qualify for Class C waste in both forms according to 10CFR61 limits. Due to the low induced activity in the biological shield, it could qualify as Class A waste.

According to the 10CFR61 limits, LiPb could qualify for shallow land burial as Class A waste after extracting all the tritium. On the other hand, if Fetter limits are used, LiPb will not qualify for disposal as Class C waste. It is important to keep in mind that the waste disposal concentration limits used to calculate the waste disposal rating of the LiPb breeder are those assigned for the disposal of solid waste. Hence, LiPb has to be in solid form before such disposal can take place and the feasibility/practicality of such a process has to be determined.

7.2.8. Routine Atmospheric Effluents

The radiological dose to the population in the vicinity of the reactor site due to the routine release of tritium has been estimated by using the EPA AIRDOS-PC code. The code calculates the effective dose equivalent (EDE) as mandated by 40 CFR 61.93 and 61.94 to the maximally exposed individual (MEI) and at several distances from the point of release. Dose

Table 7.5. Routine Atmospheric Release Parameters

• Site Information	
Locations	Albuquerque Boston Chicago Los Angeles
Temperature	15°C
Rainfall	75 cm/yr
• Emission Information	
Year-Round Averaging	
Stack Height	75 m
Stack Diameter	30 cm
Momentum	1 m/s
• Tritium Pathways	
Reactor Building	20 Ci/day
Steam Generator	50 Ci/day
Fuel Reprocessing	25 Ci/day
Target Factory	16 Ci/day
Total (adjusted for 75% availability)	30,386 Ci/yr

values are computed from ingestion, inhalation, air immersion and ground surface pathways. As discussed in Section 7.1, we considered the routine release of tritium from the reactor building, steam generator, fuel reprocessing facility and the target factory.

Assuming the release parameters listed in Table 7.5 and using meteorological conditions at different cities, we calculated the dose expected at typical locations near Boston, Chicago, Albuquerque and Los Angeles. A summary of the results is shown in Table 7.6. The worst dose was in the Los Angeles area but was only 2.95 mrem/yr. More than 85% of the doses at all sites are incurred via the ingestion pathway. The estimated doses at all sites are far below the current EPA effluent limit of 10 mrem/yr and less than the 5 mrem/yr limit adopted by ITER. It is important to keep in mind that the estimated dose values strongly depend on the stack height. For example, using a 35 meter stack height results in an EDE of 13 mrem/yr at the site boundary (1 km) if the Los Angeles meteorological conditions were

Table 7.6. Dose to the Maximally Exposed Indvidual (MEI)

Site	Dose (mrem/yr)	Distance (m)
Albuquerque	2.2	1000
Boston	0.92	3000
Chicago	1.35	1000
Los Angeles	2.95	3000

used. The rule of thumb for determining the necessary stack height is to use 2.5 times the height of the nearest tall building in order to avoid downwash of the plume into the wake of the building [15]. A shorter stack must be justified with appropriate analysis.

7.2.9. Containment Accident Analysis

Another source of potential off-site doses which are of concern in LIBRA-SP are the doses produced by an accidental release of the radioactive inventory in the containment building. In this section we calculated the potential off-site doses using the worst release characteristics as defined by the ESECOM [16] methodology (Table 7.7). The doses are due to the release of some of the radioactive inventory of the blanket, reflector, shield and LiPb. In addition, we calculated the doses produced by the release of all the tritium contained in the reactor building during an accident. To account for the worst possible accident, a containment failure is postulated in order to produce significant off-site dose even though the probability of such a failure is very low.

During a loss of coolant accident (LOCA) or loss of flow accident (LOFA), a large increase in the steel structure temperature could lead to the mobilization and partial release of the radioactive inventory. Under adiabatic conditions, the decay heat generated within the first ten hours following a LOCA would increase the blanket temperature by $\sim$ 400°C. Under the same conditions, the decay heat generated in the reflector would increase its temperature by $\sim$ 100°C. Since the blanket and reflector peak operating temperatures are $\sim$ 625 and 400°C, respectively, the full mobilization of the structure radioactive products is impossible. The highest temperature a structure would reach determines the release

Table 7.7. Activation Products Release Characteristics

Pasquill Stability Class	F
Wind Speed	1 m/s
Inversion Layer Height	250 m
Deposition Velocity	0.01 m/s
Duration of Release	0.05 hr
Population Density	50 person/km^2
Ground Level Release	
Site Boundary	1 km and 10 km
Initial Plume Dimensions	
Sigma-Y	100 m
Sigma-Z	50 m
Percentage of Land	
Crop Farming	15%
Milk/Meat Products	15%
Groundshine Shielding	
Prompt Dose	0.7
Chronic Dose	0.33

fraction of its radioactive products. Off-site dose calculations have been performed using steel experimental volatility rates [17]. HT-9 volatility rates at 600 and 1000°C in dry air were used in this analysis for the reflector and blanket, respectively. To estimate conservative release fractions, we assumed a 10 hour LOCA in which the 1 hour release rates have been used for the full 10 hours to account for any possible loss of iron oxide protection. At 600°C, the reflector produces a whole body early dose at the site boundary of 253 mrem. Most of the dose is produced by the manganese isotopes, ^{54}Mn and ^{56}Mn. On the other hand, at 1000°C, the blanket would produce a WB early dose of 8.91 rem. In addition to the manganese isotopes, ^{32}P is the third major contributor to the off-site dose from the blanket.

The decay heat generated in the steel-reinforced concrete shield is very low. The decay heat generated within the first 2 months following a LOCA would only increase the shield temperature by < 3°C. Most of the radioactive inventory is contributed by the mild steel portion of the shield. Since the shield average operating temperature is 500°C, off-site dose calculations have been performed using adjusted PCA volatility rates at 600°C in dry

air. At 600°C, the whole body early dose at the site boundary is 37.1 mrem. Most of the dose is produced by the manganese isotopes, ^{54}Mn and ^{56}Mn. Even at 1000°C, the shield would only produce a WB early dose of 88.2 mrem.

LiPb is used as a coolant and breeder in LIBRA-SP. The steady state tritium inventory in LiPb is kept very low (3 g) by its continuous removal during the reactor operation. We calculated the potential off-site dose produced by the mobilization of LiPb during an accident where a breach of the containment is postulated. Following every fusion explosion, x-rays vaporize about 6.62 kg of LiPb. A simultaneous breach in the containment and chamber would allow cold air to flow into the chamber. The air starts cooling the LiPb vapor and hence reduces its vapor pressure. As LiPb vapor pressure falls, it starts condensing rapidly. The LiPb alloy was selected because it does not react vigorously with air or water. Nevertheless, we performed the off-site dose calculation assuming that all of the 6.62 kg of the vapor LiPb is mobilized and released to the environment. The resulting whole body early dose at the site boundary is 142 mrem. More than 65% of the dose is produced by tritium present in the LiPb at the onset of an accident. The rest of the dose is caused by ^{203}Pb, ^{110m}Ag and ^{210}Po.

The final source of potential off-site doses considered in this analysis is produced by the accidental release of tritium from the reactor containment. The two sources of tritium inside the reactor containment are the target injector and breeder loops. While the target injector contains as much as 49 grams of tritium (one hour supply), the LiPb breeder present in the reactor system has a steady state inventory of only 3 g. As shown in Table 7.1, the maximum amount of tritium that may be released from the LiPb primary and secondary loops are 10 and 1 grams, respectively. Assuming a 100% release, the whole body early dose produced by the release of all of the 60 g of tritium is 540 mrem.

Table 7.8 shows the potential off-site doses produced by simultaneous occurrence of the four previous scenarios. The total whole body dose at the site boundary mounts to 9.88 rem which is far below the 200 rem value recommended by the ESECOM study as a threshold for avoidance of early fatalities.

Table 7.8. Potential Off-Site Doses

	Blanket (1000°C)	Reflector (600°C)	Shield (600°C)	LiPb (6.62 kg)	Tritium (60 g)	Total
Prompt Dose at 1 km (Rem)						
WB	7.7	1.02e-1	3.17e-2	5.55e-2	7.04e-2	7.96
BM	9.87	3.61e-1	4.57e-2	1.06e-1	2.56e-1	10.63
Lung	14.5	5.52e-1	8.85e-2	2.13e-1	5.62e-1	15.92
LLI	6.33	2.29e-1	4.10e-2	4.77e-2	8.74e-2	6.74
WB Early Dose (Rem)						
At 1 km	8.91	2.53e-1	3.71e-2	1.42e-1	5.39e-1	9.88
At 10 km	5.86e-1	1.65e-2	2.29e-3	2.54e-2	5.39e-2	6.84e-1
WB Chronic Dose at 1 km (Rem)						
Inh + Grd	135	5.61e-1	5.46e-2	2.60e-1	7.42e-1	136.62
Ingestion	374	48.6	1.73	7.40	27.87	459.6
Total	509	49.1	1.79	7.66	28.63	596.23
WB Chronic Dose at 10 km (Rem)						
Inh + Grd	9.36	3.75e-2	3.38e-3	3.95e-2	1.72e-1	9.62
Ingestion	25.9	3.36	1.20e-1	1.32	6.47	37.17
Total	35.2	3.4	1.23e-1	1.36	6.61	46.79
Cancers						
Sum Organs	90.44	17.67	6.25e-1	1.696	8.22	118.65
WB	52.47	9.146	3.25e-1	3.763	16.72	82.43
Population Dose (Man-Rem)						
WB	3.32e+5	5.79e+4	2.06e+3	2.38e+4	1.06e+5	5.22e+5

7.2.10. Doses from the Target Factory and Fuel Reprocessing Facilities

As shown in Section 7.1, the target factory will produce a total of 337,000 targets/day. The daily amount of tritium processed in the factory is about 1200 g. However, the total vulnerable inventory present in the factory at any moment and which could be released in a severe accident is only 146 grams of tritium. Similarly, the fuel reprocessing facility contains a 2-hr amount of vulnerable inventory, or about 107 grams of tritium, which might be released in a severe accident. As shown in Table 7.9, assuming 100% release of tritium

Table 7.9. Off-Site Doses Due to Tritium Release from the Target Factory and Fuel Reprocessing Facilities

	Target Factory	Fuel Reprocessing
Prompt Dose at 1 km (Rem)		
WB	1.71e-1	1.25e-1
BM	6.22e-1	4.56e-1
Lung	1.37	1.00
LLI	2.13e-1	1.56e-1
WB Early Dose (Rem)		
At 1 km	1.31	9.6e-1
At 10 km	3.05e-1	2.24e-1
WB Chronic Dose at 1 km (Rem)		
Inh + Grd	1.8	1.32
Ingestion	67.83	49.71
Total	69.67	51.03
WB Chronic Dose at 10 km (Rem)		
Inh + Grd	4.18e-1	3.06e-1
Ingestion	15.75	11.54
Total	16.17	11.85
Cancers		
Sum Organs	20	14.66
WB	40.7	29.83
Population Dose (Man-Rem)		
WB	2.58e+5	1.89e+5

from both facilities during an accident would result in whole body early doses of 1.31 and 0.96 rem for the target factory and fuel reprocessing facility, respectively.

7.2.11. Nuclear Grade Components

N-Stamp nuclear grade components are only required if the estimated off-site dose released is above the 25 rem limit. As shown in the previous analysis, none of the reactor components would produce an off-site whole body early dose in excess of 25 rem during a conservative accident scenario. However, a total release of the steel structure radioactive inventory would produce an off-site dose which exceeds the 25 rem limits. In such a case some N-Stamp components would be required. Since such a total release is quite impossible due to the lack of sources of energy which are sufficient to mobilize the steel structure, we reached the conclusion that none of the reactor components would require nuclear grade materials. Similarly, due to the low tritium inventory present in the target factory and fuel reprocessing facility at any moment, we can also avoid the use of nuclear grade components in the proposed facilities.

References for Section 7

1. B. Badger, G. A. Moses, et al., "LIBRA - A Light Ion Beam Fusion Conceptual Reactor Design, University of Wisconsin, UWFDM-800, KfK-4710, Chapter 9, 1989.

2. J. L. Anderson, "Experience of TSTA Milestone Run with 100-Gram-Level of Tritium," *Fusion Tech.*, **14**, 438 (1988).

3. K. B. Woodall, S. K. Sood and A. Busigin, "Conceptual Design of a Laboratory Scale Impurity Detritiation and Hydrogen Isotope Separation System," Abstract: Fourth Topical Mtg. of Tritium Technology, Albuquerque, Sept. 29-Oct. 4, 1991.

4. Y. C. Chan and E. Veleckis, "A Thermodynamic Investigation of Dilute Solutions of Hydrogen in Liquid LiPb Alloys," *J. Nucl. Mater.*, 122&123, 935 (1984).

5. T. J. Dolan, G. R. Longhurst and E. Garcia-Otero, "A Vacuum Disengager for Tritium Removal from HYLIFE-II Reactor Flibe," *Fusion Tech.*, **21**, 1949 (1992).

6. G. R. Longhurst, "Gas Evolution from Spheres," (Informal Report) Idaho Nuclear Engineering Laboratory EGG-FSP-9634 (April 1991).

7. J. A. Blink, O. H. Krikorian and N. J. Hoffman, "The Use of Lithium in Fusion Reactors," Lawrence Livermore Laboratory, UCRL-85145 (June 1981).

8. R. O'Dell et al., "User's Manual for ONEDANT: A Code Package for One-Dimensional, Diffusion–Accelerated, Neutral Particle Transport," LA-9184-M, Los Alamos National Laboratory (1982).

9. D. L. Henderson and O. Yasar, "DKR-ICF: A Radioactivity and Dose Rate Calculation Code Package," UWFDM-714, Vol. 1, University of Wisconsin (April 1987).

10. L. J. Porter, "Upgrade of a Fusion Accident Analysis Code and Its Application to a Comparative Study of Seven Fusion Reactor Designs," PFC/RR-89-10, Massachusetts Institute of Technology (June 1989).

11. User's Guide for AIRDOS-PC, Version 3.0, EPA 520/6-89-035, U. S. Environmental Protection Agency, Office of Radiation Programs, Las Vegas, NV (December 1989).

12. Nuclear Regulatory Commission, 10CFR part 20, "Standards for Protection Against Radiation," (1975).

13. Nuclear Regulatory Commission, 10CFR part 61, "Licensing Requirements for Land Disposal of Radioactive Waste," Federal Register, FR 47, 57446 (1982).

14. S. Fetter, E. Cheng and F. Mann, "Long Term Radioactive Waste from Fusion Reactors," *Fusion Engineering and Design*, **13**, 239-246 (1990).

15. USNRC Regulatory Guide 1.145/Rev. 1 (February 1983).

16. J. P. Holdren et al., "Report of the Senior Committee on Environmental, Safety, and Economic Aspects of Magnetic Fusion Energy," UCRL-53766, Lawrence Livermore National Laboratory (1989).

17. S. J. Piet et al., "Initial Experimental Investigation of the Elemental Volatility from Steel Alloys for Fusion Safety Applications," EGG-FSP-8459, Idaho National Engineering Laboratory (April 1989).

8. LIBRA-SP System Parameters

The parameters for the LIBRA-SP conceptual design as of December 1, 1994 are presented in this chapter. The general power balance of LIBRA-SP is shown in Table 8.4. The same parameters are shown graphically in Figure 8.1. These general parameters are supported by more specific parameters for subsystems shown in Table 8.2 for the ion beams, Table 8.3 for the target, Table 8.4 for the target chamber, and Table 8.5 for activation and safety.

Table 8.1 shows the evolution of the LIBRA concept through three design concepts. The basic change for the three is the manner in which beams are transported. LIBRA used preformed plasma channels, LIBRA-LiTE used ballistic transport and LIBRA-SP uses self-pinched channels. As the designs progressed, improvements were made in analysis and subsystem concepts that led to better designs. One constant is that the HELIA inductive voltage adder technology for the drivers was used for all three designs. This technology has recently been shown to operate at high rep rate. The costs have been scaled from the LIBRA design, where a detailed costing study was performed. The thermal conversion efficiency of LIBRA-SP (43%) was obtained from the temperature of the target chamber coolant.

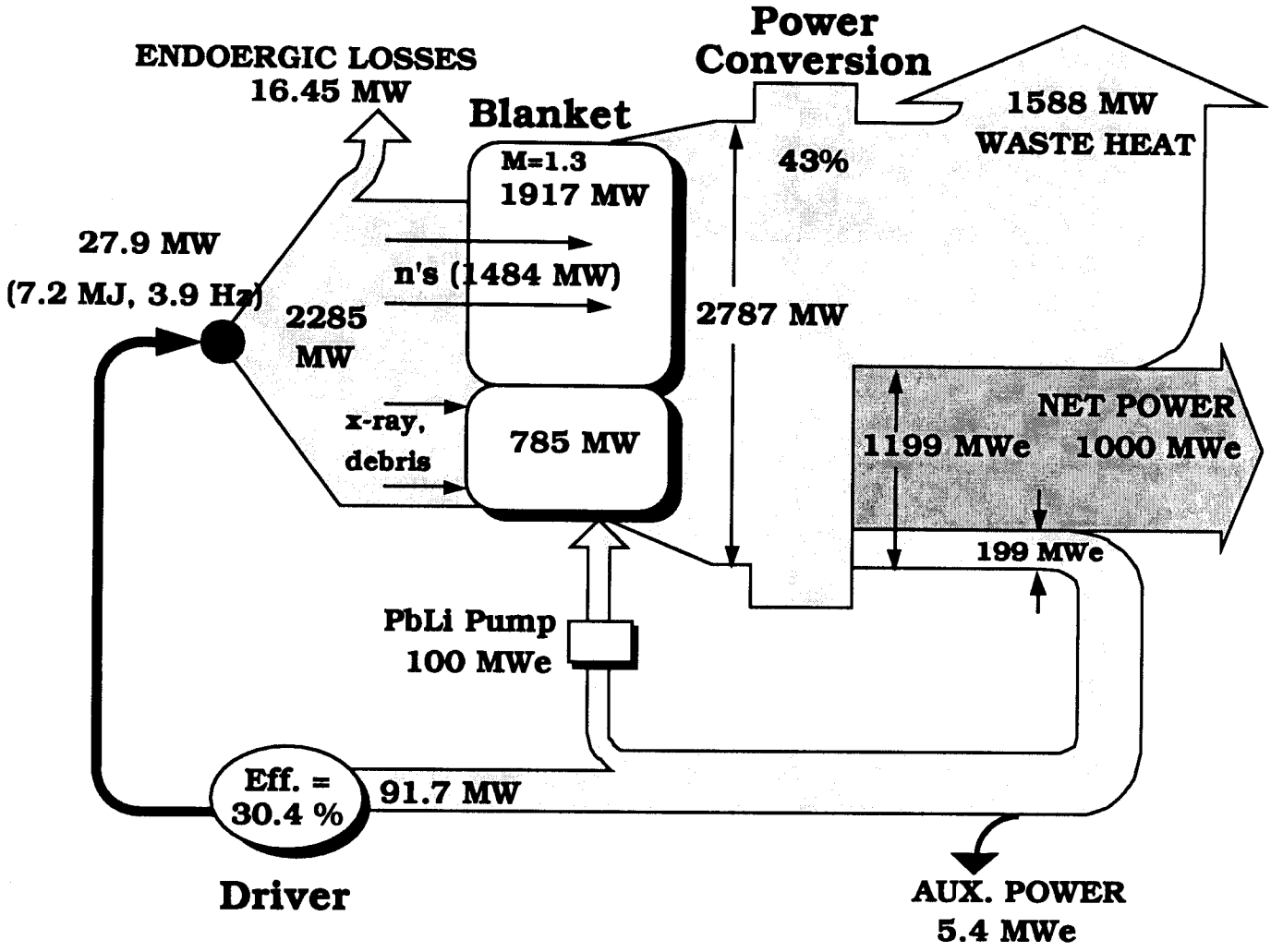

Figure 8.1. LIBRA-SP power balance.

Table 8.1. System Parameters for LIBRA, LIBRA-LiTE and LIBRA-SP

Parameter	Units	LIBRA	LIBRA-LiTE	LIBRA-SP
Net electrical power	MWe	331.96	1000.07	1001.45
Year published		1990	1991	1994
Accelerator technology		HELIA	HELIA	HELIA
Ion beam transport		Channel	Ballistic	Self-Pinched
Number of beams		18	30	24
Energy on target	MJ	4	6	7.2
Target gain		80	100	81.81
Target yield	MJ	320	600	589
Rep rate	Hz	3	3.99	3.88
Fusion power	MW	960	2394	2285
Target neutron fraction		0.6778	0.6778	0.6494
Target x-ray and ion fraction		0.2985	0.2985	0.3434
Target x-ray energy	MJ	63.68	119.40	168.08
Target debris energy	MJ	31.84	59.70	34.18
Target gamma fraction		0.0029	0.0029	0.00006
Target endoergic fraction		0.0209	0.0209	0.0072
Fusion neutron power	MW	653	1628	1484
Nuclear energy multiplication		1.28	1.211	1.292
Total neutron power	MW	836	1971	1917
X-ray and ion power	MW	287	715	785
Gamma power	MW	3.56	8.41	0.18
Endoergic power	MW	-20.06	-50.03	-16.45
Recirc. heat power	MW	37.40	83.10	85.00
Thermal power	MW	1163	2778	2787
Thermal efficiency		0.38	0.44	0.43
Gross electrical power	MWe	441.98	1222.11	1198.58

Table 8.1. (Continued)

Parameter	Units	LIBRA	LIBRA-LiTE	LIBRA-SP
Driver efficiency		0.49	0.376	0.376
Prime energy storage	MJ	17.01	33.24	23.64
Diode type		1 stage	1 stage	2 stage
Diode efficiency		0.8	0.8	0.9
Energy into diode	MJ	8.33	12.50	8.89
Transport efficiency		0.6	0.6	0.9
Energy into beam	MJ	6.67	10.00	8.00
Net driver efficiency		0.2352	0.18048	0.30456
Gain net driver efficiency		18.82	18.05	24.91
Net efficiency		0.0894	0.0794	0.1310
Gain efficiency		7.15	7.94	10.71
Driver power	MWe	51.02	132.65	91.73
Magnet power	MWe	27	75	0
Primary pump power	MWe	12	9	100
Secondary pump	MWe	15	0	0
Auxiliary power	MWe	5	5.4	5.4
Recirc. power	MWe	110.02	222.05	197.13
Recirc. power fraction		0.2489	0.1817	0.1645
Driver direct cost	M$ (1993)	304.38	426.06	323.93
Total direct cost	M$ (1993)	854.41	1739.56	1642.09
Unit direct cost	$(1993)/W	$2.57	$1.74	$1.64

Table 8.2. LIBRA-SP Ion Beam Parameters

Parameter	Unit	Main	Pre-Pulse
Ion species		Lithium	Lithium
Ion energy	MeV	30	30
Energy on target	MJ	6.0	1.2
Total transport efficiency	%	90	90
Energy leaving diodes	MJ	6.67	1.33
Number of beams		12	12
Pulse width at diodes	ns	40	40
Pulse width at target	ns	20	40
Power at diodes	TW	167	33
Power at target	TW	300	30
Particle current at diodes	MA	5.56	1.11
Particle current at target	MA	10	1
Diode			
Current/diode	kA	463	92.6
Voltage drop 1 V_1	MV	15	15
Voltage drop 2 V_2	MV	30	30
Physical gap 1 d_1	cm	2	2
Physical gap 1 d_2	cm	2	2
Enhancement factor K_e		5	5
Inner anode radius R_i	cm	10	10
Microdivergence θ_μ	mrad	4	4
Focal length F	cm	150	150
J_{scl}	kA/cm^2	0.3	0.3
J_d	kA/cm^2	1.5	1.5
Anode area A_a	cm^2	309	62
Outer anode radius R_o	cm	14.1	10.9
Focal spot radius r_f	cm	0.6	0.6
R/F		0.094	0.073
B_{crit} for gap 1	T	2.63	2.63
B_{crit} for gap 2	T	2.63	2.63
B_{appl} for gap 1	T	5.27	5.27
B_{appl} for gap 2	T	5.27	5.27

Table 8.2. (Continued)

Parameter	Unit	Main	Pre-Pulse
Self-Pinched Transport			
Transport length L	cm	550	550
γ		1.005	1.005
β		0.096	0.096
Charge state		3	3
Alfvén current	kA	6958	6958
I_{net}	kA	30.7	18.5
f_m		0.978	0.933
Energy loss ϵ	kJ	14.9	1.8
Efficiency	%	97.3	98.4
Neutronics			
Diode casing	dpa/FPY	0.06	0.06
End-of-life diode casing	dpa	1.8	1.8
Fast n fluence per FPY @ 5.7 m	n/cm^2	1.67×10^{20}	1.67×10^{20}
Lifetime of diode magnet out of direct-line-of-sight	FPY	240	240
Fast n fluence per FPY @ 5.7 m in direct line-of sight	n/cm^2	6.4×10^{21}	6.4×10^{21}
Lifetime of diode magnet in direct line-of-sight	FPY	6.25	6.25
Diode Vacuum System Parameters			
Initial He atom density in chamber	$\#/cm^3$	7×10^{15}	
Initial chamber pressure in chamber	torr	0.52	
Pressure in chamber after a pulse	torr	260	
Volume of reaction chamber	m^3	2325	
Pressure required in diode enclosure	torr	10^{-4}	
Volume of diode enclosure	m^3	0.17	
Diode beam aperture diameter	cm	2.0	
Diameter of beam tube	cm	2.0	
Length of beam tube	cm	150	
Rotating disc diameter	m	0.5	
Hole in the disc is at a radius of	m	0.2	
Rep-rate of reactor	Hz	3.9	
Rep-rate of disc	Hz	3.9	
Pressure rise in diode enclosure	torr	4.3×10^{-2}	
Pump capacity for each diode (ℓ/s)		4500	

Table 8.3. Parameters for the LIBRA-SP Target

General Parameters	
Total absorbed beam energy (MJ)	7.2
Peak beam ion (TW)	330
Hohlraum radius (cm)	0.7
Yield (MJ)	589
Peak beam intensity (TW/cm^2)	54
Target mass (mg)	151.5
Burnup fraction (%)	35
Target gain	82
Debris Ion Kinetic Energies	
Species	Energy (MJ)
H	0.029
D	0.062
T	0.094
C	2.07
Pb	15.9
Target Burn Parameters	
Total yield	589 MJ
Neutron yield	383 MJ
X-ray yield	167 MJ
Debris ion yield	35 MJ
Energy lost in endoergic reactions	4 MJ
Target Data at Ignition	
	Material
Region 1	DT
Region 2	CH
Region 3	C
Region 4	Pb
	Density (g/cm^3)
Region 1	230
Region 2	0.013
Region 3	0.024
Region 4	11.4

Table 8.3. (Continued)

Target Data at Ignition (continued)	
	Radius Range (cm)
Region 1	0-0.0173
Region 2	0.0173-0.55
Region 3	0.55-0.6983
Region 4	0.6983-0.7
	Mass (mg)
Region 1	5.0
Region 2	9.1
Region 3	17.4
Region 4	120
Nuclear Energy Deposition in Target	
Region 1	2.53896 MeV/DT fusion
Region 2	0.00345 MeV/DT fusion
Region 3	0.00039 MeV/DT fusion
Region 4	0.00002 MeV/DT fusion
Total	2.54282 MeV/DT fusion
Energy Partitioning from LIBRA-SP Target	
Fusion energy	17.6 MeV/DT fusion
Energy carried by neutrons	11.429 MeV/DT fusion (64.94%)
Energy carried by gamma photons	0.001 MeV/DT fusion (0.006%)
Energy carried by x-rays and debris	6.043 MeV/DT fusion (34.34%)
Energy lost in endoergic reactions	0.127 MeV/DT fusion (0.72%)

Table 8.4. Parameters for the LIBRA-SP Target Chamber

First Surface (FS) Parameters	
Density of HT-9 (kg/m^3)	7625
Elastic modulus of HT-9 (GPa)	163.0
Density of LiPb (kg/m^3)	9440
Tube diameter (cm)	3
Tube thickness (mm)	3
Flow velocity (m/s)	4.0
Rep rate (Hz)	3.88
Number of the coolant tubes in the FS	362
Total surface area (m^2)	1910.6
Thickness of LiPb recondensed per second (μm)	1.35
Heat flux due to recondensation at FS (W/cm^2)	107
Maximum value of volumetric heating at FS (W/cm^3)	37
Temperature rise in the coolant tube wall (HT-9 wall thick = 3 mm) due to:	
1 - Surface heat flux only (condensation) (°C)	117.5
2 - Volumetric heating only (°C)	7.5
Total temperature rise in the FS coolant tube wall (°C)	125
Maximum FS coolant velocity (at inlet) (m/s)	4.0
Minimum FS coolant velocity (at exit) (m/s)	2.9
Inlet FS coolant bulk temperature (°C)	370
Exit FS coolant bulk temperature (°C)	430 (32.32×10^4 kg/s)
Average coolant bulk temperature of outside coolant (°C)	650 (12.26×10^4 kg/s)
Exit blanket coolant bulk temperature (°C) (V = 17.4 cm/s)	600 (5.23×10^4 kg/s)
Total mass flow rate (kg/s)	49.78×10^4
HX inlet coolant bulk temperature (°C)	502
Pumping power (inside cavity) (MW)	47.61
Thermal conversion efficiency (%)	43

Table 8.4. (Continued)

Chamber Neutronics Parameters	
Inner radius of blanket	4 m
Chamber wall radius	5.2 m
Neutron wall loading	7.4 MW/m^2
Local TBR	1.48
Nuclear energy multiplication, M_n	1.292
Overall energy multiplication, M_o	1.182
Peak dpa rate in PERIT tubes	94.2 dpa/FPY
Lifetime of front PERIT tubes	1.6 FPY
Peak helium production rate in PERIT tubes	436 He appm/FPY
Peak power density in PERIT tubes	18.3 W/cm^3
Peak dpa rate in chamber wall	4.2 dpa/FPY
Peak end-of-life damage in chamber wall	126 dpa
Peak helium production rate in chamber wall	0.9 He appm/FPY
Peak power density in chamber wall	0.52 W/cm^3

Table 8.5 (a). Tritium Inventory and LIBRA-SP Release Summary

Location	System	Inventory	Tritium Routine Release	Tritium Accidental Release
Target factory	–	g	Ci/d	g(T)
	In process	146	12	146
	Storage	1200	2	0
Reactor building	Targets	49	4	49
	Breeder alloy			
	Primary	31.5	15	10
	Secondary	1.0	1	1
Fuel reprocessing	Equipment	107	13	107
	Cryo-still	14	12	0
Storage	Vault	2000	2	0
Steam generator	Water	0	50	0
	Coolant			
		Routine release		
		Air 61 Ci/d		
		Water 50 Ci/d		
				312

Table 8.5 (b). Radioactivity After Shutdown

Time After Shutdown	Activity (MCi)		Decay Heat (MW)		BHP (km^3 air)	
	Blanket	Reflector	Blanket	Reflector	Blanket	Reflector
0	721	924	2.99	3.34	3.7e+8	1.63e+9
1 hour	620	684	2.18	2.88	8.9e+7	8.02e+7
1 day	498	407	0.46	1.09	8.2e+7	5.54e+7
1 week	480	175	0.42	0.18	8.01e+7	3.2e+7
1 month	449	147	0.39	0.14	7.5e+7	2.7e+7
1 year	307	63	0.22	5.63e-2	3.7e+7	9.24e+6
10 years	29	6.5	1.23e-2	1.05e-2	1.05e+6	2.0e+6
100 years	2.78e-3	8.2e-3	1.39e-6	2.72e-6	1.02e+4	4.1e+4

Table 8.5 (c). Waste Disposal Ratings (WDR) of the Different Regions of LIBRA

WDR	Blanket	Reflector	LiPb	Shield
Class A (10CFR61 limits)	40.5 (1.62) (^{94}Nb, ^{3}H)	8.5 (7.66) (^{94}Nb, ^{60}Co)	0.2 (0.064) (^{63}Ni, ^{60}Co)	(0.125) (^{14}C, ^{94}Nb
Class C (10CFR61 limits)	2.57 (0.103) (^{94}Nb, ^{14}C)	0.68 (0.61) (^{94}Nb, ^{14}C)	9.6e-4 (3.2e-4) (^{63}Ni)	(8.64e-3) (^{14}C, ^{94}Nb
Class C (Fetter limits)	41.5 (1.66) (^{192m}Ir, ^{158}Tb)	28.4 (2.56) (^{192m}Ir, ^{108m}Ag)	40 (13.1) (^{108m}Ag, ^{208}Bi)	(2.78e-3) (^{94}Nb, ^{14}C)

- All WDR values are given after a one year cooling period.

Table 8.5 (d). Routine Atmospheric Release Parameters

• Site Information:	
Locations:	Albuquerque Boston Chicago Los Angeles
Temperature:	15 C
Rainfall:	75 cm/yr
• Emission Information:	
Year-Round Averaging	
Stack Height:	75 m
Stack Diameter:	30 cm
Momentum:	1 m/s
• Tritium Pathways:	
Reactor Building:	20 Ci/day
Steam Generator:	50 Ci/day
Fuel Reprocessing:	25 Ci/day
Target Factory:	16 Ci/day
Total (adjusted for 75% availability):	30,386 Ci/yr

9. Conclusions and Recommendations

The use of self-propagation schemes for light ions has allowed us to remove the final focusing magnets from inside the chamber that were required by ballistically focused ions. It also removes the complexity of pre-formed plasma channels used in channel transport. This ion propagation mechanism greatly simplifies the reaction chamber design by removing vulnerable focusing magnets and should result in a more robust and long lasting cavity design. The credibility of the propagation scheme can be demonstrated on existing or modified facilities. If such confirmation occurs, then one of the main obstacles to economical power generation will have been removed.

The use of solid perforated tubes (PERIT units) in place of flexible INPORT units removes the need for pre-tension on the tubes to avoid interference during pulsing. The fact the tubes are rigid allows them to be curved, thus resulting in a more uniform heat flux to the units. An additional, and very important side effect of using the PERIT units is the fact that the distance from the final diode to the target can be reduced, thus increasing the credibility of the self-pinched mode of operation. The feasibility of the PERIT liquid fan concept can be verified in simple flow experiments.

Credible design of the ion beam entrance ports has allowed us to develop more detailed shield configurations to shield the final diodes. As the design of Li diodes progresses, we will be able to demonstrate credible operating scenarios to insure long lasting components.

Recent declassification of target designs in the U.S. has allowed us to more correctly describe the geometry, mass, and manufacturing requirements for light ion beam targets. More detailed target information now allows more accurate description of the target debris and x-rays and consequently their effects on the first solid components of a reactor cavity. Declassification has allowed us to make significant progress in computing equations of state and opacities.

In spite of significant progress in 1994, there are several issues that still remain to be examined in the future. First, the development of the IPROP code as a design tool would be extremely valuable for examining self-pinched propagation. Integration of this code with others that we have developed for the ICF program over the past 20 years will enable us to develop more sophisticated designs with less human resources. Second, the calculation of light ion target performance using the new BUCKY-1 radiation hydrodynamics code under

reactor conditions will allow us to be more quantitative about the design margin available in the LIBRA class of reactors. This adds an important dimension to the fusion performance that has never before been analyzed for ICF reactor designs. More accurate pointing, beam size limits, neutron and target debris spectra, and x-ray spectra will allow us to optimize the inner tube design for longer lifetime. Finally, the improved knowledge of the degraded neutron spectra from the declassified targets will allow more credible radiation damage and activation calculations. These should bolster the environmental and economic arguments for fusion.

Appendices

Fusion Technology Institute

Nuclear Engineering and Engineering Physics Department
University of Wisconsin–Madison

MEMORANDUM

To:	LIBRA Team
From:	Bob Peterson RPP
Subject:	Self-Pinched Ion Transport
Date:	October 14, 1994

A workshop was held at Sandia National Laboratory in Albuquerque NM September 20-21, 1994 on Transport for a Common Ion Driver. The three US National Laboratories leading Ion Beam Fusion Research in the US (SNL, LBL and LLNL) have agreed to cooperate with each other in areas of common concerns to Light and Heavy Ion Fusion. SNL is a proponent of Light Ion Fusion, while LBL and LLNL favor Heavy Ions. Jeff Quintenz, the director of the Light Ion Fusion Program at SNL and Mike Campbell the Director of the ICF Program at LLNL made comments at the workshop to the effect that both the Heavy and Light Ion programs need to collaborate where possible in the areas of physics understanding and computer code development and verification. The collaborations may or may not lead to the understanding of an optimum ion species and a common driver technology. This workshop was the first manifestation of this spirit of cooperation. Workshops on targets and accelerators are planned.

At this workshop, technical presentations were made by scientists working at several institutions around the country on the topic of ion beam transport (see attached agenda). Light Ion transport experiments performed at NRL for channels, wire-guided, and ballistic transport were summarized. Analytic calculations done for ballistic Light and Heavy ion transport at NRL, SNL, and LBL were discussed. Analytic and computational studies of light ion transport in channnels performed by researchers at NRL and SNL were presented. Computer simulations of ballistic heavy ion transport were presented by LLNL. The LIBRA and HYLIFE families of Light and Heavy Ion reactor studies were presented by UW and LLNL. Atomic physics issues for ion beam transport was presented by UW. The IPROP computer code and comparisons with ballistic transport experiments at NRL was presented by MRC. Finally the workshop turned to the issue of self-pinched transport.

Self-pinched transport looks attractive to both Light and Heavy Ion Fusion. It looks to be efficient to transport for several meters, to have channel sizes that are smaller than the targets, and to require none of the structures inside the target chamber that ballistic, channel and wire transport do. Craig Olson of SNL has formulated a simple analytic theory of self-pinched transport. Dale Welsh of MRC have begun to study self-pinched transport with the IPROP code. Joe MacFarlane and Wang Ping of UW have opened discussions with Dale Welsh on implementation of better atomic physics models into IPROP.

439 ENGINEERING RESEARCH BUILDING • 1500 JOHNSON DRIVE • MADISON WISCONSIN 53706-1687 • (608) 263-4798/2352

I have used the formalism of Craig Olson to study self-pinched transport in LIBRA-SP and to look at how the transport will change at higher atomic numbers. Self-pinched transport uses the azimuthal magnetic field produced by the un-neutralized fraction of the the ion beam current to confine the beam ions to a narrow channel. The net current, I_{net}, is therefore a function of the angle that the ions make with the direction of propagation and the spot radius of the beam as it begins to propagate, r_s. The angle of the ions is R_o/F, where F is the focal length of the diode and R_o is the outer radius of the diode's anode. The length and the spot radius are related by the beam microdivergence θ_μ. The formula for the net current required for transport is,

$$I_{net} = 0.5 \left(\frac{R_o}{r_s}\right)^2 \theta_\mu^2 I_A \tag{1}$$

where

$$I_A = \beta\gamma \frac{A}{q} \frac{m_p c^3}{e} \tag{2}$$

is the Alfvén current. β and γ are the normal relativistic parameters for the ion beam. A is the beam atomic mass number and q is the charge on the beam during transport. The current neutralization factor is defined as,

$$f_m = 1 - \frac{Inet}{I_{beam}}. \tag{3}$$

The diode design parameters determine how well self-pinched transport will function. The anode area and the inner radius determine R_o. The anode inner radius must be large enough for all required magnetic field coils and associated power feeds and cooling to fit inside; I have assumed it is 3 cm for the sake of argument. The area is just the required current divided by the enhanced space-charge-limited current density. From the Child-Langmuir law, and assuming that the current density is enhanced by a factor of 8.5, the current density on the anode is,

$$J_a = 1.215 \frac{V^{3/2} q_1}{A d^2} \; kA/cm^2. \tag{4}$$

V is the voltage across the first gap of a multigap diode in MV, A is the atomic mass in gm/mole, and d is the physical gap length of the first gap in cm. q_1 is the charge state of the ion in the first gap, and is assumed to be 1 for these examples. d is assumed to be 2 cm for all the examples discussed here. The maximum possible V is assumed to be 50 MV. The microdivergence is assumed to be 4 mrad and the focal length is 150 cm.

With these diode limits, and using the formalism discussed above, I have calculated the diode and transport parameters for all of the alkali metals (Li, Na, K, Rb, and Cs). The ion energy for a range of 30 mg/cm^2 in gold is assumed to equal $4ZA^{1/2}\ MeV$. The beam power requirements are assume to be 13.9 $TW/beam$ in the main pulse at the 12 diodes. From this I obtain the following Table.

Table 1: Self-Pinched Transport and Diode Parameters for Alkali-Metal Ions

Ion	Li	Na	K	Rb	Cs
A (amu)	6.939	23.0	39.1	85.5	132.1
Z	3	11	19	37	55
Ion Energy (MeV)	30	211	475	1346	2457
Particle Current per Diode (kA)	463	66	29	10	6
V (MV)	15	50	50	50	50
J_A (kA/cm^2)	2.54	8.5	6.5	4.4	3.6
R_o (cm)	8.18	3.4	3.2	3.1	3.1
R_o/F	0.055	0.025	0.0215	0.021	0.0206
q during Transport	3	10	10	10	10
I_A (MA)	6.96	10.1	19.8	49	83
I_net (kA)	10.35	2.57	4.58	10.7	17.5
$1 - f_m$	0.0075	0.004	0.16	0.103	0.309

There are of course many issues of self-pinched transport still to be studied. The guiding of the beams with narrow tubes looks promising and would avoid the use of a pre-ionizing laser, but questions such as bends in the tube persist. Energy loss and transport efficiency are thought to be favorable, but computer simulations and experiments are needed.